Versatile apparatus for ultracold atomic hybrid systems

by

Andrei Tretiakov

A thesis submitted in partial fulfilment of the requirements for the degree of

Master of Science

Department of Physics
University of Alberta

Abstract

In modern quantum technology, different quantum systems have properties that make them effective for some tasks and less beneficial for others. Integrating these systems together into a single quantum hybrid system, exploiting the advantages of each systems strengths while suppressing their disadvantages, can advance the total performance. On-chip quantum hybrid systems coupled to an ensemble of ultracold atoms show a great potential for advancing quantum technology, because they combine the long coherence time of the atomic ensemble with access to conventional read-out techniques provided by the chip.

This thesis presents an apparatus that we have built to carry out experiments with coupling ultracold ^{87}Rb gases to various systems, including nanomechanics and optical cavities. The apparatus operates at ultra-high vacuum conditions, required for experiments with ultracold gases, and its design allows us to easily and quickly switch between different on-chip devices to perform and study quantum hybridization with ultracold gases. Such versatility is provided by separating the region where the ultracold gas is created from the location of the chip, and implementing a system which can optically transfer the atoms between these two regions.

In this work we also describe atom cooling techniques used in this experiment, including magneto-optical trapping, sub-Doppler cooling in optical molasses and evaporative cooling. These methods have demonstrated cooling to temperatures below 100 μK. We also discuss a setup for optimal optical-dipole transport.

Finally, we theoretically consider magnetic coupling between atoms and nanomechanical oscillators and propose using the Landau-Zener transitions as a method for reducing or measuring mechanical temperature of the resonators, and to create quantum entanglement between multiple devices.

Preface

Most of the work described in this thesis was done by myself under an attentive supervision of Dr. Lindsay LeBlanc, with a help and contributions from other lab members (current and past) and an experienced technician Greg Popowich. The whole apparatus was designed by L. LeBlanc and assembled mostly by myself. During many stages of the experiment I was following the footprints of T. Hrushevskyi and Dr. E. Saglamyurek, who are working on the Quantum simulation project in our lab.

The majority of the parts (section 3.2) of the vacuum system were cleaned and assembled (section 3.1) by myself. Ion pumps and the titanium sublimation pump (section 3.2.1) were set up by G. Popowich. The complete vacuum system was baked (section 3.1.2) by myself and L. LeBlanc. During the bake we used a temperature monitor built by W. Morrish (not described in the thesis).

The laser locking and control system (not described in the thesis) was set up by L. LeBlanc. The optics for the laser cooling (section 3.4) was assembled and connected to the main laser system by myself, while the holders for the optics (not described in the thesis) were designed and machined by G. Popowich. The imaging system (section 3.5.2) was set up by myself. The image acquisition and analysis software (not described in the thesis) was originally written by W. Morrish and L. LeBlanc, and recently updated by L. LeBlanc and S. Wilson.

Bias field magnetic system, that includes coils (section 3.3.2) and the electric current servo-control system (section 3.3.3), was designed by L. LeBlanc and built by myself and L. LeBlanc. For the servo controller for the current control system we used the design by I. Spielman at NIST (not described in the thesis). Quadrupole field coils (section 3.3.1) for magnetic and magneto-optical trapping as well as the water cooling system (not described in the thesis) for them were made by G. Popowich. For the control of trapping quadrupole field I used electric current servo-control system built by T. Hrushevskyi and E. Saglamyurek. Coils for the evaporative cooling (section 3.3.5) were done by myself based on samples generously provided by T. Hrushevskyi.

The computer control of the experiment is carried out in a labview program (not described in the thesis), originally written by I. Spielman and J.V. Porto at NIST and adapted by L. LeBlanc. All steps of the experiment and the corresponding data analysis (Chapter 4) were performed by myself using the results of T. Hrushevskyi and E. Saglamyurek as a starting point.

The preliminary work on testing and calibrating the lens system for optical dipole transport (not described in the thesis) was started by H. Sharum and continued by M.X. Na. This system was enhanced and integrated with the main apparatus (section 3.6) by myself.

Theoretical work on the Landau-Zener transitions in atom-to-nanostring system (Chapter 5) was done by L. LeBlanc and myself and was recently published in [A. Tretiakov and L.J. LeBlanc, Phys. Rev. A 94, 043802] [1]. My contribution to this work includes study and calculation of magnetic coupling between atomic spins and magnetized mechanical oscillators (section 5.3 in discussion with L. LeBlanc), the idea to use the Landau-Zener sweeps to manipulate the state of the oscillator (expression 5.14) and to create the quantum entanglement between two oscillators (section 5.4.3). The chip design for magnetic trapping (Figure 5.2 (a)) was proposed by L. LeBlanc while the corresponding trapping potential (Figure 5.2 (b-c)) was numerically calculated by myself. The mechanical cooling scheme (section 5.4.1) was proposed and developed by L. LeBlanc. The mechanical thermometry (section 5.4.2) was originally proposed by J. Davis and developed by L. LeBlanc and myself. The whole composition of Chapter 5 was adapted from [A. Tretiakov and L.J. LeBlanc, Phys. Rev. A 94, 043802] by myself, including an additional theoretical section 5.1.

Acknowledgements

I would like express my appreciation to my committee members, Professors Mark Freeman and John Davis for their valuable advice on the preparation of this thesis, and especially my supervisor Dr. Lindsay LeBlanc for her guidance and help with the experiment and theoretical work, valuable discussions during our weekly meetings and tedious proofreading of this thesis.

Also, I want thank Greg Popowich for his help with setting up hi-tech equipment for our apparatus, my colleagues Taras Hrushevskyi and Dr. Erhan Saglamyurek for their consultation and occasional help during the experiment, and many undergraduates who directly or indirectly contributed to the project, especially Haille Sharum and Ketty (M.X.) Na for their work on the optical-dipole transport system.

Contents

List of Figures

List of Tables

Chapter 1

Introduction

Modern quantum technology, such as quantum information processing and storage, quantum communication and cryptography, and high-precision measurements, can be advanced by using quantum hybrid systems [2–4] – systems that integrate components from different kinds of quantum technologies that are best-suited for individual quantum tasks or allow control and read-out by classical signals. Apart from practical applications, hybrid systems can be used to study and better understand the classical-to-quantum crossover: the process during which macro- or mesoscopic objects, which are usually fully described by the laws of classical physics, start showing quantum behaviour [5–7]. Similarly, these systems help us to understand the opposite process of the quantum-to-classical crossover, usually governed by decoherence [8].

Among various candidates as a part of a quantum hybrid system, such as superconducting circuits [9,10], NV-centers in diamonds [11,12], cavity photons [12,13] and nanomechanical oscillators [3,11,13], ultracold atomic ensembles show great potential due to their long coherence time and easy state control by electromagnetic fields. In our lab, we are particularly interested in coupling ultracold gases to nanomechanical oscillators, which can be read-out and controlled by conventional techniques through optical and electrical signals, and can be cooled to their mechanical ground states cryogenically [14] or optically [15]. Previous work in other labs demonstrated coupling between atomic ensembles and different kinds of mechanical devices: optically-mediated coupling to a membrane [16–18], to cantilevers [19,20] and to an on-chip cantilever via fluctuations of vacuum electromagnetic field [21]. For our experiment we decided to use a high-tensile stress SiN nanostring design [22–25], which promises high quality factors and was successfully implemented and analysed by our collaborators at the University of Alberta [24]. Also, we focus our considerations on atom

chip technology [26,27] which in addition to nanomechanical systems, has shown coherent coupling of atomic ensembles to superconducting circuits integrated with microwave cavities [28] and optical cavities [29].

This manuscript describes current progress towards building a machine that allows to create and study hybridization of ultracold ^{87}Rb gas with various types of on-chip devices, which can be replaced in a relatively fast and easy way. This versatility is achieved by using a design, in which the region where gas cooling happens ("preparation region") and the place where the on-chip experiments are carried out ("science chamber") are spatially separated [30]. Even though these regions are integrated into a single ultrahigh vacuum system, the preparation region can be isolated from the rest with a gate valve during the loading and baking of a new chip. This prevents us from removing and reassembling magnetic coils and various optical components for atomic cooling and imaging, as well as tedious and time-consuming alignment of the optics and optimization of cooling steps after each chip change. In order to move the cooled atoms to the science chamber, we are implementing the optical dipole transport with a system of focus-tunable lenses, as was recently proposed and successfully demonstrated [31].

Chapter 2 presents a basic general theory of interactions between atoms and optical and magnetic fields, which is essential to understand the experimental techniques used in this project for cooling and trapping of atoms. Also it discusses the energy levels structure of alkali metals in general, and of ^{87}Rb used in this experiment in particular. **Chapter** 3 outlines the main parts of the apparatus, procedures to achieve ultrahigh vacuum conditions, including cleaning and baking of the vacuum system. Also, this chapter describes the imaging and temperature measurement of the atomic clouds. **Chapter** 4 provides theoretical description and the experimental results of the laser cooling, magnetic trapping and evaporative cooling of atoms in this work, and gives details on the principles of optimal optical transport. In **Chapter** 5 we propose using the Landau-Zener transitions [32] for cooling and calibration of the mechanical motion of a magnetized nanostring, as well as quantum entanglement of two nanostrings, based on a recently published paper [1]. **Chapter** 6 gives the summary of the experiment with future directions. The **Appendix** shows the absorption imaging pictures of the atomic cloud after the main stages of the laser cooling and magnetic trapping at the base pressure.

Chapter 2

Theory

This chapter presents general theory behind the main cooling techniques used for realization of ultracold quantum gases. We will discuss evolution of a two-level system under influence of a periodic off-diagonal perturbation (section 2.1), which describes a scattering force exerted on an atom by near-resonant light - the main component of laser cooling and magneto-optical trapping. Further, the energy-level structure of alkali metals (section 2.2) and its dependence on external electric and magnetic fields are explained (sections 2.3 and 2.4).

2.1 Two-level atom interacting with light. Scattering force

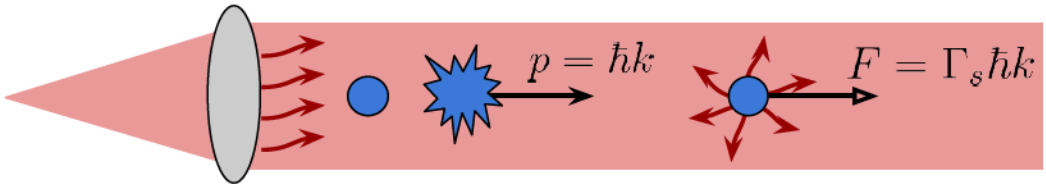

Figure 2.1: Schematic illustration of scattering force concept. After absorbing photons of the light field and re-emitting them in random direction an atom experiences a force proportional to the scattering rate.

Most laser cooling and trapping techniques rely on the concept of a scattering force, illustrated schematically in Figure 2.1. An atom illuminated by a laser gains momentum Δp, in the direction of the light propagation, by absorbing photons. Then, the atom spontaneously radiates a photon in a random direction. Due to the isotropy of the spontaneous emission, the net recoil momentum

from the emission processes (after many events) is zero. The resulting scattering force F points in the direction of the light's k-vector and is equal to the product of a single-photon momentum and the average scattering rate[1]:

$$F = \left\langle \frac{\Delta p}{\Delta t} \right\rangle = \hbar k \left\langle \frac{1}{\Delta t} \right\rangle = \hbar k \Gamma_s, \tag{2.1}$$

where Γ_s is the average scattering rate. Assuming that the time of momentum transfer Δt is smaller than the atom excited state lifetime and that after the emission another photon is absorbed immediately, the scattering rate can be expressed as a a product of the spontaneous emission rate Γ and the probability of being in an excited state p_e:

$$\Gamma_s = \Gamma p_e. \tag{2.2}$$

Below, we derive the scattering rate for the case when the atom can be considered as a two-level system.

2.1.1 Rabi oscillations in a two-level system

The interaction between an oscillating electromagnetic field and an atom can be described in semi-classical picture by the Hamiltonian

$$\hat{H} = \hat{H}_0 + \hat{H}_I. \tag{2.3}$$

Here, the first term corresponds to the atomic energy in the absence of an external electromagnetic field and the second characterizes the time-dependent interaction between the field and atomic electric or magnetic dipole.

For most practical applications, it is sufficient to consider the atom as a two-level system in the basis of eigenstates of $\hat{H}_0$:

$$\hat{H}_0 \left|\phi_1\right\rangle = \hbar\omega_1 \left|\phi_1\right\rangle, \hat{H}_0 \left|\phi_2\right\rangle = \hbar\omega_2 \left|\phi_2\right\rangle, \tag{2.4}$$

where state $|\phi_1\rangle$ corresponds to the ground state and $|\phi_2\rangle$ to the excited state. The interaction

[1]Most of the derivations in this section follow a standard textbook approach, e.g. see [33] or [34].

term can be described as

$$\hat{H}_I = \hat{V}\cos(\omega t) = -\hat{\mathbf{d}} \cdot \mathbf{E}\cos(\omega t), \tag{2.5}$$

where $\hat{\mathbf{d}} = e\mathbf{r}$ is the electric dipole operator and $\mathbf{E}$ is the electric field vector. Note that $\langle\phi_1|\,\hat{V}\,|\phi_1\rangle = \langle\phi_2|\,\hat{V}\,|\phi_2\rangle = 0$ due to the odd parity of the dipole operator.

The basis states evolve in time as $|\phi_1(t)\rangle = |1\rangle\exp(-i\omega_1 t)$ and $|\phi_2(t)\rangle = |2\rangle\exp(-i\omega_2 t)$, where $|1\rangle$ and $|2\rangle$ are basis states at $t = 0$. The wavefunction of the atom at moment of time t is the superposition of these two states:

$$|\psi(t)\rangle = c_1(t)\,|\phi_1(t)\rangle + c_2(t)\,|\phi_2(t)\rangle\,, \tag{2.6}$$

where coefficients $c_1(t)$ and $c_2(t)$ govern the time evolution of the wavefunction with respect to the basis. Projecting the Schrödinger equation

$$i\hbar\frac{d\,|\psi(t)\rangle}{dt} = \hat{H}\,|\psi(t)\rangle \tag{2.7}$$

onto $|1\rangle$ and $|2\rangle$ gives a set of ordinary differential equations for the the coefficients $c_1(t)$ and $c_2(t)$:

$$\frac{d}{dt}c_1(t) = i\Omega_R e^{-i\omega_{21}t}\cos(\omega t)c_2(t), \tag{2.8}$$

$$\frac{d}{dt}c_2(t) = i\Omega_R e^{i\omega_{21}t}\cos(\omega t)c_1(t); \tag{2.9}$$

where $\hbar\Omega_R = -\langle 1|\,\hat{V}\,|2\rangle = -\langle 2|\,\hat{V}\,|1\rangle$ (since the coupling is real) and $\omega_{21} = \omega_2 - \omega_1$. Using Euler's formula $\cos(\omega t) = (e^{i\omega t} + e^{-i\omega t})/2$, these equations can be rewritten as

$$\frac{d}{dt}c_1(t) = \frac{i\Omega_R}{2}(e^{i(\omega-\omega_{21})t} + e^{-i(\omega+\omega_{21})t})c_2(t), \tag{2.10}$$

$$\frac{d}{dt}c_2(t) = \frac{i\Omega_R}{2}(e^{i(\omega+\omega_{21})t} + e^{-i(\omega-\omega_{21})t})c_1(t). \tag{2.11}$$

In the case where ω is close to resonance frequency ω_{21}, the rapidly oscillating terms $e^{-i(\omega_{21}+\omega)t}$ and $e^{i(\omega_{21}+\omega)t}$ do not significantly affect the evolution of the system and thus can be omitted. This

is called the rotating-wave approximation and it gives us

$$\frac{d}{dt}c_1(t) = \frac{i\Omega_R}{2}c_2(t)e^{i\delta t}, \tag{2.12}$$

$$\frac{d}{dt}c_2(t) = \frac{i\Omega_R}{2}c_1(t)e^{-i\delta t}; \tag{2.13}$$

where we introduced the detuning $\delta = \omega - \omega_{21}$.

In the resonant case, $\delta = \omega - \omega_{21} = 0$, these equations have simple solutions in trigonometrical functions. For the initial condition $c_1(0) = 1$, $c_1(0) = 0$, the probability of the population transfer at a moment of time t is given by

$$p_2 = |c_2|^2 = \sin^2\left(\frac{\Omega_R t}{2}\right). \tag{2.14}$$

In the non-resonant case ($\delta \neq 0$), we can solve the system of equations 2.12 and 2.13 with the substitution $\widetilde{c_1}(t) = c_1(t)e^{-i\frac{\delta t}{2}}$, $\widetilde{c_2}(t) = c_2(t)e^{i\frac{\delta t}{2}}$:

$$\frac{d}{dt}\widetilde{c_1}(t) = -\frac{i\delta}{2}\widetilde{c_1}(t) + \frac{i\Omega_R}{2}\widetilde{c_2}(t), \tag{2.15}$$

$$\frac{d}{dt}\widetilde{c_2}(t) = \frac{i\Omega_R}{2}\widetilde{c_1}(t) + \frac{i\delta}{2}\widetilde{c_2}(t). \tag{2.16}$$

We obtain a system of ordinary differential equations in the form of $\frac{d}{dt}\widetilde{\mathbf{c}}(t) = A * \widetilde{\mathbf{c}}(t)$, which has solution in a the form of a matrix exponent $\widetilde{\mathbf{c}}(t) = \exp(At) * \widetilde{\mathbf{c}}(0)$. For the same initial conditions as before, the solution is

$$\widetilde{c_1}(t) = \cos\left(\frac{\Omega t}{2}\right) + i\frac{\delta}{\Omega}\sin\left(\frac{\Omega t}{2}\right), \tag{2.17}$$

$$\widetilde{c_2}(t) = i\frac{\Omega_R}{\Omega}\sin\left(\frac{\Omega t}{2}\right); \tag{2.18}$$

where $\Omega = \sqrt{\Omega_R^2 + \delta^2}$ is a generalized Rabi frequency. The result implies that, in the case of detuning, a two-level atom experiences partial state transfer between the levels, at a higher oscillation frequency (as shown in Figure 2.2). This result will be the same if we consider the interaction between an oscillating linearly polarized magnetic field $\mathbf{b}$ and atomic magnetic moment $\boldsymbol{\mu}$. In this case the Rabi frequency is $\Omega_R = \langle 1| \hat{\boldsymbol{\mu}} \cdot \mathbf{b} |2\rangle$.

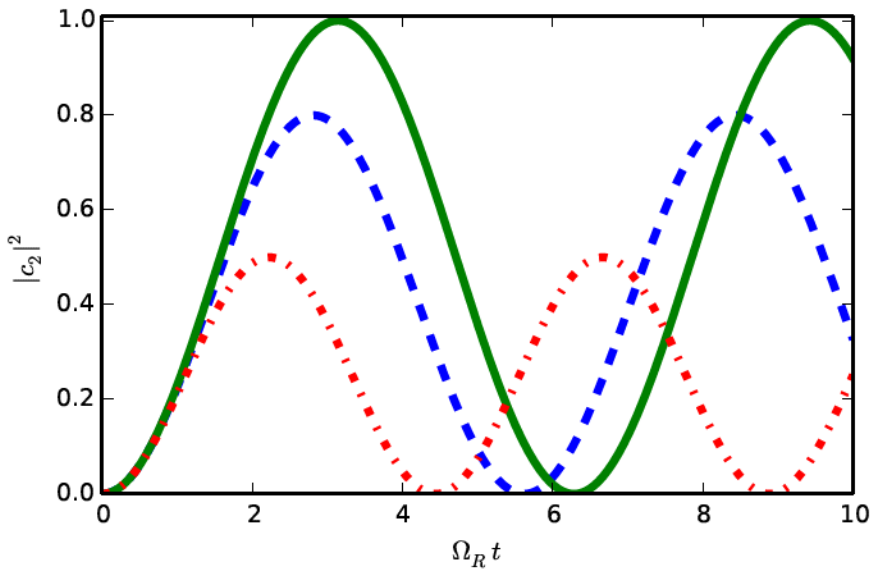

Figure 2.2: Rabi oscillations of the excited state population as function of time for an atom starting in the ground state for different values of the detuning δ. Green solid curve: $\delta = 0$, blue dashed curve: $\delta = 0.5\ \Omega_R$, red dash-dotted curve: $\delta = -\Omega_R$.

2.1.2 Optical Bloch equations without damping

In the preceding section we did not take into account spontaneous emission, which is a reasonable approximation for magnetic-dipole transitions. For electric-dipole transitions, spontaneous emission can be introduced phenomenologically, if we apply a density matrix formalism to describe the problem.

If we start with a pure state $|\psi\rangle = \widetilde{c_1}\,|1\rangle + \widetilde{c_2}\,|2\rangle$ as before, the corresponding density matrix can be expressed as the outer product

$$\rho = |\psi\rangle\langle\psi| = \begin{pmatrix} |\widetilde{c_1}|^2 & \widetilde{c_1}\widetilde{c_2}^* \\ \widetilde{c_1}^*\widetilde{c_2} & |\widetilde{c_2}|^2 \end{pmatrix} \equiv \begin{pmatrix} \widetilde{\rho}_{11} & \widetilde{\rho}_{12} \\ \widetilde{\rho}_{21} & \widetilde{\rho}_{22} \end{pmatrix}, \tag{2.19}$$

where the coefficients $\widetilde{\rho}_{11} = \rho_{11}$ and $\widetilde{\rho}_{22} = \rho_{22}$ are called *populations* and $\widetilde{\rho}_{12} = (\widetilde{\rho}_{21})^* = e^{-i\delta t}\rho_{12}$ are called *coherences*.

Now, we rewrite evolution equations in terms of the density matrix elements, using equations 2.15 and 2.16:

$$\frac{d}{dt}\widetilde{\rho}_{11} = \frac{d}{dt}(\widetilde{c_1}\widetilde{c_1}^*) = i\frac{\Omega_R}{2}(\widetilde{\rho}_{21} - \widetilde{\rho}_{12}), \tag{2.20}$$

$$\frac{d}{dt}\widetilde{\rho}_{22} = -\frac{d}{dt}\widetilde{\rho}_{11} = i\frac{\Omega_R}{2}(\widetilde{\rho}_{12} - \widetilde{\rho}_{21}), \tag{2.21}$$

$$\frac{d}{dt}\widetilde{\rho}_{12} = \frac{d}{dt}(\widetilde{c}_1\widetilde{c}_2{}^*) = -i\delta\widetilde{\rho}_{12} + i\frac{\Omega_R}{2}(\widetilde{\rho}_{22} - \widetilde{\rho}_{11}). \tag{2.22}$$

$$\frac{d}{dt}\widetilde{\rho}_{12} = \frac{d}{dt}(\widetilde{c}_2\widetilde{c}_1{}^*) = i\delta\widetilde{\rho}_{21} - i\frac{\Omega_R}{2}(\widetilde{\rho}_{22} - \widetilde{\rho}_{11}). \tag{2.23}$$

2.1.3 Optical Bloch equations with damping

The phenomenological damping term can be guessed from the exponential nature of spontaneous emission: $\rho_{22}(t) = \rho_{22}(0)e^{-\Gamma t}$, which implies that $c_1(t) = c_1(0)e^{-\Gamma t/2}$ (this result can be obtained rigorously from the Wigner-Weisskopf theory of spontaneous emission [35]). Thus, we can insert phenomenological damping terms for $\frac{d}{dt}\widetilde{\rho}_{22}$, $\frac{d}{dt}\widetilde{\rho}_{12}$ and $\widetilde{\rho}_{21}$ as $-\Gamma\widetilde{\rho}_{22}$, $-(\Gamma/2)\widetilde{\rho}_{12}$ and $-(\Gamma/2)\widetilde{\rho}_{21}$, respectively. Since the trace of a density matrix is always equal to one, the $\Gamma\widetilde{\rho}_{22}$ term should be added to the equation for $\frac{d}{dt}\widetilde{\rho}_{11}$. This leads us to the optical Bloch equation with damping:

$$\frac{d}{dt}\widetilde{\rho}_{11} = i\frac{\Omega_R}{2}(\widetilde{\rho}_{21} - \widetilde{\rho}_{12}) + \Gamma\widetilde{\rho}_{22}, \tag{2.24}$$

$$\frac{d}{dt}\widetilde{\rho}_{22} = i\frac{\Omega_R}{2}(\widetilde{\rho}_{12} - \widetilde{\rho}_{21}) - \Gamma\widetilde{\rho}_{22}, \tag{2.25}$$

$$\frac{d}{dt}\widetilde{\rho}_{12} = -(\frac{\Gamma}{2} + i\delta)\widetilde{\rho}_{12} + i\frac{\Omega_R}{2}(\widetilde{\rho}_{22} - \widetilde{\rho}_{11}). \tag{2.26}$$

$$\frac{d}{dt}\widetilde{\rho}_{21} = -(\frac{\Gamma}{2} - i\delta)\widetilde{\rho}_{21} - i\frac{\Omega_R}{2}(\widetilde{\rho}_{22} - \widetilde{\rho}_{11}). \tag{2.27}$$

The numerical solution of these equations for different parameters, in terms of the population of the excited state ρ_{22}, is depicted in Figure 2.3. The population reaches steady state after several Rabi oscillations in the underdamped case ($\Omega_R \gg \Gamma$) or directly in the overdamped case ($\Omega_R \ll \Gamma$).

2.1.4 Steady-state solution

The steady-state values depend on the system's parameters and can be found from the *steady state* solution of the equations (2.24)-(2.27), where the left-hand side is set to zero. Before we

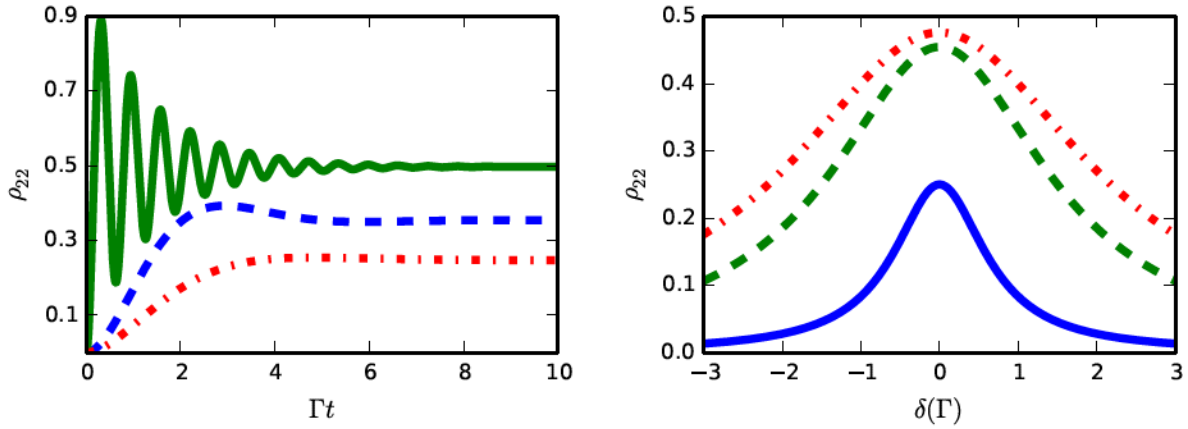

Figure 2.3: **Left**: excited state population as a function of time for an atom starting in the ground state. Green solid curve: $\Omega_R = 10\ \Gamma$, blue dashed curve: $\Omega_R = 1.1\ \Gamma$, red dash-dotted curve: $\Omega_R = 0.7\ \Gamma$. **Right**: steady-state excited state population as a function of the detuning (in units of Γ). Blue solid curve: $s_0 = 1$, green dashed curve: $s_0 = 10$, red dash-dotted curve: $s_0 = 20$.

proceed, let us simplify the notation. Due to the constrains $\widetilde{\rho}_{11} + \widetilde{\rho}_{22} = 1$ and $\widetilde{\rho}_{12} = (\widetilde{\rho}_{21})^*$ there are only two independent equations. By subtracting 2.24 from 2.25 and introducing the population inversion $w = \widetilde{\rho}_{22} + \widetilde{\rho}_{11}$, we can rewrite the optical Bloch equations with damping in the following way:

$$\frac{d}{dt}\widetilde{\rho}_{21} = (\frac{\Gamma}{2} - i\delta)\widetilde{\rho}_{21} - i\frac{\Omega_R}{2}w, \tag{2.28}$$

$$\frac{d}{dt}w = -\Gamma(w+1) - i\Omega_R(\widetilde{\rho}_{21} - \widetilde{\rho}_{12}). \tag{2.29}$$

Setting the left-hand sides of equations (2.28) and (2.29) to zero and solving the system gives us the following steady-state solution:

$$w = -\frac{1}{1+s}, \tag{2.30}$$

$$\widetilde{\rho}_{21} = \frac{i\Omega_R}{(\Gamma - 2i\delta)(1+s)}, \tag{2.31}$$

where

$$s = \frac{\Omega_R^2/2}{\delta^2 + (\Gamma/2)^2} = \frac{s_0}{1 + 4(\delta/\Gamma)^2} \tag{2.32}$$

is called the saturation parameter and $s_0 = 2\Omega_R^2/\Gamma^2$ is the resonant saturation parameter.

Finally, from the equation (2.30) the excited state population is

$$\rho_{22} = \frac{1}{2}(1+w) = \frac{1}{2}\frac{s_0}{1+s_0+(4\delta^2/\Gamma^2)} = \frac{1}{2}\frac{I/I_s}{1+I/I_s+(4\delta^2/\Gamma^2)}, \tag{2.33}$$

where in the third equality we used the fact that the saturation parameter is proportional to the light intensity I: $s \sim \Omega_R^2 \sim |\mathbf{E}|^2 \sim I$. The proportionality factor I_s is called *saturation intensity*. The steady-state population ρ_{22} as a function of the detuning for different values of the saturation parameter is presented in Figure 2.3.

Equation (2.33) has the two following limits:

1) Low intensity: $s_0 = I/I_s \ll 1$. In this limit $\rho_{22} \sim 0$ and the atom remains in its ground state. This corresponds to the over-damped regime of a harmonic oscillator with damping.

2) High intensity: $s_0 = I/I_s \gg 1$. In this limit $\rho_{22} \to 1/2$, which reflects that it is not possible to create a population inversion in a two-level system.

Finally, the scattering force as a function of detuning can be written as

$$F_s(\delta) = \hbar k \Gamma \rho_{22}(\delta) = \frac{\hbar k \Gamma}{2}\frac{I/I_s}{1+I/I_s+(4\delta^2/\Gamma^2)}. \tag{2.34}$$

2.1.5 Optical Bloch equations in terms of the Bloch vector

In some cases (e.g. for numerical integration) it might be more convenient to rewrite the equations (2.28)-(2.29) in terms of real-valued variables. This can be done by introducing $u = \widetilde{\rho}_{12} + \widetilde{\rho}_{21}$ and $v = i(\widetilde{\rho}_{21} - \widetilde{\rho}_{12})$:

$$\frac{d}{dt}u = \delta v - \frac{\Gamma}{2}u, \tag{2.35}$$

$$\frac{d}{dt}v = -\delta u + \Omega_R w - \frac{\Gamma}{2}v, \tag{2.36}$$

$$\frac{d}{dt}w = -\Omega_R v - \Gamma(w+1). \tag{2.37}$$

It can be shown that without spontaneous emission these equations describe the precession of the vector (v, u, w) around axis $(\Omega_R, 0, \delta)$ with frequency $\Omega = \sqrt{\Omega_R^2 + \delta^2}$. This vector is usually called the Bloch vector.

2.2 ^{87}Rb-level structure.

In this section, we discuss the fine and hyperfine structure of energy levels in hydrogen-like atoms and alkalis in general, and ^{87}Rb in particular.

2.2.1 Quantum defect in alkali metals

Alkali metals have a single valence s-electron outside a set of fully filled electronic shells. Generally, the electrons in the filled shells are not perturbed by external fields and thus do not participate in optical transitions. These electrons create a spherically symmetric electric field outside of the shell which screens the nuclear electric field, leading to hydrogen-like wave functions of the valence electron. The energy of this electron is similar to that of hydrogen-like atoms with a correction due to non-zero probability of being inside the "screen". Quantitatively it can be described by Rydberg's formula with the quantum defect δ_L [36]:

$$E(n, L) = -hc\frac{R_\infty}{(n - \delta_L)^2}, \tag{2.38}$$

where n is the principal quantum number and R_∞ is Rydberg's constant. Since the probability of penetrating the screen depends on the shape of the wavefunction, the quantum defect depends on the orbital quantum number L, thus removing the degeneracy with respect to the orbital angular momentum. For the ground state of Rb atoms, the value of the quantum defect is $\delta_S = 3.19$ [36].

2.2.2 Fine structure of atoms

Considering first-order relativistic corrections to the electron's energy in an atom leads to the following Hamiltonian [37]:

$$\hat{H} = \hat{H}_0 - \frac{\hat{p}^4}{8m^3c^2} + \frac{1}{2m^2c^2}\frac{1}{r}\frac{dV(r)}{dr}\hat{\mathbf{L}}\cdot\hat{\mathbf{S}} + \frac{\hbar^2}{8m^2c^2}\Delta_{\mathbf{r}}V(r), \tag{2.39}$$

where $\hat{p}$, r, and $V(r)$ correspond to the electron's momentum, position and potential energy,respectively, and operators $\hat{\mathbf{L}}$ and $\hat{\mathbf{S}}$ describe the electron's angular momentum associated with its orbital motion and spin, respectively. The first and second terms in (2.39) refer to the non-relativistic energy and the first-order relativistic correction to the kinetic energy, respectively. The third takes into account the spin-orbit coupling, which is the interaction between the electron's magnetic moment associated with its spin and the effective magnetic field as a result of the electron's motion in

an inhomogeneous electrostatic field. The last one is the Darwin term describing energy of the Zitterbewegung or "trembling motion" of the electron about its position $\mathbf{r}$ [38].

The second, third, and fourth terms scale as $\alpha^2 = \left(\frac{1}{4\pi\varepsilon_0}\frac{e^2}{\hbar c}\right)^2 = \left(\frac{1}{137}\right)^2$ with respect to $\hat{H}_0$. The spin-orbit coupling term removes the degeneracy with respect to L, thus giving rise to the fine structure of atoms.

2.2.3 Hyperfine structure of atoms

The total energy of an atom is affected by its nuclear spin $\mathbf{I}$, interacting with magnetic moment associated with the electron's spin and the magnetic field created by the electronic orbital motion. This energy correction can be expressed in terms of the total angular momentum of the electron $\mathbf{J} = \mathbf{L} + \mathbf{S}$ and the nuclear spin [39]:

$$\hat{H}_{HF} = A\mathbf{I} \cdot \mathbf{J}, \tag{2.40}$$

where $A(n, L, J)$ is the hyperfine constant. This interaction leads to the separation between levels corresponding to different values of the total angular momentum of an atom $\mathbf{F} = \mathbf{J} + \mathbf{I}$ giving rise, to the hyperfine structure of atoms.

2.2.4 Hyperfine structure of ^{87}Rb

^{87}Rb isotopes have nuclear spin $I = 3/2$. In a combination with the spin of a single valence electron, there are two ground-state levels in the hyperfine structure with $F = 1$ and $F = 2$ connected by a long-lived magnetic-dipole transition. In the first excited state, the absolute value of the vector sum of the electron's spin and orbital angular momentum can have two values providing two optical transitions in the fine structure: $5^2\boldsymbol{P}_{1/2} \rightarrow 5^2\boldsymbol{S}_{1/2}$ (D_1-line) and $5^2\boldsymbol{P}_{3/2} \rightarrow 5^2\boldsymbol{S}_{1/2}$ (D_2-line). The hyperfine structure corresponding to the D_2-line used in our experiment is presented in Figure 2.4.

2.3 Level splitting in a magnetostatic field: Zeeman effect and magnetic trapping

Most atoms have an intrinsic permanent magnetic dipole moment $\boldsymbol{\mu}$ proportional to the total angular momentum $\mathbf{F}$. Interaction between $\boldsymbol{\mu}$ and an external static magnetic field shifts the atomic energy depending on the magnetic number m_F, the phenomenon called the Zeeman effect.

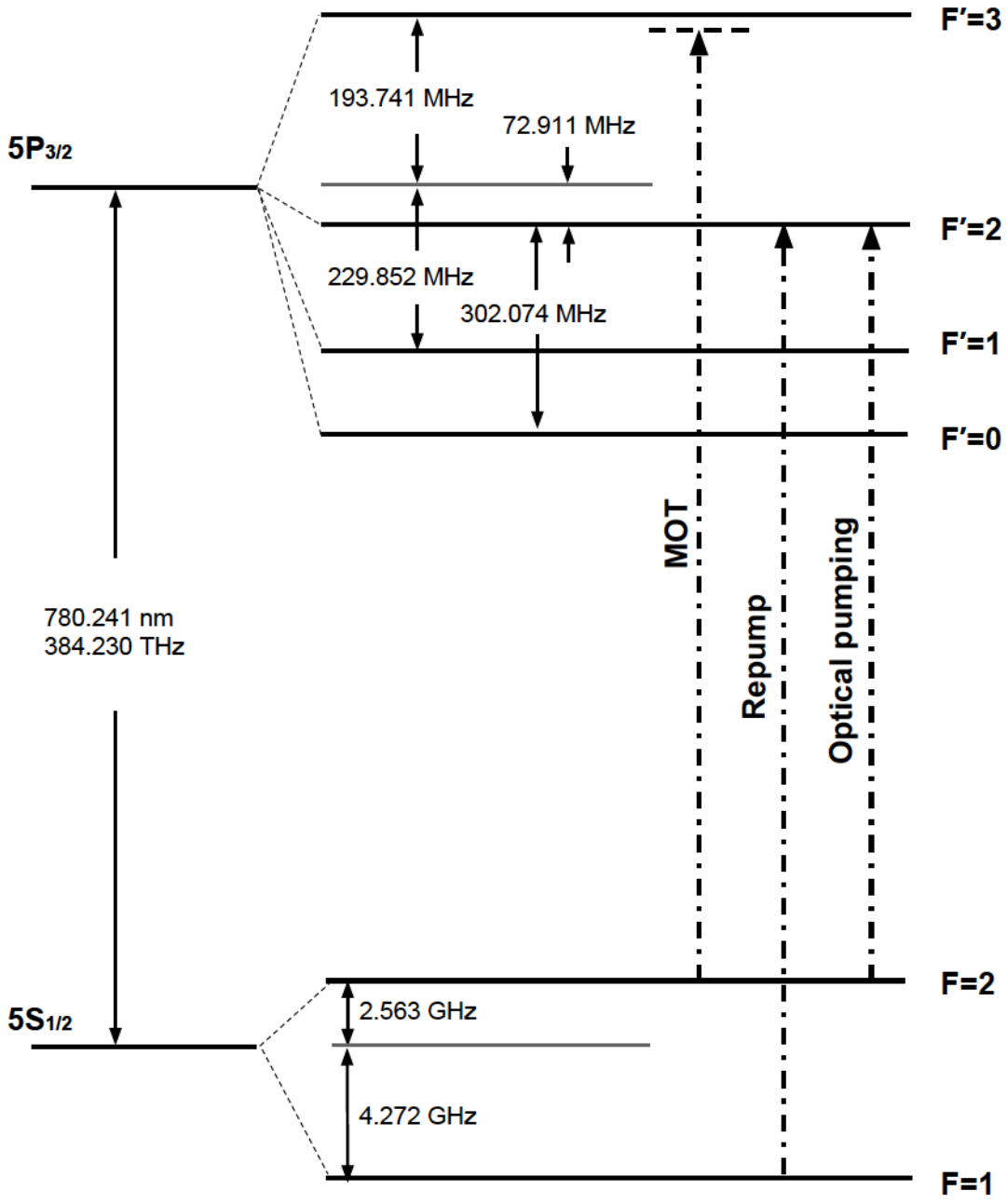

Figure 2.4: Hyperfine structure associated with D_2-line transitions in ^{87}Rb used in the experiment (see section 3.4). Adapted from [40]).

Experimentally, this effect is used for magnetic trapping, evaporative cooling and optical pumping. A semi-classical operator describing this effect for a single-electron atom can be expressed in the following way [41]:

$$\hat{H}_Z = -\hat{\boldsymbol{\mu}} \cdot \mathbf{B} = -(\hat{\boldsymbol{\mu}}_S + \hat{\boldsymbol{\mu}}_L + \hat{\boldsymbol{\mu}}_I) \cdot \mathbf{B} = -\frac{\mu_B}{\hbar}(g_s \hat{\mathbf{S}} + g_L \hat{\mathbf{L}}) \cdot \mathbf{B} - \frac{\mu_N}{\hbar} g_I \hat{\mathbf{I}} \cdot \mathbf{B} \approx \frac{\mu_B}{\hbar}(2\hat{\mathbf{S}} + \hat{\mathbf{L}}) \cdot \mathbf{B}, \quad (2.41)$$

where we write the total magnetic moment in terms of the contributions from spin $\mathbf{S}$, orbital momentum $\mathbf{L}$, and the total nuclear spin $\mathbf{I}$. In the last equality, we used $g_L = -1$ and $g_S = -2$ for the orbit and spin gyromagnetic ratios respectively, and neglected the nuclear terms, since the nuclear magneton μ_N is much smaller than Bohr's magneton μ_B.

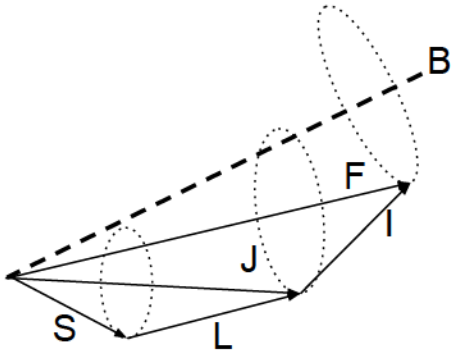

Figure 2.5: Vector diagram representation of the Zeeman effect. In the **LS**-scheme, vectors **S** and **L** rapidly revolve about the vector of total electronic angular momentum **J**. In the **IJ**-scheme **I** and **J** rapidly evolve around **F** which precesses slowly about magnetic field vector **B**.

If the magnetic shift is smaller than the hyperfine splitting, **L** and **S** need to be expressed in terms of F and m_F numbers. We assume that the nuclear spin **I** and the total electron angular momentum $\mathbf{J} = \mathbf{L} + \mathbf{S}$ rotate rapidly about **F** while the electron orbital angular momentum **L** and spin **S** rotates rapidly around **J** corresponding to the **IJ** and **LS** coupling schemes respectively [39,42]. Meanwhile, **F** precesses slowly around the magnetic field axis as depicted by Figure 2.5.

In this treatment we need to rewrite **S** and **L** in terms of their projections on **J**, accordingly to the projection theorem [37]

$$\mathbf{S} \to \frac{\langle \hat{\mathbf{S}} \cdot \hat{\mathbf{J}} \rangle}{\langle \hat{\mathbf{J}}^2 \rangle} \hat{\mathbf{J}} = \frac{\langle \hat{\mathbf{S}}^2 \rangle + \langle \hat{\mathbf{S}} \cdot \hat{\mathbf{L}} \rangle}{\langle \hat{\mathbf{J}}^2 \rangle} \hat{\mathbf{J}} = \frac{J(J+1) + S(S+1) - L(L+1)}{2J(J+1)} \hat{\mathbf{J}}, \quad (2.42)$$

$$\mathbf{L} \to \frac{\langle \hat{\mathbf{L}} \cdot \hat{\mathbf{J}} \rangle}{\langle \hat{\mathbf{J}}^2 \rangle} \hat{\mathbf{J}} = \frac{\langle \hat{\mathbf{L}}^2 \rangle + \langle \hat{\mathbf{L}} \cdot \hat{\mathbf{S}} \rangle}{\langle \hat{\mathbf{J}}^2 \rangle} \hat{\mathbf{J}} = \frac{J(J+1) + L(L+1) - S(S+1)}{2J(J+1)} \hat{\mathbf{J}}, \tag{2.43}$$

$$\mathbf{J} \to \frac{\langle \hat{\mathbf{J}} \cdot \hat{\mathbf{F}} \rangle}{\langle \hat{\mathbf{F}}^2 \rangle} \hat{\mathbf{F}} = \frac{\langle \hat{\mathbf{J}}^2 \rangle + \langle \hat{\mathbf{J}} \cdot \hat{\mathbf{I}} \rangle}{\langle \hat{\mathbf{F}}^2 \rangle} \hat{\mathbf{F}} = \frac{F(F+1) + J(J+1) - I(I+1)}{2F(F+1)} \hat{\mathbf{F}}, \tag{2.44}$$

Substituting equations (2.42-2.44) into (2.41) gives us

$$\hat{H}_Z = \frac{g_F \mu_B B \hat{F}_z}{\hbar}, \tag{2.45}$$

$$\Delta E_Z = \langle \hat{H}_Z \rangle = g_F \mu_B m_F B; \tag{2.46}$$

where the operator $\hat{F}_Z$ corresponds to the projection of the vector $\mathbf{F}$ on the magnetic field axis z with eigenvalues of $\hbar m_F$. The g-factors are given by

$$g_F = g_J \frac{F(F+1) + J(J+1) - S(S+1)}{2F(F+1)} \tag{2.47}$$

and

$$g_J = 1 + \frac{J(J+1) + S(S+1) - L(L+1)}{2J(J+1)}. \tag{2.48}$$

According to expression (2.46), inhomogeneous magnetic field creates a potential well or a potential hill for an atom depending on the sign of $g_F m_F$, providing a tool for magnetic trapping of atoms. Since a static magnetic field cannot have a local 3D maximum in a current-free region [43], only atomic states for which $g_F m_F > 0$ are magnetically trappable. In general, an atom sees a changing quantization axis when moving through an inhomogeneous field, but if the atom moves slowly enough, its magnetic dipole follows the field vector adiabatically and maintains its m_F value. This adiabaticity cannot be achieved when the magnetic field is zero at its minimum, thus it is better to use magnetic traps with a non-zero minimum value if possible. Loss near the centre of the trap due to this mechanism is known as Majorana loss [44].

2.4 Level splitting in optical field: AC-Stark effect and optical dipole trap

The time-independent Hamiltonian associated with a two-level system in an optical field is described by equations (2.15) and (2.16) and can be written in a matrix form as

$$\hat{H} = \frac{1}{2}\begin{pmatrix} \hbar\delta & -\hbar\Omega_R \\ -\hbar\Omega_R & -\hbar\delta \end{pmatrix} \tag{2.49}$$

with eigenvalues

$$E_{\pm} = \pm\frac{\hbar}{2}\sqrt{\delta^2 + \Omega_R^2}. \tag{2.50}$$

The values from equation (2.50) correspond to the energy shift of two levels in a "dressed-atom" picture due to interaction with the light field [33], a phenomenon known as the AC-Stark effect. At large detuning $\delta \gg \Omega_R$ equation (2.50) becomes

$$E_{\pm} = \pm\frac{\hbar}{2}\delta\left(1 + \frac{\Omega_R^2}{2\delta^2}\right), \tag{2.51}$$

which is proportional to the optical field intensity. This result is rather qualitative, since we assumed large δ while expression (2.49) was derived in the rotating-wave approximation, which is a good assumption only for small values of detuning. Nevertheless, it shows that the force that the light exerts on the atom is proportional to the light's intensity gradient.

The same result can be obtained classically, assuming that the atomic electric dipole moment $\mathbf{d}$ induced by the light filed is proportional to its field strength $\mathbf{E}$:

$$\mathbf{d}(t) = \alpha\mathbf{E}(t) = \alpha\mathbf{E}_0\cos(\omega t), \tag{2.52}$$

where the proportionality coefficient α is the atomic polarizability and we keep in mind the dipole moment varies in time as the field oscillates. The force acting on the dipole is proportional to the field's gradient, which, averaged in time, gives us

$$\langle\mathbf{F}\rangle_t = \left\langle \mathbf{d}(t)\cdot\frac{d}{d\mathbf{r}}\mathbf{E}(t)\right\rangle_t = \alpha\left\langle \mathbf{E}(t)\cdot\frac{d}{d\mathbf{r}}\mathbf{E}(\mathbf{t})\right\rangle_t = \frac{\alpha}{4}\frac{d}{d\mathbf{r}}|\mathbf{E}_0|^2 = \frac{\alpha}{2c\varepsilon_0}\frac{d}{d\mathbf{r}}I. \tag{2.53}$$

For negative α, the optical dipole force points towards the intensity maximum and allows one to trap atoms in a laser focus, the technique known as optical dipole trapping.

Chapter 3

Experimental setup

In our experiment, we use a two-chamber setup, where the chip's location is different from the place where the ultracold gas is prepared. The experimental idea is to create the ultracold gas in the "preparation region", a rectangular glass cell (section 3.2.6) surrounded with optics (section 3.4) and magnetic-field coils (section 3.3), and then to move the sample to the "science chamber" for on-chip experiments via optical transport (section 3.6).

The system is kept all the time under ultrahigh vacuum condition necessary for ultracold gas experiments. The science chamber can be isolated from the rest of the system with a gate valve, which allows us to change chips without breaking vacuum in the preparation region. This prevents us from the necessity of baking out (section 3.1.2) the glass cell, which would require dismounting of all optics and magnetic coils, thereby making the design more versatile. Particular vacuum components are described in section 3.2. The imaging setup is discussed in section 3.5.

3.1 System preparation

3.1.1 Ultra-high vacuum component cleaning

To achieve ultra-high vacuum, all parts of the system should contain as little contamination as possible on their inner walls. To achieve this in our experiment we use the following cleaning sequence:

1) Sponge in hot tap water with a low foam powdered detergent.

2) Rinse with hot tap water.

3) Spray with acetone.

4) Spray with methanol.

5) Rinse with distilled water.

6) Let it dry, covered with lint-free tissues (Kim-wipes) to protect from dust. The presence of remaining liquids will slow down pumping significantly.

3.1.2 Baking

In order to get to a low base pressure, all parts of the system should be gradually heated up to temperature $150 - 200\ ^0$C, which dispenses contaminants (mostly trapped water and hydrogen) from the inner walls. During the whole process all parts of the system (including ion pumps) should be kept at about the same temperature in order to avoid redistribution of the contaminants to the colder parts. The uniform temperature can be achieved by wrapping the whole system in aluminium foil (baking).

Before baking we turned on a roughing pump (see section 3.2.1) and waited until the pressure in the system stopped changing significantly (usually leaving the pumping overnight is enough). The pressure measured with an ion gauge (see section 3.2.3) before the start of baking was on the order of 10^{-6} Torr. For the heating we wrapped all metallic parts with heater tapes directly, while for the glass cell we wrapped the tape around a metallic rectangular frame surrounding the cell. The current through the heating tapes was controlled with variable transformers (variacs). The temperature was measured with various type-K thermocouples attached to exposed metal and glass parts with a kapton tape. Aluminium foil was placed on top of the tape in a few layers.

At the beginning, increasing average temperature in the system by 5 ^{0}C led to a few orders of magnitude increase in the pressure. After some time, the pressure started dropping until it reached a new base value. After that, we increased the temperature. The maximal average temperature during the bake was about 180 ^{0}C with the glass cell and windows slightly colder then the rest of the system.

When the pressure at the maximum temperature dropped to 10^{-7} Torr, we turned the ion pumps on. The pressure went high for about 20 s and then was dropping constantly. When the pressure stabilized we started to lower the temperature gradually over a day. The base pressure after the baking was on the order of 10^{-10} Torr.

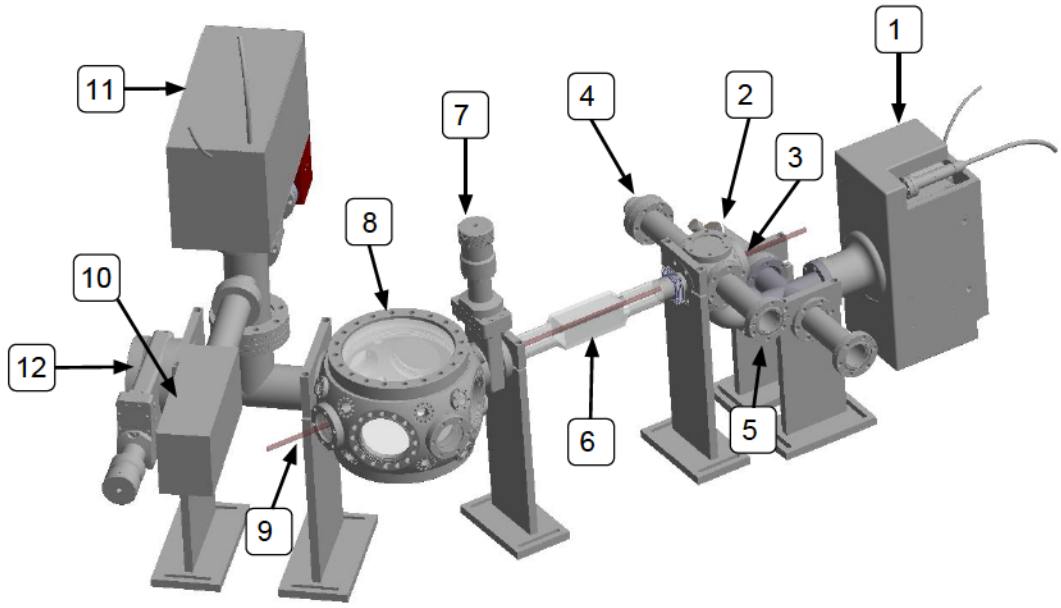

Figure 3.1: Vacuum assembly schematics. 1) 40 L/s Ion pump. 2) Angle valve. 3) Optical trapping beam input. 4) Rb dispenser's electric connections. 5) Observation window. 6) Preparation glass cell. 7) Gate valve to isolate preparation region from science chamber. 8) Science chamber. 9) Optical trapping beam output. 10) RGA. 11) 55 L/s Ion pump. 12) Gate valve to isolate science chamber from chip loading region. Red beam across the system represents the optical dipole trap. Figure was adapted from a 3D image made by L.J. LeBlanc.

3.2 Vacuum system components

In our experiment we use stainless steal vacuum parts from **MDC** and **Kimball**. The sealing is achieved with ConFlat flange technology, where each face of the assembled parts carries an edge that cuts through a soft metal gasket. Here, we use silver-coated copper gaskets from **Duniway Stockroom Corporation**. In order to achieve uniform penetration of the conflat knife-edge and to save it from bending, bolts around the flange circumference were tightened in a rotatory pattern. The assembled vacuum system with labelled parts is presented in Figure 3.1.

3.2.1 Pumping

For the roughing stage we use **TPS compact EX9698222** turbo pump from **Agilent Technologies**. At normal operation it works at a frequency of 960 Hz and power of 17 W. Turbo pump is connected to the system via an angle valve that can be seen in Figure 3.2. It pumps out gases

from the system to the atmosphere and becomes ineffective at low pressures.

For achieving ultra-high vacuum conditions after the roughing stage, we use 40 L/s and 55 L/s **Valcon Plus Starcell** ion pumps with **4UHV 929-400** controller from **Agilent Technologies**. Ion pumps ionize most of the atoms and molecules of the residual gases with electrons spinning in an inhomogeneous magnetic field created by strong permanent magnets. The ionized particles of the gases are then collected with the pump's cathode. Ion pumps become ineffective when contaminated, which happens fast at high pressures, and thus should be turned on only after the roughing stage.

To reduce the concentration of hydrogen, which is not trapped effectively by the ion pumps, we use a titanium sublimation pump from **Gamma Vacuum**. It sprays titanium inside the system, which covers the system's inner walls with a thin layer. The titanium layer effectively absorbs hydrogen molecules that collide with it.

3.2.2 UV-lights for light induced atom desorption

While the high background pressure of the Rb vapour is essential for the MOT stage, it is the main factor limiting the lifetime of the magnetic and optical dipole traps. A rapid switching "on" and "off" of the background pressure can be achieved with a light-induced atom desorption [45]. In this experiment we use **Marubeni L405-66-60-550** high-power 300 mW illuminators that radiate the preparation cell with 405 nm light. Turning them on for the MOT loading stage significantly increases the number of trapped atoms, while keeping the background pressure low during the later stages, when the lights are off.

3.2.3 Pressure measurements

In general, the pressure inside the system can be estimated from the value of the ionic current inside the ion pump. It gives a good measure of the pressure inside the pump, but it may differ from the values in other parts of the system, especially when the pump is contaminated. In this case we use a Bayard-Alpert ionization gauge from **SRS**. It ionizes near-coming atoms and molecules with electrons emitted from a hot filament and measures ionic current that is proportional to the total pressure.

In order to determine the abundance of different gases that are present in the system, we use a residual gas analyzer **RGA-100** from **SRS**. It uses a quadrupole mass spectrometer, that shows a partial pressure of components as a function of their mass. The RGA can also be used for a leak

detection in the system. In this case one needs to spray a He gas near the region of the suspected leak. A significant increase in He partial pressure will be a signature of the leak.

3.2.4 Dispensers

As a source of Rb in the experiment we use **SEAS Rb/NF/7/25** alkali metal dispensers. They contain stable salts that release Rb when heated at a rate proportional to the dispenser's temperature. We use electric current as a means of controlling the release rate. The dispensers are connected to a **Agilent 6541A** power supply via a **MDC 9112000 - 0268201 (made by Insulator Seal)** feed-through connector attached via in-line connectors **Accuglass 110113, 110111**. Even though the manufacturer gives a value of 5 A as the release threshold current, we found that running 4 A increases the background pressure by 10^{-9} Torr, which is sufficient for the purposes of the experiment.

3.2.5 Differential pumping tube

To maintain low background pressure in the science chamber while using the dispensers in the preparation region, we setup a differential pumping tube between this two regions. The tube sticks out in the direction of the preparation cell creating an obstruction for atoms coming to the science chamber. Our differential pumping tube is made of 316 stainless steel tubing.

3.2.6 Glass cell (preparation region)

For the preparation region, in which the ultracold gas is created, we use a rectangular cell with outer dimensions of $40 \times 40 \times 100$ mm made of the **Pyrex** glass by **Precision Glassblowing**. The cell has an anti-reflection coating for 780 nm light incident at right angle to a cell's face. One end of the cell is attached to metallic flexible bellows as shown in Figure 3.2. The bellows reduce tension in the glass during the mounting, thus keeping it from breaking. The preparation during the later stages of the experiment is shown in Figure 3.3

3.3 Magnetic fields system

3.3.1 Quadrupole magnetic field

Two magnetic coils with opposite currents (anti-Helmholtz configuration) create magnetic fields whose vectors point in opposite directions along the coils' axis and cancel each other in the middle.

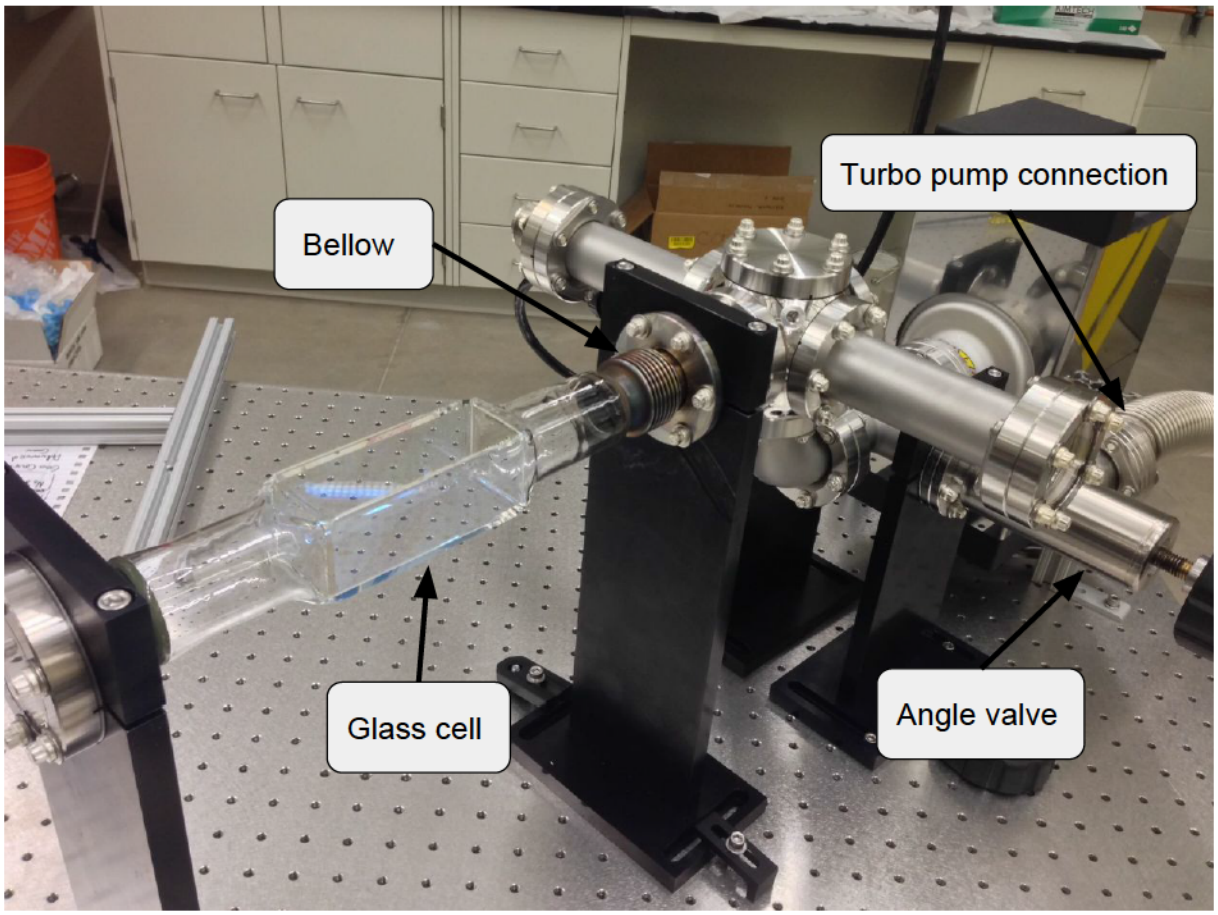

Figure 3.2: Preparation region during primary stages of assembling and testing.

This results in a quadrupole field with almost constant slope near the center (see Figure 3.4, left). Because of the axial symmetry, magnetic field gradients in radial directions are equal: $dB_x/dx = dB_y/dy$. Due to the non-divergence of magnetic fields, near zero the slope in longitudinal direction is two times larger than in radial direction. In our experiment a quadrupole magnetic field created by a pair of anti-Helmholtz coils is used for magneto-optical and magnetic trapping (see Chapter 4).

In the experiment we use a pair of coils that are formed with a kapton insulated hollow copper wire. It has a square cross-section with a 3/16 inch side and has hollow core with 3/32 inch in diameter. Each coil has an inner diameter of 120 mm, 6 turns in width and 4 turns in height. The coils have an inner separation of approximately 58 mm, and create a quadrupole magnetic field with a gradient of 0.197 G/cm·A in the radial direction and 0.42 G/cm·A in the longitudinal direction. The current used for magnetic trapping can go as high as 420 A for several seconds. Thus, to provide enough heat dissipation from the coils, we use a **Berkeley MGP70-02** booster pump to run cold water through the hollow part inside the wire.

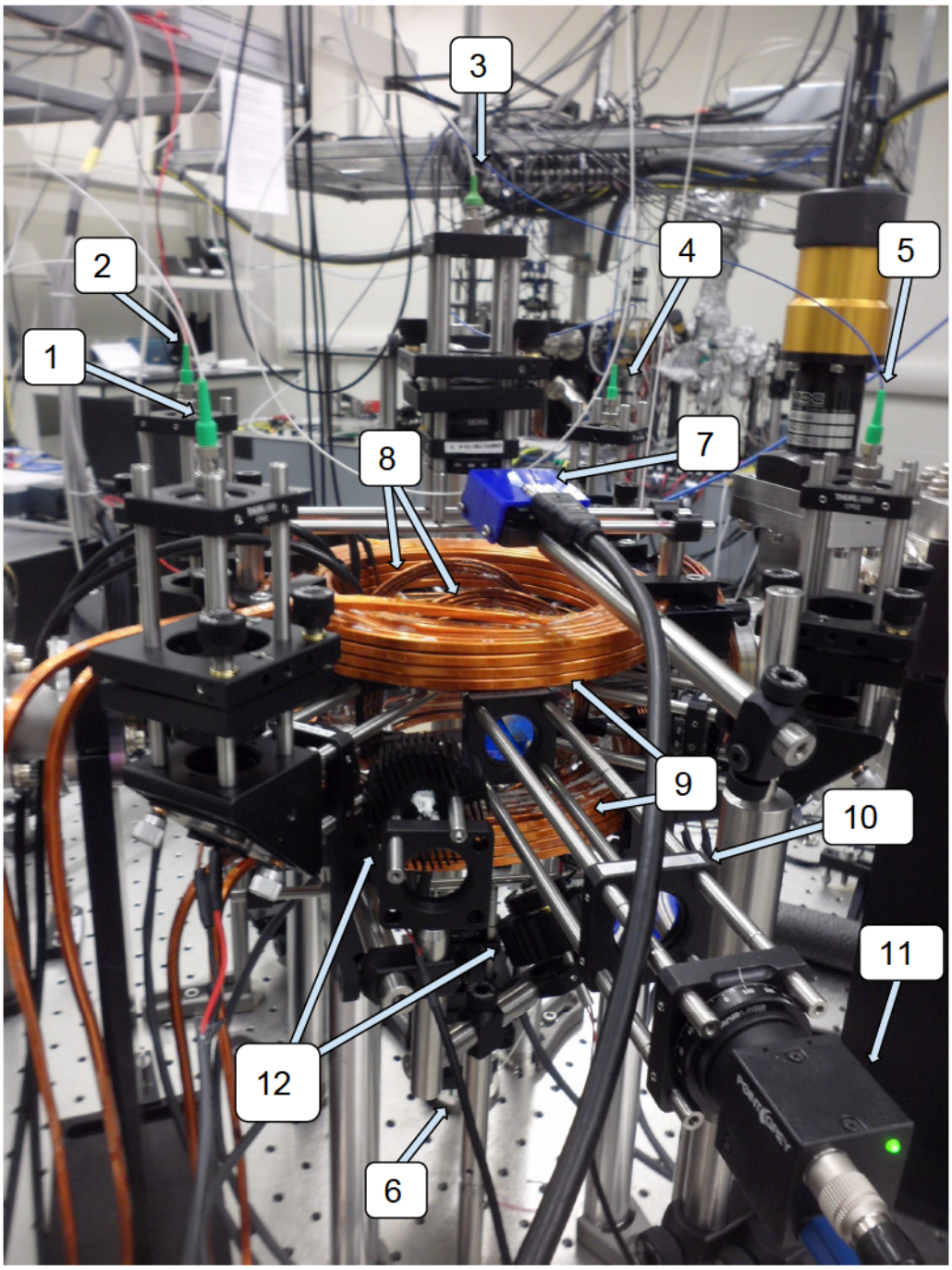

Figure 3.3: Preparation region at final stage. 1) South beam output. 2) West beam output. 3) Top beam output. 4) North beam output. 5) East beam output. 6) Bottom beam output. 7) IR Raspberry-Pi camera for continuous monitoring of the MOT (set up by Chenxi Huang). 8) y-bias field coils. 9) Quadrupole field coils. 10) Focusing system for absorption imaging. 11) CCD camera for absorption imaging. 12) UV-LEDs for induced desorption of ^{87}Rb.

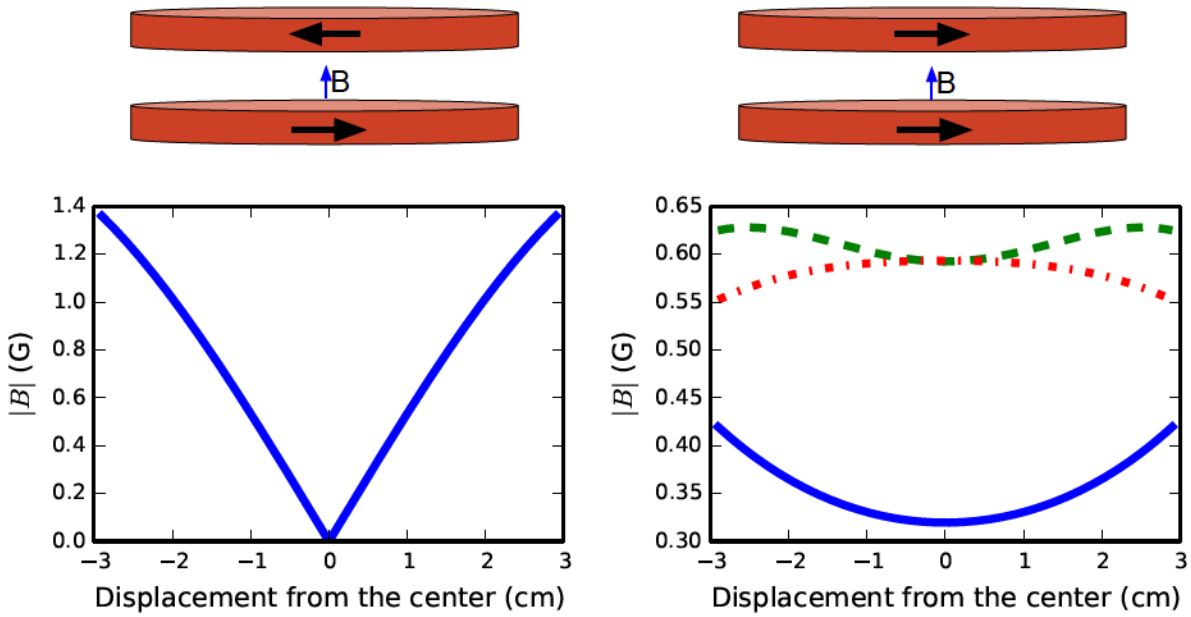

Figure 3.4: Magnetic field schematics and calculations for MOT/magnetic coils (left) and bias coils (right). **Left top**: Coils in an anti-Helmholtz configuration, as used for the MOT and magnetic trap. Black arrows indicate current direction. **Left bottom**: Magnitude of the magnetic field along a common axis between two anti-Helmholtz coils with parameters given in the text. The calculated field gradient is slightly different but close to the one given in the text (measured experimentally). **Right top**: Coils in a Helmholtz configuration, as used for 3 sets of bias coils. Black arrows indicate current direction. **Right bottom**: Magnitude of the magnetic field along a common axis between two Helmholtz coils with parameters given in Table 3.1. Blue solid curve corresponds to the x-coils, green dashed curve corresponds to the y-coils, red dash-dotted curve corresponds to the z-coils.

3.3.2 Bias field coils

In a Helmholtz configuration, both coils have the same electric current orientation and the vectors of the magnetic fields created by each coil add. At a point that is equally separated from both coils and is located on their common axis, the resulting field is nearly homogeneous (see Figure 3.4, right). In the experiment, homogeneous fields are used to shift the position of the minimum of the quadrupole magnetic field, to introduce a quantization axis for optical pumping (see section 4.2), and to eliminate background magnetic fields in the optical molasses.

In this experiment we use three pairs of coils in Helmholtz configuration along three mutually orthogonal spatial axes. All coils are made of 12 AWG insulated copper wire. The summary of the bias coils setup is presented in Table 3.1, where x corresponds to the glass cell's long axis and z is the vertical axis.

	x-bias	y-bias	z-bias
Turns in radial direction	4	4	1
Turns in axial direction	4	1	4
Coils separation (mm)	210	65	58
Inner diameter (mm)	100	100	128
Field in between (G/A)	0.32	0.6	0.6

Table 3.1: Bias field coil parameters.

3.3.3 Current control

To control the current in the quadrupole and bias field coils, we use the remote current control system depicted in Figure 3.5. It includes a servo with a negative feedback loop, a transistor bank and a DAQx that allows us to send an analog control signal from the computer. The transistor bank itself is a number of transistors connected in parallel in order to reduce the current running through each individual one. The number of transistors is determined by the their type and the maximal current in the circuit. To prevent the transistor from overheating they are placed onto an aluminium heatsink through which we run cold water. For a better contact with the heatsink we covered the transistors' bases with a thermal grease.

The schematic representation of the control circuit is given in Figure 3.5. The control signal from the computer is sent to the servo controller, where it is compared to a reading from a current sensor. The negative feedback loop in the servo matches these two signals by adjusting the voltage applied between the gate and the source of the transistor bank, which is connected in series with the coils. The result is a change in the resistance of the drain-source channel and the total current in the circuit.

In order to adjust for the coils' resistance changing in time due to heat dissipation, the power supply output voltage should exceed the value required by the Ohm's law. In general, the voltage can be set to a constant value, although working at high currents requires ability to control the voltage in order to protect the transistors from overheating, as described in section 3.3.3.

In our experiment we use one **Agilent 6651A** power supply for all three sets bias field coils. They do not require total current more then 15 A, so the voltage is set to 2 V during the whole experiment. Each set of bias coils is connected to a pair of transistors connected in parallel. All transistors share the same heatsink. For the quadrupole coils we use an **Agilent 6690A** power supply, which can provide up to 15 V and 450 A. Here we control the voltage remotely by applying

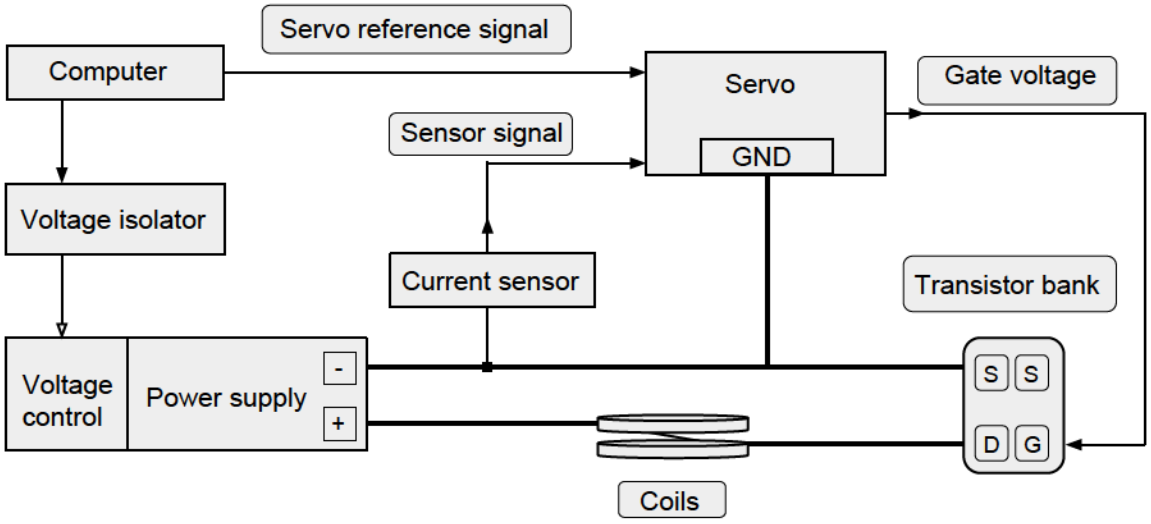

Figure 3.5: General purpose current control schematics. Solid lines represent current carrying wires, arrows represent electric potential with respect to the common ground (negative terminal of the power supply), empty arrow represents floating voltage.

an analogue voltage from a computer. We use a **Analog Devices AD210BN** transformer isolation amplifier to provide a floating control signal isolated from the load for the remote voltage control.

Optimal voltage for high currents

The transistor bank plays the role of a variable rheostat in which resistance is controlled with a signal from the servo applied to the gate. When the applied voltage V is equal or less than Ir, where I is the desired current set by the computer and r is the resistance of the load, the servo decreases the source-drain resistance R to a nearly-zero lowest possible value. In this case, almost no power is dissipated in the transistors.

For larger V the servo increases R until the current matches I. In this case, the power dissipation P is equal to

$$P(V) = I^2 R(V) = I(V - Ir). \tag{3.1}$$

Figure 3.6 shows the power dissipated by a transistor bank for different values of the set current I as a function of voltage applied to the circuit. The applied voltage should be adjusted according

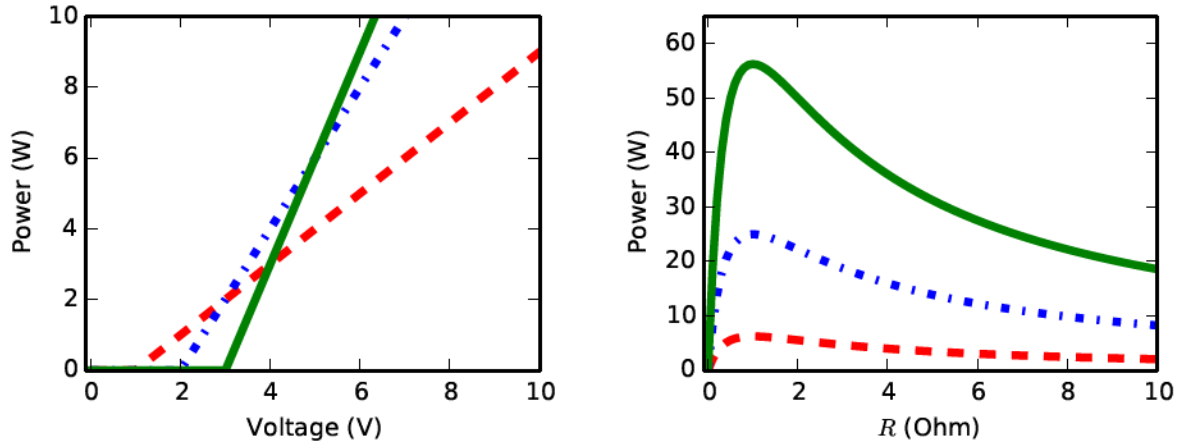

Figure 3.6: **Left**: Power dissipated in a transistor as a function of the voltage from the power supply for three different values of the required current. Green solid line corresponds to $I = 1$ A, blue dash-dotted to $I = 2$ A, red dashed to $I = 3$ A. Here the transistor resistance is adjusted for the set current. The resistance of the rest of the circuit is 1 Ω. **Right**: Power dissipation as a function of the transistor resistance at a constant current of 1 A for three different values of applied voltage. Green solid line corresponds to $V = 5$ V, blue dash-dotted to $V = 10$ V, red dashed to $V = 15$ V. The resistance of the rest of the circuit is 1 Ω.

to the set current values, since the same value, of e.g. 3.1 V, would lead to very small power in the case of 3 A and about 5 times larger power for 2 A.

So, ideally, we always want to apply voltage equal Ir, so the power dissipation in the transistors is minimal. The problem is that at high currents the coils' temperature changes significantly enough to cause increase in their resistance. In this case we want to add a ballast resistance by applying a larger V to the transistors to balance out this increase, so the total resistance is unchanged. This will provide a stable constant current during the experiment. At constant voltage-constant current regime, the transistor resistance decreases to compensate for the coil resistance growth. So, during this process the power dissipation is decreased.

Servo calibration

For servo controller calibration one should bear in mind the power has a non-linear dependence on the transistor resistance shown in Figure 3.6, with a maximal power dissipated when $R = r$. In our experiment the resistance of the quadrupole coils, including lead wires, is around 30 mΩ at room temperature, so the transistors' resistance should be to the right of the peak (in Figure 3.6 (right)) in order to provide enough ballast resistance. It is actually better to start with a larger ballast resistance to avoid the power peak.

3.3.4 Computer control

As a source of analog control voltage we use **NI-PCI-6733 National Instruments**, which is integrated with the control computer's motherboard, and **National Instruments BNC-2110** BNC interface. For digital control signals and experiment's sequence timing we use **PulseBlaster USBS/NC103** from **SpinCore**. All signals are controlled from a **LabView** project.

3.3.5 RF-field coils

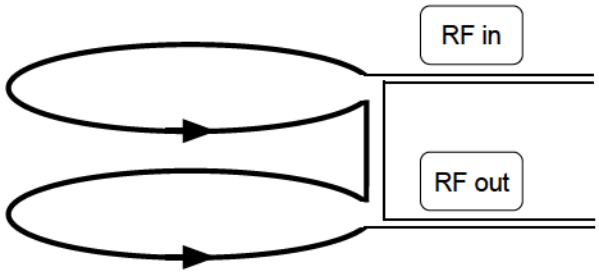

Figure 3.7: Schematics of the RF-coils connection.

Induced evaporative cooling (section 4.4) in a magnetic trap requires a linearly polarized magnetic field oscillating with a frequency in range between 10 MHz and 25 MHz. In order create this we use a pair of single-loop coils in Helmholtz configuration. They are connected to a **Novatech 409B/AC** frequency synthesizer with **OphirRF 5303055** amplifier via a BNC cable. The connection is schematically presented in Figure 3.7 The output cable can be connected to an oscilloscope to monitor the signal, left open, or terminated with a 50 Ω resistor.

3.4 Optics for laser cooling and trapping

For the magneto-optical trapping and laser cooling we use three pairs of counter-propagating beams of circularly polarized laser light, which are red-detuned from the $|F = 2\rangle \rightarrow |F' = 3\rangle$ transitions in ^{87}Rb (see Figure 2.4). The light at this frequency can lead to off-resonant $|F = 2\rangle \rightarrow |F' = 2\rangle$ transitions after which the atoms can decay to both $|F = 2\rangle$ and $|F = 1\rangle$ ground levels. Due to significant hyperfine splitting between these levels, the laser light becomes far off resonance for the atoms in the $|F = 1\rangle$ state and these atoms do not participate in laser cooling and magneto-optical trapping any longer. To put these atoms back to $|F = 2\rangle$ we use an additional *repump* light,

resonant with the $|F = 1\rangle \rightarrow |F' = 2\rangle$ transition to promote the atoms back into the cooling cycle.

The repump light comes from a **Toptica Photonics DL100** laser. Its frequency is locked by means of Doppler-free saturation spectroscopy [46] to 780.234 nm, corresponding to $|F = 1\rangle \rightarrow |F' = 2\rangle$ transition in ^{87}Rb. The output power of this laser is about 100 mW. For the magneto-optical trapping and laser cooling we use a **Toptica Photonics TApro** laser operating at 2 W of output power, which is red-detuned from the $|F = 2\rangle \rightarrow |F' = 3\rangle$ transition and locked through a beat-note to the repump laser at about 780.245 nm.

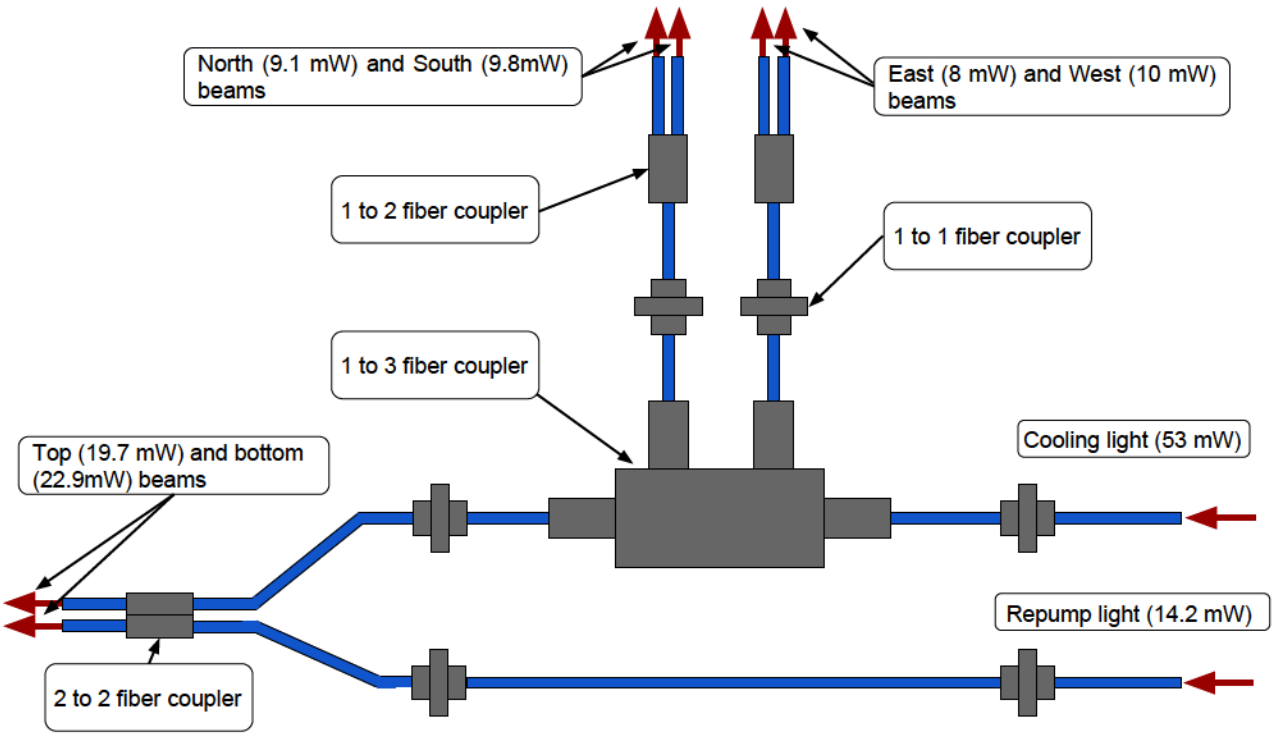

Figure 3.8: Fibers connection schematics for the cooling and the repump light.

Figure 3.8 shows details on how the light is divided between the beams. First, the cooling light is connected via optical fiber to an input of an **OZ optics FOBS-13P-1111-5/125-PPPP-40-3A3A3A3A-3-8,1** fiber coupler, which divides it into three beams of approximately equal intensity. After that, two of the outputs are divided into two beams each, using **Thorlabs PMC 780-50B-FC** fiber splitter. They enter the glass cell in the horizontal plane. The third output fiber is merged with a fiber with the repump light in an **OZ optics FUSED-22-780-5/125-50/50-3A3A3A3A-1-1** coupler with two inputs and two outputs. It divides light coming to each of its two inputs equally between two outputs. These two beams enter the glass cell from the top and bottom. Before the beams enter the glass cell, they are collimated with a 75 mm focal length lenses

and circularly polarized with $\lambda/4$ wave-plates.

3.5 Imaging and temperature measurements

3.5.1 Resonant absorption imaging

Resonant absorption imaging is an effective tool for probing ultracold gases experiments. It allows one to estimate the density distribution in an atomic cloud, its temperature and its phase-space density.

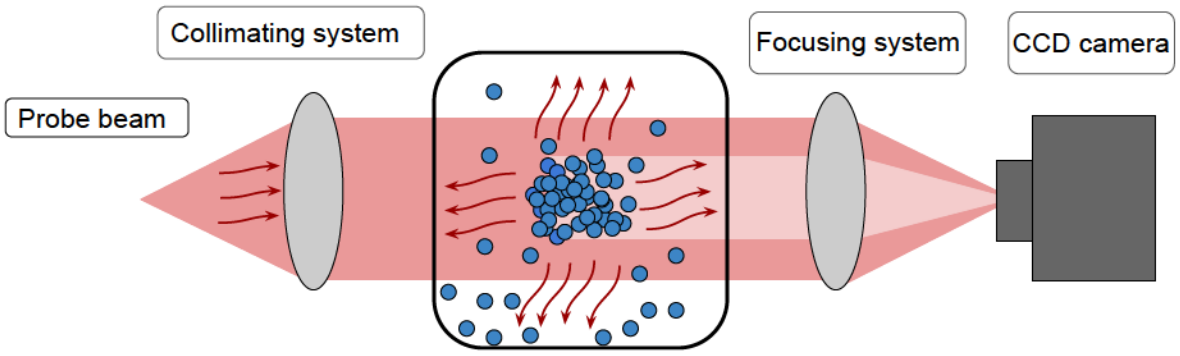

Figure 3.9: Absorption imaging schematics. Analyzing a shadow from atomic cloud in a resonant probe light allows to determine the density distribution in the cloud. For visibility the focusing system is schematically presented as a single lens instead of the telescopic system as is described in the text.

A resonant absorption imaging setup is illustrated in Figure 3.9. In this technique the sample atomic cloud is radiated by resonant light, which is then collected by a CCD camera. The amount of light absorbed and scattered per unit time in a thin layer of area A and thickness dx is

$$AdI = -\hbar\omega\Gamma_s nAdx, \tag{3.2}$$

where n is the density, and the minus-sign indicates that this light power is lost from the beam.

The factor $\hbar\omega\Gamma_s$ can be written in terms of intensity as $I\sigma_s$, where σ_s has units of area and corresponds to the scattering cross-section. Substituting this in (3.2) and integrating with respect to x gives

$$I(x) = I_0 \exp(-\sigma_s nx), \tag{3.3}$$

where I_0 is the intensity of the light before scattering. If we neglect the light that is scattered towards the camera, then the number of atoms met by the resonant light on its way to a single

camera pixel of area A_{pix} through the cloud region of thickness l is

$$N_{pix} = nlA_{pix} = \frac{A_{pix}}{\sigma_s} \ln \frac{I_0}{I(l)}. \tag{3.4}$$

Thus, knowing the pixel size, input intensity I_0 and intensity after scattering $I(l)$, we can determine the number of atoms in front of each pixel and reconstruct the density distribution in the cloud. Summing over the all pixels gives the total number of atoms seen by the camera $N = \Sigma N_{pix}$.

In our experiment we use three shots for absorption imaging. The first image is taken right after the cloud of interest was created and records the shadow from the cloud in the resonant imaging light. The second and third images are taken after the cloud is destroyed and measure the intensity of the non-scattered imaging beam, and the background level when no laser light comes into the imaging system, respectively.

3.5.2 Absorption imaging and optical pumping setup

In our experiment we shine a collimated beam of light resonant with one of the atomic transitions onto the atomic cloud from the side of the glass cell. The probe light goes across the glass cell and is scattered by the atomic cloud. The resulting shadow is then focused onto a CCD camera as is schematically shown in Figure 3.9. The focusing system and the CCD camera can be seen in Figure 3.3.

The collimation system consists of a single convex lens, whose focal point coincides with the output of the fiber with the imaging light. The focusing system consists of two convex lenses with equal focal lengths and can be seen at the front in Figure 3.3. The front lens' focal point is approximately at the middle of the glass cell, which is the expected location of the atomic cloud. The CCD camera is located at the rear focal point of the second lens. The separation between the lenses equals to the doubled focal length, which gives $1:1$ correspondence between the cloud and its image collected by the camera. In the case where magnification or demagnification are needed, lenses with focal lengths different from each other should be used.

The CCD camera that is used in this experiment is **Point Grey BFLY-U3**, connected to the main computer via USB cable. The camera is set to a trigger mode and is triggered with a digital voltage signal from the computer. In our experiment the set exposure time is 490 ms. To estimate the number of atoms in absorption imaging three pictures should be taken, as described above.

The probe light comes from the laser used for the cooling and trapping and is resonant with the

$|F = 2\rangle \rightarrow |F' = 3\rangle$ transition. The light intensity is lower than I_s to avoid saturation. It can be varied with an AOM to adjust for different cloud densities. For better imaging efficiency, the probe light is circularly polarized with a $\lambda/4$ wave-plate and a magnetic field is applied along the beam with the y-bias field coils. This set up is also used for the optical pumping at the $|F = 2\rangle \rightarrow |F' = 2\rangle$ transition.

Depending on the density of the observed cloud, in general, we use probe light at a power ranging from 1.29 μW to 29 μW.

3.5.3 Absorption spectroscopy

In early stages of the experiment, resonant absorption can be used to check that Rb vapours are present in the system, and that the laser light is tuned to the correct frequencies. In this technique a beam of probe light goes through the glass cell and then is collected by a photodiode or a powermeter. When the frequency of the probe light is close to one of the transitions in Rb, the vapor scatters more light and the resulting signal from the detector is decreased.

Figure 3.10 shows a dependence of the photodiode's signal on time, while sweeping the laser frequency around 780.24 nm. The signal was recorded with a digital oscilloscope. The bigger dip corresponds to the D2-line in ^{85}Rb ($5\mathbf{S}_{1/2} \rightarrow 5\mathbf{P}_{3/2}$ transition centred at 780.2414 nm [47]), the most abundant isotope of rubidium. The smaller dip corresponds to the D2-line in ^{87}Rb. From the absorption spectra it is clear that the pressure of ^{85}Rb dominates over ^{87}Rb, which is one of the main factors limiting life-times of magnetic and optical-dipole traps (see section 4.4).

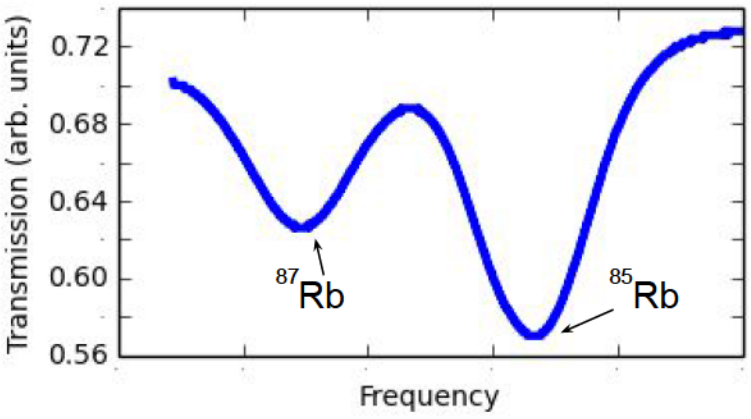

Figure 3.10: Transmitted signal from a frequency sweep in absorption spectroscopy measurement.

3.5.4 Free fall calibration

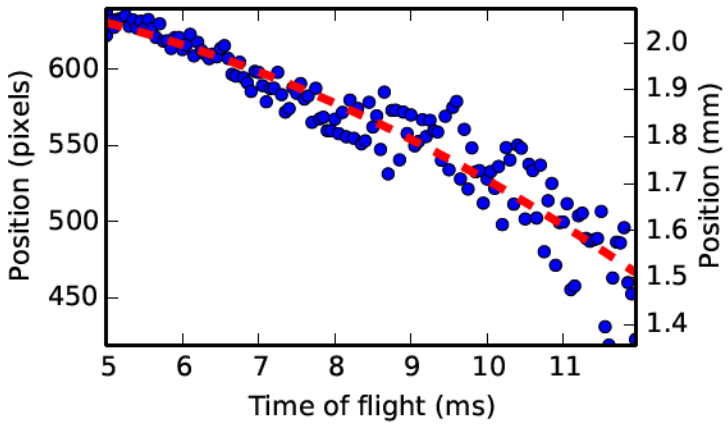

Figure 3.11: Position of the center of mass of the cloud released from a magneto-optical trap as a function of time. The dots correspond to the measured data, while the dashed line represents a quadratic fit. We start measuring at 5 ms of the flight, since this is how long it takes to open a shutter for the imaging beam. The acceleration is found to be -3000000 ± 700000 pixels/s^2, which gives an effective pixel size of 3.2 ± 0.8 μm.

In cases when the cloud is out of the focus of the imaging system, the cloud's image size is different from the cloud's real size, which leads to an incorrect temperature measurement. The imaging system can be calibrated by looking at the cloud's fall under the influence of gravity. Fitting the cloud's center of mass position as a function of the time of flight and comparing the fitting parameters with the free fall acceleration allows to establish effective pixel size of the image. Figure 3.11 shows the free fall of a cloud after magneto-optical trap. Comparing the fitting results with the knows value of the free fall acceleration gives the imaging system's magnification of 0.86.

3.5.5 Time-of-flight measurements

The temperature of an atomic cloud can be estimated by observing its expansion in a free fall after its release from a trap. During the flight, the original atomic momentum distribution is transferred into the density distribution in space.

To estimate the expected distribution we first consider a number of particles per unit of a 6-dimensional phase space [48]

$$dN(\mathbf{r},\mathbf{p}) = \frac{d\mathbf{r}d\mathbf{p}}{(2\pi\hbar)^3} f(\mathbf{r},\mathbf{p}), \tag{3.5}$$

where $f(\mathbf{r},\mathbf{p})$ is the distribution function. For a non-interacting gas in a potential $V(r)$ with a

temperature T we assume a Boltzmann distribution $f(\mathbf{r},\mathbf{p}) = \exp[-(p^2/2M + V(\mathbf{r}))/k_BT]$. The density distribution can be obtained by integrating (3.5) in the momentum subspace:

$$n(\mathbf{r}) = \int \frac{dN}{d\mathbf{r}} d\mathbf{p} = \int \frac{d\mathbf{p}}{(2\pi\hbar)^3} \exp\left[-\frac{1}{k_BT}\left(\frac{p^2}{2M} + V(\mathbf{r})\right)\right] = \left(\frac{Mk_BT}{2\pi\hbar^2}\right)^{3/2} \exp\left(-\frac{V(\mathbf{r})}{k_BT}\right). \quad (3.6)$$

In case of a harmonic potential $V(r) = (\omega_x x^2 + \omega_y y^2 + \omega_z z^2)/2M$, according to (3.6), one would expect the density distribution to be a Gaussian for non-interacting particles.

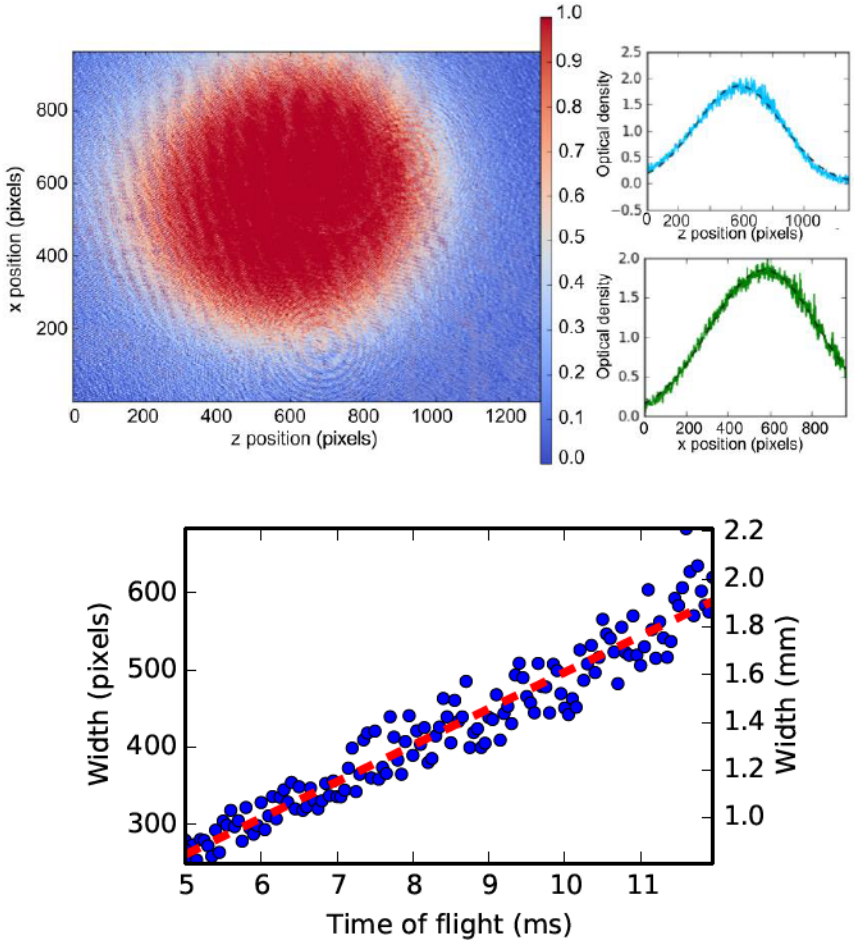

Figure 3.12: **Top left**: Absorption image of magneto-optical trap. Color-bar represents the optical density $n\sigma_s l$. **Top right**: Cross-section of optical density in x and y directions going through the image center. Black dashed curve corresponds to the Gaussian fit. **Bottom**: time-of-flight temperature measurement after magneto-optical trap. Slope from the linear fit (red-dashed line) is found to be 47000 ± 1000 pixels/s, which corresponds to the temperature of 240 ± 110 μK

Experiments show that an atomic cloud in a magneto-optical trap is nicely approximated by a Gaussian (see Figure 3.12, top). Since in an atomic cloud the inter-atomic interaction can not be

neglected, fitting the density distribution with (3.6) does not give a very precise estimate of the temperature. Instead, the temperature can be determined from the cloud's expansion measurements.

It was shown [49] that the cloud released from the trap maintains a Gaussian shape and, after some sufficiently long time $t \gg (\omega_x^2+\omega_y^2+\omega_z^2)^{-1/2}$, its width σ does not to depend on the particular parameters of the trap and is determined by the temperature:

$$\sigma(t) = \sqrt{\frac{k_B T}{M}} t. \tag{3.7}$$

Thus, the temperature can be estimated from a linear fit of the measured density-distribution width as a function of the time during the free expansion time (the time of flight).

3.6 Optical dipole trap and transport

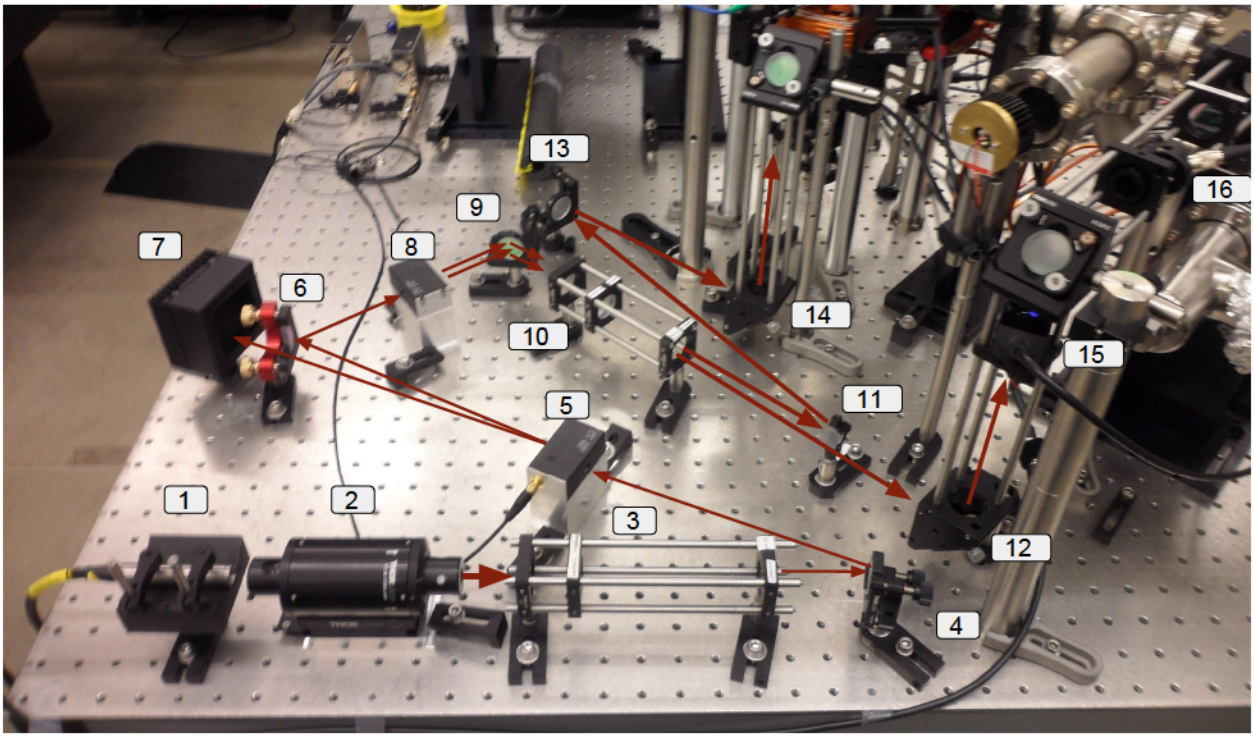

Figure 3.13: Setup for optical dipole trapping and transport. 1) 1064 nm laser output. 2) Optical isolator. 3) Demagnifying telescope. 4), 9), 13) C-coated mirrors. 5), 8) AOMs. 6), 11) D-shaped mirrors. 7) Beam block. 10) Magnifying telescope. 12), 14) Periscope entrance mirrors. 15), 16) focus tunable lenses.

The setup for the optical dipole trapping and transport is shown in Figure 3.13. First, the

light beam from a 1064 nm laser goes through a Faraday optical isolator, which prevents the light back-reflected from other optical parts from going back to the laser output. This protects the laser, when operating at high powers.

Then a mirror reflects the light into an acousto-optical modulator (AOM). When the AOM is not driven, the light passes through without deflection and is blocked by a beam block. When the AOM is driven, the light intensity is split between different orders of diffraction. If the angle of incidence is chosen appropriately and the AOM is driven at the full power, 80% of power goes to the first order of diffraction. The rest goes to the zero-order beam, which is not deflected. The power loss to higher orders of diffraction can be neglected. In order to increase the efficacy of diffraction, the beam's diameter is decreased by a demagnifying telescope before entering the AOM. This set up allows us to switch the optical trap elongated with the glass cell on and off, and to control the trapping depth by applying voltage to the AOM.

The first order beam is then picked up by a D-shaped mirror and is sent to a second AOM. This time, the angle of incidence is chosen so the AOM at full power splits the laser intensity equally between zero and first orders. Then, both beams go through a magnifying telescope, which increases the beams' diameters, to provide a wider trap. The zero order beam goes to the periscope for optical transport system. The second beam is reflected from a D-shaped mirror and then is sent to another periscope. The periscope sends the beam at about 45^0 to the glass cell's north face. This gives us an option to trap the atoms in a crossed-beam trap, which would give a higher density of atoms and evaporative cooling efficacy.

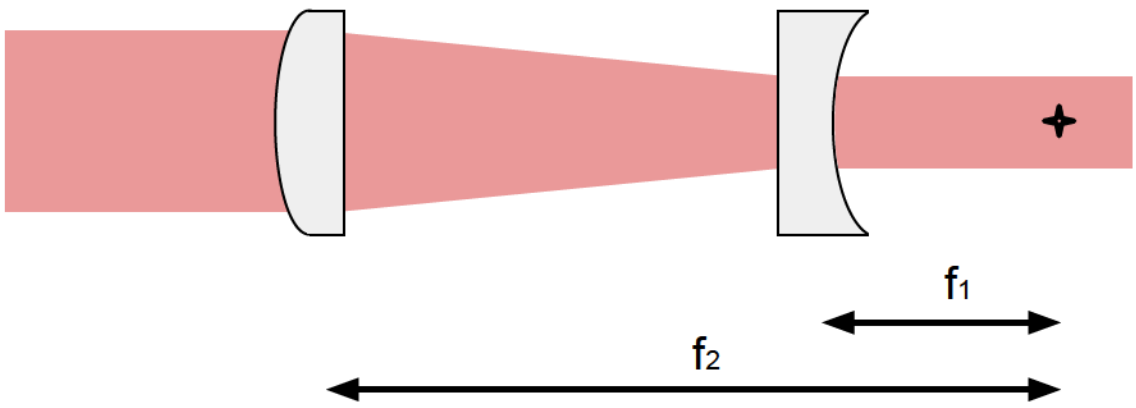

Figure 3.14: Schematics of the telescope. The star represents the focal point.

In this experiment we use a 10 W Ytterbium Fiber Laser **YLR-10-1064-LP 1** from **IPG Photonics**. Both AOMs are **23080-3-1.06-LTD** models actuated by **MLP080-2AS2-A1** driver from **Gooch & Housego**. Both drivers are powered with **BK Precision 1150** power supply. The Faraday optical isolator is **Thorlabs IO-5-1030-HP**. All mirrors and lenses in this setup have a Thorlabs C-coating which makes them more effective for 1064 nm light. Telescopes include a plano-concave and a plano-convex lens. For the demagnifying telescope the rear focal points of the both lenses coincide, which gives the demagnification of f_1/f_2, where f_1 and f_2 are the focal lengths of the concave and convex lenses respectively. For the magnifying telescope the lenses are set in inverse order. To reduce the spherical aberrations, the lenses should be faced with the curved surface to the collimated beam, as shown in Figure 3.14.

Optical transport system

For the optical dipole transport we use a setup introduced by [31], which employs two electrically tunable lenses by Optotune and one static convex lens. The Optotune lenses are made of an optical liquid medium covered with a flexible polymer membrane. The focal length is controlled by running electrical current through a ring that pushes the liquid under the membrane towards the center of the lens, thus changing its curvature.

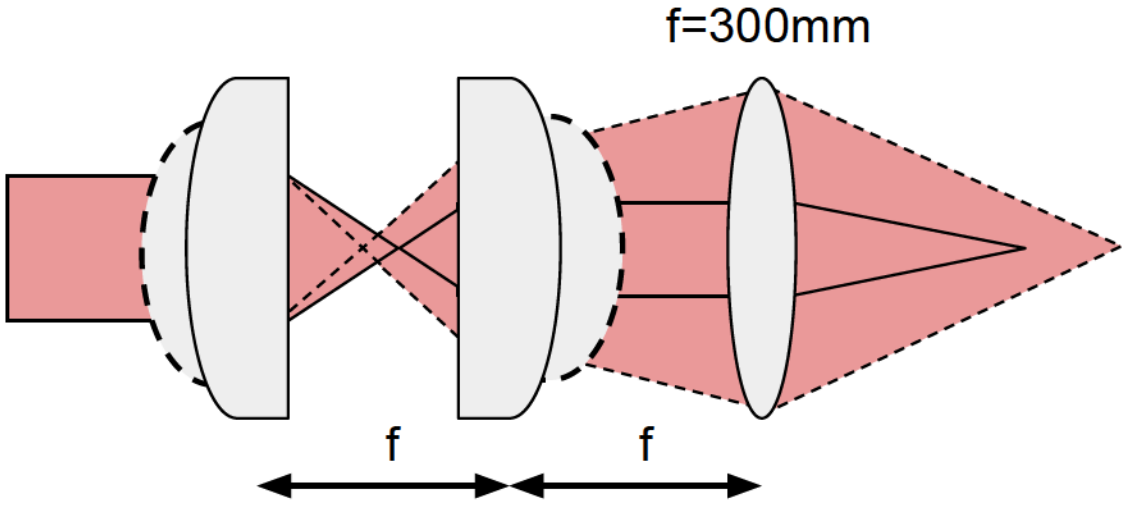

Figure 3.15: Schematics of the set up for optical dipole trapping. First two lenses have tunable focal lengths, the third one has a static positive focal length. Changing both focal lengths provides optical transport. The figure was adapted from [31]

The set up schematics is depicted in Figure 3.15. Using a three-lens setup allows to move the

focal point and to control the waist at the focus at the same time. This results in a constant trapping frequency and trap depth during the transport. We use a static lens with focal length of 300 mm. The tunable lenses are placed before the static one, with the closest being in its focal point. The separation between the two tunable lenses is 300 mm. The lenses are located inside a periscope system which guides the trapping beam from the horizontal plane on the optical table to the input window of the vacuum system as can be seen in Figure 3.13.

In our experiment we use **Optotune EL-10-30-C-NIR-LD** and **EL-10-30-C-NIR-LD** tunable lenses from **Edmund Optics**. The lenses are controlled through special drivers that are connected to the main computer via USB cables. The values of the control electric current are set with a Labview code, integrated with the main control program. This allows to vary the transport parameters as described in section 4.5 and assures the appropriate timing with respect to the other stages of the experimental procedure.

3.6.1 Laser safety measures

It is important to avoid the direct contact of eyes with light from any type of laser. The 1064 nm light is especially dangerous since it does not trigger the blink reflex of a human eye. The appropriate protective goggles are required for every person in the room the a laser of this type is operated. At full power the laser can cause a thermal damage to skin or start a fire, so one has to be sure that all light beams are blocked. It is best to operate the laser at the lowest power during the setup and alignment of the optics.

Chapter 4

Experimental results

In order to achieve efficient optical-dipole trapping and transport of atoms, they should be cooled down to temperatures on the order of a few tens of μK. In our experiment we begin with the laser cooling of ^{87}Rb (Section 4.1) that includes magneto-optical trapping directly from rubidium vapour and the subsequent sub-Doppler cooling in optical molasses. To access ultralow temperatures with RF-induced evaporative cooling (Section 4.4), we put the atoms into the magnetically trappable $|F = 2, m_F = 2\rangle$ state using the optical pumping technique (Section 4.2) and magnetically trap them with a quadrupole field. We start with a low-field magnetic trap (Section 4.3.1) that does not trap atoms with $m_F = 1$, which cause significant losses due to inelastic collisions (Section 4.3.2), and then adiabatically ramp the field gradient compressing the trap (Section 4.3.2). Even though the compression increases the temperature in the trap, the increase in the atomic density leads to a better rate of elastic collisions, which determines the efficiency of the evaporative cooling (Section 4.4.1).

In this chapter we discuss experimental stages in the order in which they occur in our experiment. The completed stages are outlined in Table 4.1, which presents the number of atoms and the temperature after each at the base pressure. Progress toward the RF evaporative cooling is summarized in Section 4.4.2. Basic experimental parameter of optical-dipole trapping and transport are discussed in Section 4.5. Absorption imaging pictures after experimental stages are included in Appendix A.

Stage	Duration	Measured number of atoms	Temperature
MOT	15 s	3.2×10^7	252 μK
Molasses	5.5 ms	3.0×10^7	80 μK
Optical pumping	1 ms	3.5×10^7	83 μK
Magnetic trap	74 ms	3.0×10^7	136 μK
compression	100 ms	2.4×10^7	300 μK

Table 4.1: Experiment outline. Number of atoms and temperature are given at the base pressure.

4.1 Laser cooling

In this section we apply the concept of scattering force to describe the principles of the magneto-optical trapping and optical molasses cooling and then discuss the realization of these techniques in our experiment.

4.1.1 Doppler cooling

One of the easiest ways to cool atomic vapour down is to use a set of counter-propagating laser beams that are red-detuned from one of the hyperfine transitions. Due to the Doppler effect, a moving atom "sees" a shift $\Delta\omega$ in the light frequency proportional to its velocity $\mathbf{v}$: $\Delta\omega = -\mathbf{k} \cdot \mathbf{v}$, where $\mathbf{k}$ is the light's wavevector. As a result, an atom moving between two red-detuned counter-propagating laser beams "sees" a higher frequency from the beam propagating in the direction opposite to the atom's motion and lower frequency from the other beam (see Figure 4.1).

Since the scattering rate depends on the detuning in the atomic reference frame, according to expression (2.34), the scattering force from the oncoming beam is higher than from the codirectional beam. The total force $F_D = F_s(\delta + kv) - F_s(\delta - kv)$ acting on the atom points oppositely to the atom's velocity and is equal to

$$F_D = \frac{-8I\hbar\delta k^2 v}{I_s\Gamma[1 + I/I_s + 4(\delta + kv)^2/\Gamma^2][1 + I/I_s + 4(\delta - kv)^2/\Gamma^2]}, \tag{4.1}$$

where we keep in mind that $\delta < 0$. As can be seen from Figure 4.1, for $|kv| \ll \Gamma$ the magnitude of the force is linearly proportional to the speed:

$$F_D = \frac{-8I\hbar\delta k^2 v}{I_s\Gamma[1 + I/I_s + 4\delta^2/\Gamma^2]^2} = \alpha v, \tag{4.2}$$

which is similar to the viscous force in liquids with effective viscosity α. Because of this analogy the

set-up with counter-propagating laser beams is usually called optical molasses. Using three pairs of beams allows cooling in three dimensions.

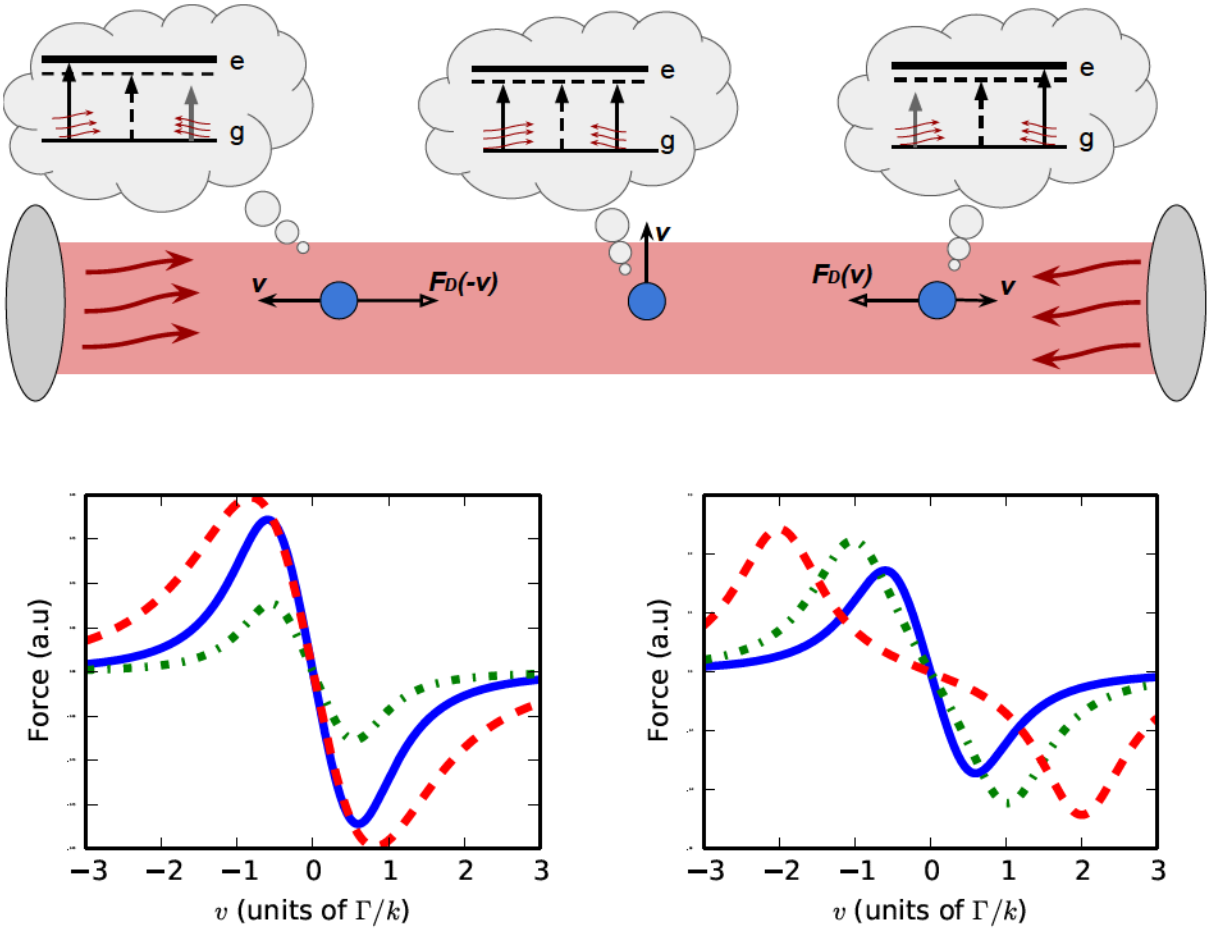

Figure 4.1: **Top**: schematics of the 1-dimensional Doppler cooling. For an atom moving between two laser beams red-detuned from one of the atomic transitions, the counter-propagating beam has a frequency closer to the resonance in atomic reference frame. The net scattering force experienced by an atom from this beam is opposite to the atomic velocity. Dashed arrow represents the transition in the lab frame. **Bottom left**: net scattering force for $\delta = \Gamma/2$ and different values of the resonant saturation parameter $s_0 = I/I_s$: red dashed curve corresponds to $s_0 = 5$, blue solid to $s_0 = 1$ and green dash-dotted to $s_0 = 0.25$. **Bottom right**: net scattering force for $s_0 = 1$ and different values of the detuning: red dashed curve corresponds to $\delta = 2\Gamma$, blue solid to $\delta = \Gamma$ and green dash-dotted to $\delta = 0.5\Gamma$.

Doppler cooling limit

When writing down expression (2.1) for the scattering force, we assume the scattering process is continuous. The discreteness of the photon absorption and emission leads to a heating mechanism

that limits the efficacy of the optical molasses technique [50]. First let us derive the kinetic energy dissipation rate for a viscous force $F = -\alpha v$ with viscosity coefficient α:

$$\frac{d}{dt}\left(\frac{Mv^2}{2}\right) = vM\frac{dv}{dt} = -\alpha v^2, \tag{4.3}$$

where M is the atomic mass. In units of temperature this expression gives us a cooling rate.

Now we need to consider the absorption and emission processes in terms of energy and momentum conservation:

$$\hbar\omega_a = \hbar\omega_0 + E_r, \tag{4.4}$$

$$\hbar\omega_0 = \hbar\omega_e + E_r; \tag{4.5}$$

where ω_a and ω_e are the frequencies of absorbed and emitted photons respectively, ω_0 is the optical transition frequency and $E_r = (\hbar k)^2/(2M)$ is the recoil energy. During one scattering event the atom acquires an energy equal to $\hbar(\omega_a - \omega_e) = 2E_r$. In two beams this happens with the rate of $2\Gamma_s$, thus leading to heating rate of $4E_r\Gamma_s$.

At equilibrium, the cooling rate is equal to the heating rate, which leads to the following condition for the equilibrium temperature:

$$T = \frac{Mv^2}{2k_B} = \frac{2ME_r\Gamma_s}{k_B\alpha}. \tag{4.6}$$

Remembering that $\Gamma_s = \Gamma\rho_{22}$ and using expressions (2.33), (4.2) gives

$$T = -\frac{\hbar\Gamma^2(1 + 4\delta^2/\Gamma^2)}{8k_B\delta}, \tag{4.7}$$

where we assume that $\delta \approx 0$ and $I/I_0 \ll 1$. The equilibrium temperature has a minimum at $\delta = -\Gamma/2$ which determines the Doppler cooling limit as $T_D = \hbar\Gamma/2k_B$. Note that it depends only on the natural linewidth of the cooling transition. For the D_2 transition in ^{87}Rb the Doppler limit is approximately 140μK ($\Gamma = 2\pi \cdot 6.056$ MHz [40]).

4.1.2 Magneto-optical trap (MOT)

Even though the optical molasses technique creates an effective viscous medium which slows down atoms, it does not create a trap and the atoms eventually diffuse out of the molasses region. Adding a magnetic field gradient on top of the 3D optical molasses creates a position-dependent

restoring force that creates a potential well.

The principle of magneto-optical trapping in one dimension is shown in Figure 4.2 and is easily generalized into three dimensions. Two coils with opposite currents (anti-Helmholtz configuration) create a quadrupole magnetic field with zero value at the trap center and constant gradient β extending from the centre. At zero field, the atom is assumed to be a two-level system with energy separation between the ground and excited stated $\hbar\omega$ slightly larger than the energy of the laser light photons. Outside the trap center, where the magnetic field is not zero, the energy levels are further split due to the Zeeman effect depending on m_F number. The energy of the transition between ground and excited states for which $(m_{F'} - m_F) = -1$ is decreased in proportion to the to magnetic field, which leads to an increase in the photon scattering rate and the corresponding force.

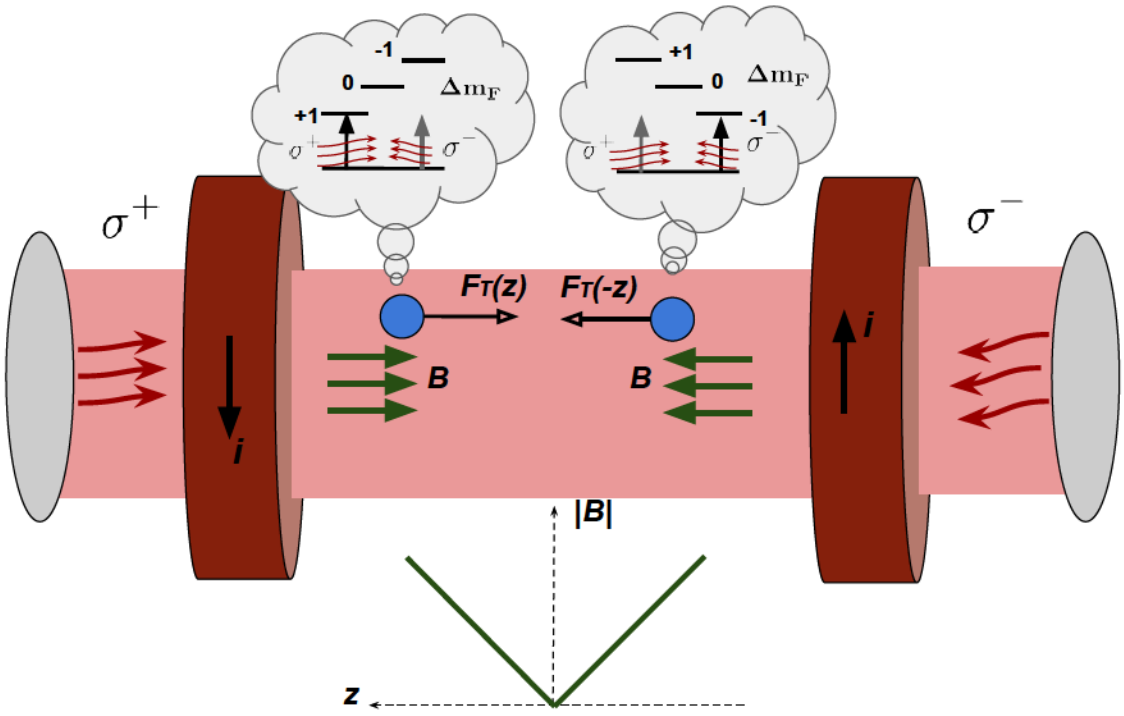

Figure 4.2: Schematics of a 1-dimensional magneto-optical trap. Two coils create a magnetic field with zero in the middle and a constant slope outside. For the atom shifted to the right $m_F = 1$ sublevel is closer to the resonance than $m_F = -1$. Because of a higher scattering rate for σ^+ the net force points toward the center. Here the polarization is defined with respect to the z-axis.

For the levels with $(m_{F'} - m_F) = 1$ the opposite effect occurs, thus reducing the radiation scattering force. Shining two counter-propagating beams leads to trapping of the atoms if the light

in both beams has the same circular polarization with respect to its propagation direction, and the light pointing towards the trap center is σ^- polarized with respect to the magnetic field vector. The other beam has σ^+ polarization and exerts a smaller force compared to σ^- polarized beam. For an atom with zero velocity in z-direction, the resulting force has the same form as expression 4.1 with $g_F\mu_B\beta z/\hbar$ instead of kv. For small displacement, z, the force points towards the trap center with magnitude

$$F_T(z) = F_{\sigma^-}(z) - F_{\sigma^+}(z) = \kappa z, \tag{4.8}$$

where F_{σ^+} and F_{σ^-} are scattering forces from σ^+ polarized and σ^- polarized beams respectively, z is the displacement from the trap center and $\kappa = g_F\mu_B\beta\alpha/\hbar$ is effective elasticity constant, where α is the effective viscosity. This force is harmonic in nature and does not provide cooling of the gas, but since the light is red-detuned from the resonance the Doppler cooling mechanism still takes place. It provides enough dissipation to reduce atomic energy below the trap's depth.

For an atom that is far from the trap center and has a large velocity, the linear approximations 4.2 and 4.8 are no longer valid. When the atom is moving toward the trap, the Doppler effect from the co-propagating beam and the Zeeman effect for the corresponding m_F state contribute to the frequency shift with the same sign and result in a large blue detuning and negligible scattering force. In contrast, the Doppler and Zeeman effect for the counter-propagating beam cancel each other and lead to a scattering force that slows that atom down. As the atom moves toward the MOT, both the Doppler and magnetic shifts decrease keeping the atom near the resonance. This effect is analogous to that of the Zeeman slower [51] and allows to capture faster atoms and dramatically increases the number of atoms in the MOT. Numerical simulations show that the capture velocity is maximized for $\delta = -10\Gamma$ [52] which is in a good agreement with our experimental results.

Experimental realization

Before the MOT was observed, we measured fluorescence at the laser beams' crossing with the CCD camera for different values of the detuning ranging from -400 MHz to 240 MHz (minus sign corresponds to red-detuning) at different currents. In fact, we observed a dip in the signal at -53.12 MHz detuning for 20 A compared to the case of zero current and current of 60 A. This was an indication of the incorrect polarity of the anti-Helmholtz coils with respect to the polarization of the trapping light, which resulted in a potential hill instead of a well. After switching the current direction in both coils, a small peak in fluorescence appeared instead of the dip and a faint cloud

could be observed with an infrared viewer. After that, re-aligning the optics and increasing the current led to a denser cloud near the focus of the imaging system. Then, using the technique of absorption imaging (see section 3.5), the main parameters of the magneto-optical trap were optimized.

In general, at the 3D-MOT stage we aim to collect as many atoms as possible for subsequent cooling. The number of captured atoms is mainly determined by the following parameters: MOT loading time, trapping current, detuning and power of the trapping light, and the repump power. Optimal parameters[1] are summarized in Table 4.2.

Parameter	Trapping current	Trapping light detuning	Trapping light power (per beam)	Total repump power
Value	32 A	-53.12 MHz	10.2 ± 0.9 mW (max)	12 mW (max)

Table 4.2: Setup parameters for the 3D MOT. The optimal parameters very slightly depend on the Rb vapour pressure in the system.

Trapping current

Trapping current defines the tightness of the trap, as discussed in section 4.1.2. In our setup MOT works at trapping current values in the range of $15-50$ A with maximal trapping effectiveness at around 32 A, corresponding to the quadrupole field gradients of 6.3 G/cm in the radial and 13.44 G/cm in the longitudinal directions.

Trapping light's detuning and power

Detuning and power of the trapping light defines the kinetic energy dissipation rate of the atoms in the MOT (see section 4.1.1) and the trap's tightness (see section 4.1.2). Scanning the detuning of the trapping light from -55 MHz to -61 MHz gives a peak number of atoms at around -53.12 MHz, which corresponds to $\delta = -8.8\ \Gamma$. The number of trapped atoms is maximised when the trapping light is set to its maximal power.

Repump light's power

The repump light transfers ^{87}Rb atoms from $|F = 1\rangle$ to $|F = 2\rangle$ ground state, where they are resonant with the trapping light (see section 3.4). In our setup, the trapping efficiency is maximized for the maximal available power of the repump light.

[1]Here and in the other sections in this chapter, optimal values are robust with respect to reasonable changes (e.g on the order of the least significant digits).

MOT loading

Figure 4.3 shows that the MOT loading rate goes down as the number of atoms in the trap increases and the MOT reaches its equilibrium state. It is clear that this steady-state value is higher for a higher rubidium pressure. In the cases when we need to operate at a low background pressure, for example, during experimental stages which involve compressed magnetic trap, we load the MOT for 15 seconds. In other cases, it is more convenient to use a 5-second loading at dispenser current of $3.8 - 4$ A.

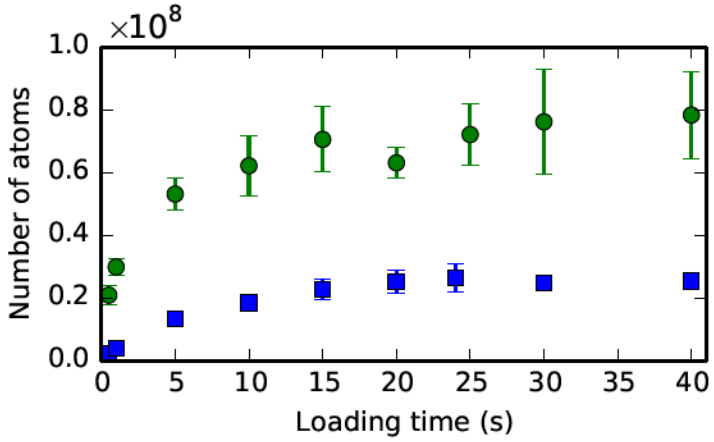

Figure 4.3: MOT loading at different dispenser currents. Green circles correspond to 3.8 A, blue squares correspond to zero current. Error bars represent standard deviation from the mean value.

Number of atoms and temperature

Depending on the current in the dispenser and the loading time, we were able to trap up to 10^8 atoms in the MOT. Because of the Doppler cooling mechanism, the atoms in the MOT are cooled down to around 250 μK, where the temperature was measured using the time-of-flight technique (see section 3.5.5).

4.1.3 Sub-Doppler cooling

So far we only considered atoms in a two-level-system approximation. Including additional levels allows us to describe cooling mechanisms leading to temperatures below the Doppler cooling limit. In the σ^+-σ^- configuration used in this experiment, two counter-propagating laser beams with opposite circular polarizations create a standing wave with linear polarization. The polarization vector direction varies in space along the beams' axis with the periodicity of a wavelength.

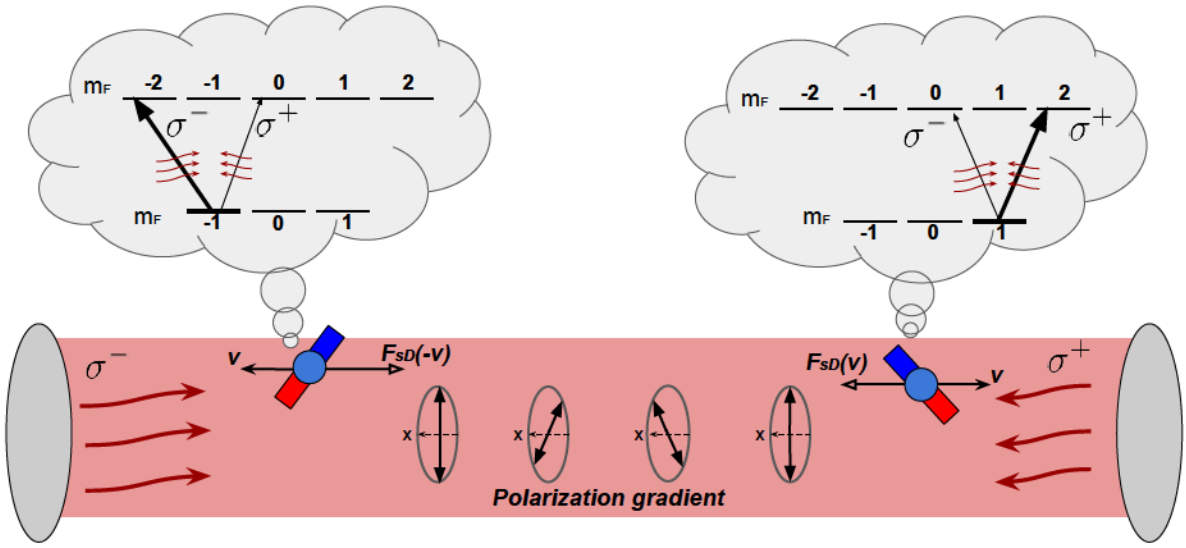

Figure 4.4: Schematics of the 1-dimensional sub-Doppler cooling. Because of the motion-induced orientation, sublevel population of an atom moving to the right is shifted to $m_F = 1$. Since the transition with absorbing σ^+ is stronger than for σ^-, the net scattering force points to the left. Bar magnets represent orientation of the atomic angular momentum $\mathbf{F}$.

The sub-Doppler cooling process is schematically shown by Figure 4.4. An atom at rest scatters both beams equally and on average occupies the $m_F = 0$ substate. An atom that moves along the beams "sees" a polarization vector that rotates with a frequency proportional to the atomic speed. This leads to an increase in the population of the edge m_F sublevels of the atomic ground state, an effect known as motion-induced orientation [53]. In the case of red-detuned light, atoms in the $F = 2$ ground state that are moving towards the σ^+-beam will experience a population shift towards $m_F = 2$, while the atoms moving in opposite direction will be be shifted to $m_F = -2$. For the D2-line in ^{87}Rb, the matrix element of the electric dipole moment for transitions from $m_F = 2$ with absorption of σ^+-photons is $\sqrt{15}$ higher than σ^--photons, which leads to a 15-times higher scattering from the σ^+ beam that opposes the atom's motion, compared to that from the σ^-- polarized light. Analogously, atoms in $m_F = -2$ (moving in opposition to the σ^- beam) state will scatter σ^- with a 15-times higher rate than σ^+-light.

Thus, the net scattering force opposes atomic motion. Since the effectiveness of the motion-induced orientation is proportional to the atomic velocity, the force has the same form as in the Doppler cooling case, but with a higher damping coefficient. The resulting temperature limit is around the photon recoil energy $k_B T_{sD} = (\hbar k)^2/2M$.

Optical molasses

After collecting and cooling a significant number of atoms in the MOT, we turn the quadrupole magnetic field off and keep the atomic cloud in the 3D optical molasses for a few milliseconds. In the absence of magnetic field, both the Doppler and sub-Doppler cooling mechanisms become more efficient and we were able to reduce the temperature down to 80 μK, which is below the Doppler cooling limit.

At first, we were optimizing molasses's parameters trying to reduce the loss of atoms while keeping the final temperature as low as possible. After our first success on magnetic trapping of atoms, we optimized all molasses' parameters in terms of number of atoms in the magnetic trap. The main parameters are discussed below and the optimal values are presented in Table 4.3.

Parameter	Duration	Cooling light detuning	Cooling light power (per beam)	Total repump power
Value	5.5 ms	ramp from (-362.2) MHz to (-53.12) MHz	10.2 ± 0.9 mW	5.7 mW

Table 4.3: Optical molasses parameters.

Duration

The optimal time for optical processes is determined by two competing processes: energy damping and diffusion of the atoms out of the molasses. For the efficient cooling the atoms need to be in molasses for longer than the damping time, which defined by effective viscosity α. On the other hand, optical molasses do not provide any restoring force, so after some time the atoms eventually escape from the molasses region. In our experiment we observe a peak in the number of atoms in the magnetic trap for the molasses cooling time of 5.5 ms.

Cooling and repump light

In optical molasses we the use same laser and optics as for magneto-optical trapping. The power in the six cooling light beams defines the damping rate and temperature limit, while the repump light maintains atoms in cooling transition, as was discussed before. In our experiment we use maximal available power for the cooling light, but reduce the repump power to 5.7 mW.

Frequency sweep

At a constant detuning of the cooling light from the resonance, the cooling force acting on the fastest atoms in the cloud is not linear with velocity and might be significantly reduced. This can be fixed by increasing the detuning of the cooling light as is shown by the right-hand bottom graph in Figure 4.1. In our experiment, we address different velocity classes of atoms by linearly sweeping the detuning form -342.2 MHz to -53.12 MHz during the molasses stage, which seems to decrease the resulting temperature.

Bias fields

In general, it is necessary to eliminate any residual magnetic fields during optical molasses to improve efficiency of the optical molasses. In the presence of a uniform magnetic field, the radiation force from two counter-propagating beams is unbalanced. This can lead to a drift of the cloud from the center and have a negative effect on the magnetic trapping efficiency. In our experiment, using bias coils to cancel out stray magnetic fields does not have a significant positive effect, indicating that the background fields are already close to zero in all directions.

4.2 Optical pumping

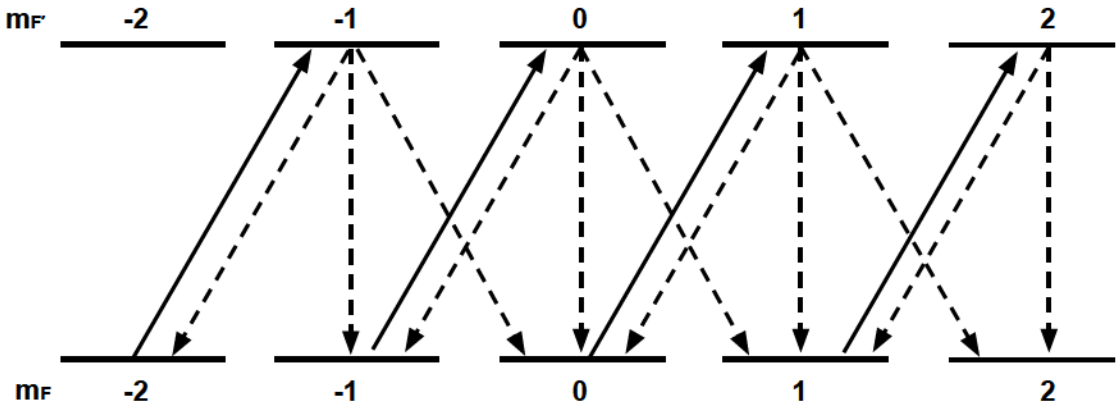

Figure 4.5: Optical pumping with σ^+-polarized light resonant with $F = 2 \rightarrow F' = 2$ transition. Each sublevel is labeled with the corresponding m_F number. Solid arrows correspond to an absorption and dashed to a spontaneous emission of a single photon. The $m_F = 2$ state is a "dark" state.

Shining circularly polarized light at an atomic cloud in a static homogeneous magnetic field magnetically polarizes the cloud so that all atomic magnetic dipoles align along the field axis. This technique is known as the optical pumping and is illustrated by Figure 4.5.

After absorption of a σ^+- polarized photon an atom gains one quantum of angular momentum along the quantization axis thus changing its m_F number by 1. Similarly, m_F is decreased by 1 for σ^-- polarized light. By spontaneously radiating a photon the atom can decay from its excited state into one of the ground states for which $\Delta m_F = 0, \pm 1$. So, after one cycle of absorption and emission of a photon the atomic m_F either stays the same or changes by 1 or 2. After many such cycles the atom is eventually transferred to a "dark" state where it can no longer absorb light due to the angular momentum conservation law.

In our experiment we optically pump ^{87}Rb atom into $|2, 2\rangle$ state (see section 4.2) right after the optical molasses stage before turning on the quadrupole magnetic field. We use a light resonant with the $|F = 2\rangle \rightarrow |F' = 2\rangle$ transition coming from the same optical fiber as the imaging beam. During the optical pumping, we create a quasi-homogeneous magnetic field (see section 3.3.2) along the beam with y-bias field coils. As before, in order to retrieve the atoms that decay into $|F = 1\rangle$ hyperfine state, we use the repumping light.

The parameters for the optical pumping were optimized in terms of the number of atoms in the magnetic trap and are presented in Table 4.4. The turn-on time of the quadrupole field should be long enough to let the atomic magnetic moments realign along the magnetic field vector, but sufficient to prevent the atomic cloud from falling under the influence gravity too far, or spread out due to thermal motion.

Parameter	Duration	Pumping light power (per beam)	Total repump power	Bias field coils current (field)
Value	1 ms	0.25 mW	12 mW (max)	$I_y = 15$ A ($b_y = 9$ G)

Table 4.4: Optical pumping parameters.

4.3 Magnetic trapping

A quadrupole magnetic field in one dimension creates a linear (see section 3.3.1) trap for $|F, m_F\rangle$ states for which $g_F m_F > 0$. If the atoms were sufficiently cooled prior to loading into the magnetic trap, their magnetic moments will adiabatically follow the magnetic field vector as the atoms move across the trap, as was discussed in section 2.3. The Majorana losses (see section 2.3) from the trap

center can be neglected until the temperature is significantly lowered [44]. At this point we expect to transfer the atoms into an optical-dipole trap. Below we discuss the experimental realization of the magnetic trapping in our experiment.

4.3.1 Low-field magnetic trap

In our first successful attempts for magnetic trapping we used 120 A current in the anti-Helmholtz coils, which creates a quadrupole field with gradients of 50.4 G/cm in the longitudinal direction and 23.6 G/cm in the radial direction, and captures a sufficient number of atoms. After the compression of the magnetic trap had been done and optimized, we reduced magnetic currents in the low-field trap stage down to 65 A, which noticeably increased the life-time of the compressed trap. At this current a magnetic field gradient of 27.3 G/cm is not sufficient to hold atoms in $m_F = 1$ state against the gravity, which reduces the number of bad collisions (see section 4.3.2) within the trap. Below we discuss main parameters of the low-field magnetic trap, which are summarized in Table 4.5.

Duration

The duration of the magnetic trap turn-on ramp should be sufficient to allow the atomic cloud to adjust its shape as well as to clear out the atoms with $m_F = 1$. On the other hand, at low currents the trap does not provide a strong confinement in the radial direction, so a significant number of atoms will be lost after a long time. In our experiment we found 74 ms to be the optimal time for the low-field magnetic trap. Programming a value of 300 A for the first 4 ms of magnetic in the control program decreases the turn-on time, for the control circuit to reach the value of 65 A.

Bias fields

In order to eliminate sloshing of the atomic cloud in the magnetic trap, the trap's center should coincide with the cloud's center of mass as the trap is turning on. In the experiment we adjusted the trap's position with bias fields.

Parameter	Duration	Trapping current	Bias coils current (field)
Value	74 ms	65 A	$I_x = 1$ A ($b_x = 0.32$ G) $I_y = 7$ A ($b_y = 4.2$ G) $I_z = 2$ A ($b_z = 1.2$ G)

Table 4.5: Low-field magnetic trap parameters.

4.3.2 Compressed magnetic trap

Compressing the magnetic trap increases the density of atoms and their collisional rate , which is essential for efficient evaporative cooling (see section 4.4.1). In our experiment we run 420 A through the anti-Helmholtz coils, which gives a quadrupole field gradient of 176.4 G/cm in the longitudinal and 82.7 G/cm in the radial directions. During the process of compression, the temperature of the trapped gas increases. At the optimal value of the compression time, we measure a temperature of 240 μK, which is about three times higher than after the molasses cooling stage. This sacrifice is excused by ultra-low temperatures that are promised by evaporative cooling, for which we require the increased density provided by this trap. The main parameters defining the efficiency of the compressed magnetic trap for the purposes of evaporative cooling are discussed below and summarized in table 4.6.

Compression time

On one hand, the process of compression should be gentle enough to allow the atomic magnetic moments to align with the field and to reduce residual center-of-mass motion of the cloud. On the other hand, the compression time should be short enough to prevent the atoms from escaping from the trap at low magnetic fields. A linear ramp from 65 A to 420 A during 100 ms gives an optimal number of atoms after 4 s in the compressed trap.

Bias fields

Since the anti-Helmholtz coils are not perfectly identical and might be slightly misaligned, increasing the trapping current can shift the quadrupole field's zero. This can be avoided by linearly ramping bias field during the compression.

Parameter	Duration	Trapping current	Bias coils current (field)
Value	100 ms	420 A	$I_x = 4.5$ A ($b_x = 1.44$ G) $I_y = 3$ A ($b_y = 1.8$ G) $I_z = 3$ A ($b_z = 1.8$ G)

Table 4.6: Magnetic trap compression parameters.

Magnetic trap lifetime and background pressure

The main sources of atomic losses from the magnetic trap include background collisions and inelastic collisions within the trap [54]. By background collisions, we imply a contact interaction

between the atoms in the trap and free particles such as residual water and hydrogen molecules, ^{85}Rb vapour released from the dispenser and ^{87}Rb atoms which were not trapped in the MOT or were lost during the cooling. In general, after a collision with these particles, the atoms in the trap receive enough energy to escape. Background collisions happen at a constant rate throughout the experiment and do not significantly affect the temperature of the trapped gas since they occur at the same rate for all trapped atoms independent of their energy.

During inelastic collisions between trapped atoms, the atomic internal energy is transferred to their kinetic energy, which is usually allows these atoms to escape from the trap. There are three types of inelastic collisions that cause loss: two-body spin relaxation, two-body dipole relaxation and three-body recombination. In the spin relaxation process, the atomic nuclear spin exchanges angular momentum with the electron spin, changing the atom's hyperfine state. It happens at a high rate until all atoms that can undergo spin relaxation are lost from the trap. However, this process is forbidden for atoms in $|F = 2, m_F = 2\rangle$ state [54], and in our experiment we suppress this loss mechanism by getting rid off $|F = 2, m_F = 1\rangle$-atoms in the low-field magnetic trap. In dipole relaxation collisions, angular momentum is exchanged between the electron spin and its angular momentum. The rate of this process is constant at low temperatures and it determines the lowest temperature limit that can be achieved by evaporative cooling [54]. In three-body recombination, two atoms form a bound molecular state while the third takes away the binding energy as kinetic energy, and all of them leave the trap [55]. This type of collision becomes significant at high densities and in our experiment is negligible. All inelastic collisions occur more frequently near the bottom of the trap, where the density of atoms is maximized, so the coldest atoms preferentially escape from the trap, increasing the sample's temperature.

The characterization of the total losses at the base pressure in our experiment is shown in Figure 4.6. The approximate half-life of the trap is 9 seconds. For ^{87}Rb atoms in $|F = 2, m_F = 2\rangle$, losses due to background collisions dominate, as is illustrated in right-hand graph in Figure 4.6, which shows how the number of atoms kept in the trap changes as we turn on and off dispenser current. Here, dispenser current was set to 3.8 A at minute 1 and was turned off at minute 18. First, the number of atoms drops as the contamination is released from the dispenser. Then, as the pressure goes up, more atoms become available for the trapping and the trap population increases. As the pressure grows further, losses due to background collision become significant and eventually the trap disappears. After turning the dispenser off at this point, the trap population gradually improves as the pressure goes down. In this case, UV-desorbed atoms become the main source

for the trap. Such behaviour suggests that running large currents through the dispenser for a few minutes and then turning it off could be a good strategy for achieving a big number of trapped atoms while maintaining a sufficiently long trap lifetime.

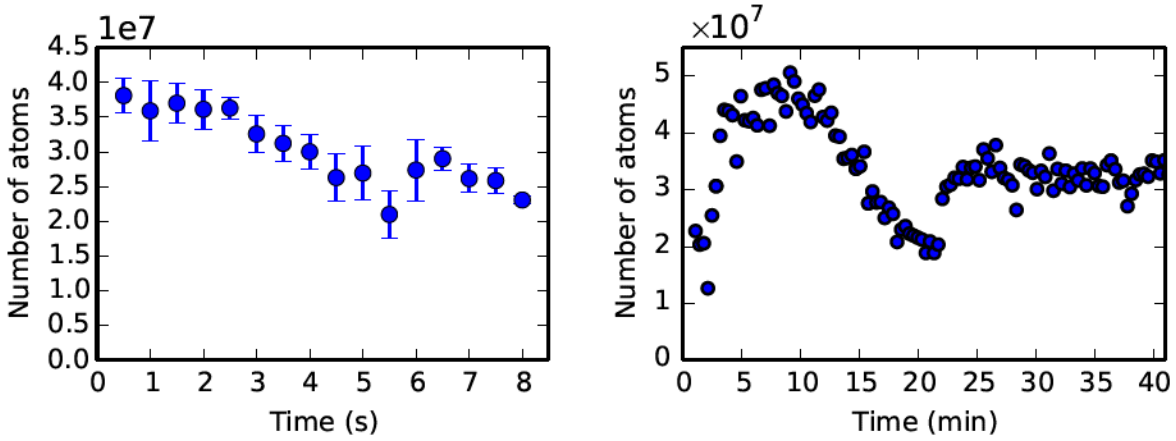

Figure 4.6: **Left**: Number of atoms in the compressed magnetic trap at the base pressure as a function of the trapping time. **Right**: Number of atoms measured after 4 s in the compressed magnetic trap as the background Rb pressure varies. The measurements began at the base pressure and after 1 minute we run 3.8 A current through the dispenser for 17 minutes.

4.4 RF-induced evaporative cooling in a magnetic trap

Temperatures below the sub-Doppler cooling limit can be achieved by means of evaporative cooling. In this technique we selectively remove the fastest atoms from an atomic ensemble trapped in a potential well, thus decreasing the average energy of the ensemble [54]. Below we discuss radio-frequency (RF) field-induced evaporative cooling of atoms in a magnetic trap.

In this technique we selectively remove the most energetic atoms from the magnetic trap by applying an additional linearly-polarized magnetic field that oscillates in time with a radio-frequency. When the RF frequency ω matches the energy separation between two neighboring Zeeman m_F sublevels: $\hbar\omega = g_F \mu_B m_F B$ (see section 2.3), the RF leads to adiabatic transitions between these levels in the same way as is discussed in section 5.1, except that here, more than two levels are involved. Changing the m_F-number leads to a reduction of the trap's depth and loss of atoms. Since the separation between sublevels depends on the strength of the magnetic field, it is larger in the regions further from the trap center, where only the most energetic atoms can pass. Thus, using high RF field frequencies allows to clear the trap of these "hot" atoms without perturbing the rest as is schematically shown in Figure 4.7.

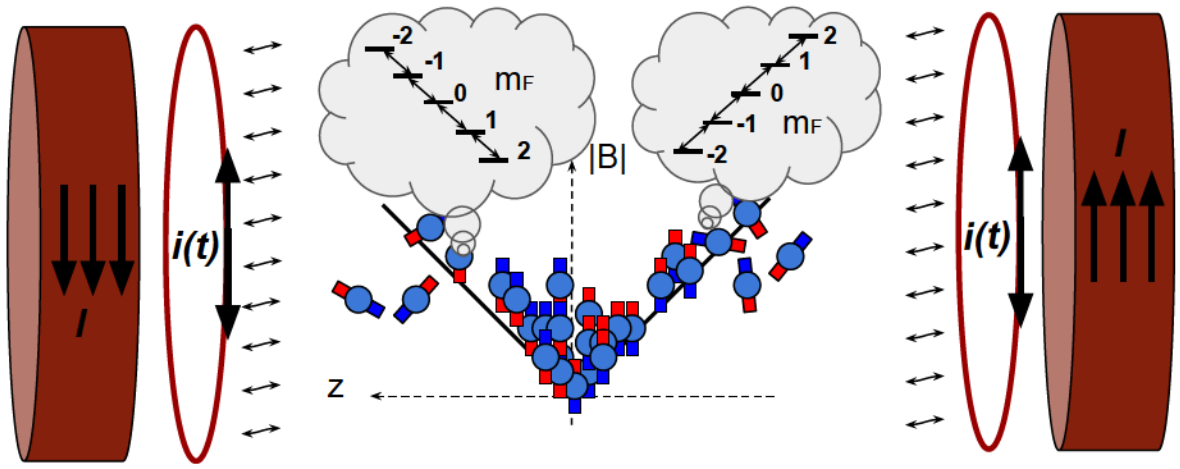

Figure 4.7: RF-induced evaporation schematics. Atoms are magnetically trapped in a quadrupole field created by coils with large current I. Oscillating magnetic field created by a pair of Helmhotz coils with alternating current $i(t)$ is resonant only with the most energetic atoms. Going through the resonant slice, atoms can go to a state with $m_F \leqslant 0$, where they are no longer trappable.

4.4.1 Evaporative cooling efficiency

Qualitatively the process of evaporative cooling can be considered as many cycles of two-step processes. The first step is the truncation, during which the hottest atoms are removed from the distribution tail. The following step is the rethermalization or the relaxation of the resulting non-thermal distribution to a new equilibrium distribution corresponding to a lower temperature. The rethermalization process is performed by elastic collision between atoms within the ensemble, and it was shown experimentally and theoretically [54] that efficient rethermalization is achieved after 2.7 elastic collisions.

It seems that in general, one would want to increase the time between the truncation steps in order to allow the atoms to rethermalize. However, the inevitable losses limit the life-time in the trap and put under question the reasonableness of the evaporative cooling if too many atoms are lost during the process. A better approach is to decrease the elastic collision time, or equivalently, to keep the elastic collision rate higher than the loss rate.

The elastic collision rate can be estimated as[1]

$$R_{col} = n\sigma\overline{v}, \tag{4.9}$$

[1]The derivation of the average elastic collision rate follows one of the lectures given on the group meetings by Dr. LeBlanc

where n is the atomic density, σ is the elastic collision cross-section and $\overline{v} = \sqrt{2} \times (8k_BT/\pi M)^{1/2}$ is the average relative velocity between two atoms. In order to derive the average collision rate we assume the Boltzmann density distribution in the trap $n(\mathbf{r}) = n_0 \exp[-(g_F m_F \mu_B \beta r')/k_B T]$, where β is the magnetic field gradient in the radial direction and $r' = \sqrt{x^2 + y^2 + 2z^2}$. The peak density n_0 can be found from the normalization $N = \int n(\mathbf{r}) d\mathbf{r}$:

$$n_0 = \frac{N}{4\pi} \left(\frac{g_F m_F \mu_B \beta}{k_B T} \right)^3, \tag{4.10}$$

where N is the total number of atoms in the trap. The average atomic density in the trap is found as

$$\langle n \rangle = \frac{1}{N} \int n^2(\mathbf{r}) d\mathbf{r} = \frac{n_0}{8}. \tag{4.11}$$

Substituting expressions 4.11 and 4.10 to 4.9 gives the following expression for the average collision rate as a function of the temperature, field gradient and number of atoms:

$$\langle R_{col} \rangle = A \frac{N \beta^3}{T^{5/2}}, \tag{4.12}$$

where A is a constant defined by atomic properties and we assume that at low temperatures σ is constant. Expression 4.12 suggests that a tighter trap would give a higher elastic collision rate, however one needs to take into account the fact that during adiabatic compression the field performs work on the trapped gas increasing its temperature. The temperature change can be estimated using the conservation of average phase space density in an adiabatic process (also is known as Liouville's theorem, e.g. see [56]). The average phase space density is given by [54]

$$D = \langle n \rangle \lambda_{dB}^3 \sim \frac{\beta^3}{T^{9/2}}, \tag{4.13}$$

where $\lambda_{dB} = \sqrt{2\pi\hbar^2/M k_B T}$ is the thermal de Brogile wavelength. For a constant D, expression 4.13 gives a change in temperature by a factor of $b^{2/3}$ if the field gradient was changed by a factor of b. As a result, the average elastic collision rate is changed by a factor of $b^{4/3}$ if we neglect the particle loss during the compression. It means that for reasonable densities, a compression of the magnetic trap is beneficial for the elastic collision rate.

To summarize, for successful evaporative cooling it is essential to achieve experimental conditions including magnetic field gradient, magnetic trap lifetime and atomic temperature in the trap

that allows the atoms to rethermalize during the evaporation process. In order to make the evaporation cooling efficient, it is necessary to optimize parameters of the truncation-relaxation steps (such as the duration, the RF sweep boundaries and the oscillating field power) so that the change in the number of atoms and the temperature leads to an increase in the elastic collision rate after each step.

4.4.2 RF-induced evaporation results (in progress)

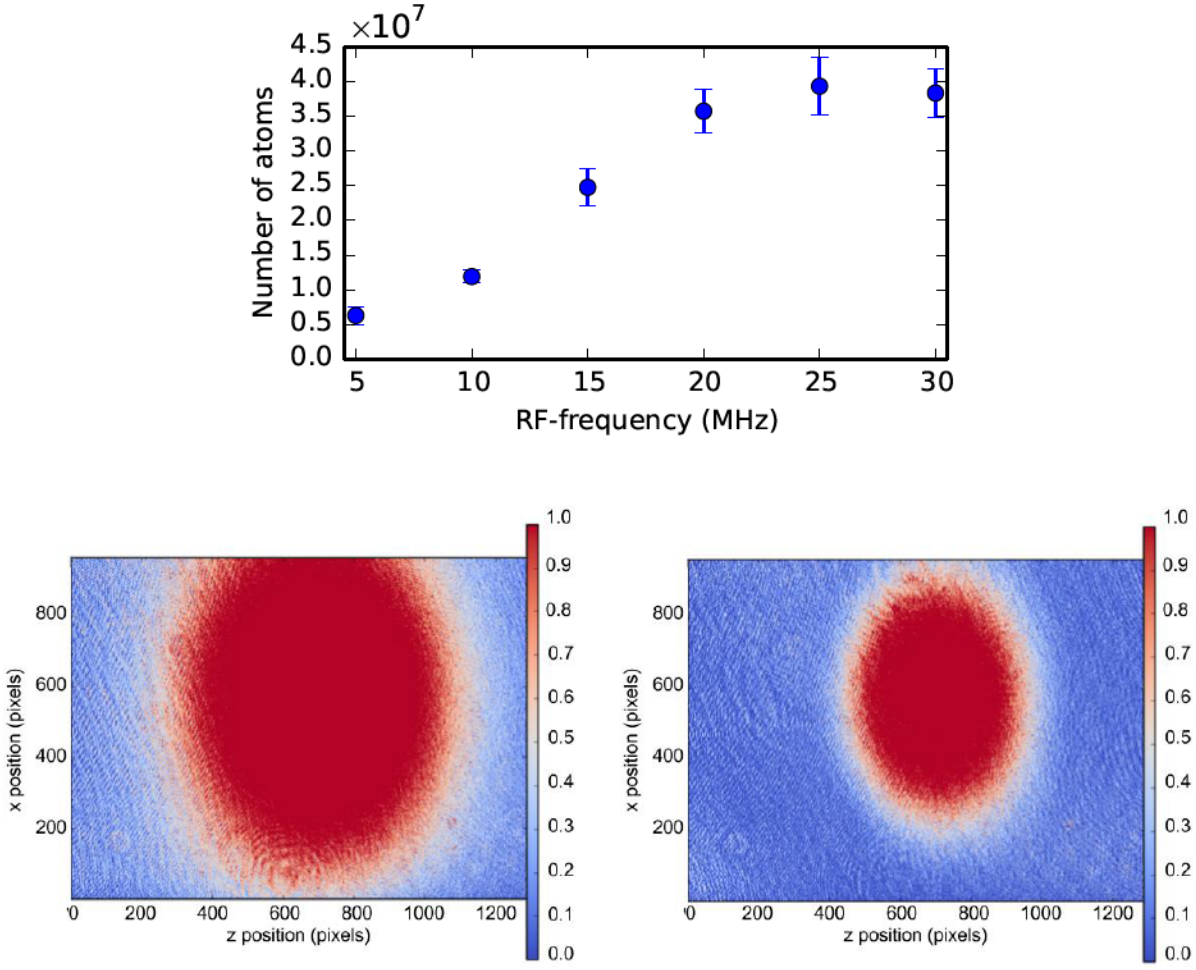

Figure 4.8: **Top**: Number of atoms after 4 s in the compressed magnetic trap with applied RF magnetic field. The field is created by applying an alternating voltage with peak-to-peak amplitude of 510 mV to the RF-coils (see section 3.3.5). **Bottom**: Absorption image of the atomic cloud after 4 s in the compressed magnetic field with (right) and without RF field (left). In the case where there in no RF field, we measure 4.2×10^7 atoms at 280 μK. RF is created by an oscillating voltage in the RF coil with peak-to-peak amplitude of 510 mV, whose frequency linearly changes from 25 MHz to 10 MHz. In this case we measured 1.7×10^7 atoms at 140 μK after evaporation. The colorbar represents optical density $n\sigma_s l$.

In this section we discuss current progress on RF evaporative cooling. Figure 4.8 (top) shows the loss of population of the compressed magnetic trap as we decrease the frequency of the applied RF field. It can be seen that the induced evaporation starts at frequencies below 25 MHz.

The maximal populations achieved in the compressed magnetic trap in our experiment are around 6×10^7 atoms, which give the calculated average collision rate of $1.6 - 2.4$ collision/s. Applying a linear RF sweep from 25 MHz to 10 MHz for 4 s provides a noticeable reduction in temperature as is shown in Figure 4.8 (bottom). To achieve high efficiency of the evaporative cooling, one needs to maximize the elastic collision rate after each step as was discussed in section 4.4.1.

4.5 Optical transport (in progress)

One of the main elements defining the versatility of our experiment is the optical-dipole transport, whose setup is discussed in section 3.6. Below we discuss the main characteristics of optical-dipole traps and general issues concerning optimization of the optical transport.

4.5.1 Focused beam optical dipole trap (follows [55])

The origin of the optical-dipole force and trapping potential was considered in section 2.4. It was shown that the trapping potential is proportional to the light intensity I. The intensity of a Gaussian light beam with power P propagating in z-direction is given by

$$I(r,z) = \frac{2P}{\pi w^2(z)} \exp\left(-2\frac{\rho^2}{w^2(z)}\right), \tag{4.14}$$

where ρ is the distance from the beam's axis of symmetry and $w(z)$ is the beam waist given by

$$w(z) = w_0\sqrt{1+\left(\frac{z}{z_R}\right)^2}, \tag{4.15}$$

where w_0 is the waist at the focus, $z_R = \pi w_0^2/\lambda$ and λ is the wavelength of the light. Thus, the optical-dipole potential has a Gaussian shape in the radial direction:

$$U(\rho,z) = U_0 \exp\left(-\frac{2\rho^2}{w^2(z)}\right). \tag{4.16}$$

Near the bottom, the trap has a quadratic shape:

$$U(\rho, z) = U_0 - \frac{1}{2}M\omega_\rho^2\rho^2 - \frac{1}{2}M\omega_z^2 z^2, \tag{4.17}$$

where $\omega_\rho = \sqrt{4U_0/MW_0^2}$, and $\omega_z = \sqrt{2U_0/Mz_R}$.

Preliminarily studies of the optical-dipole transport setup in our experiment performed MengXing Na showed [57] that we should be able to move the focus of the beam over a 25 cm distance at a constant waist $w_0 = 135$ μm, which corresponds to a trap depth of 30 μK.

4.5.2 Optimal optical transport

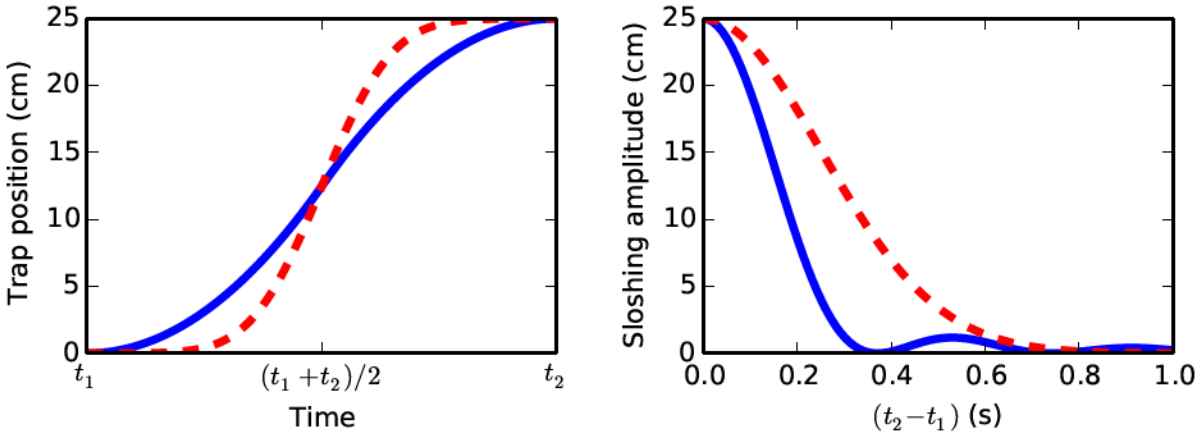

Figure 4.9: Characterization of residual sloshing in a non-adiabatic transport over 25 cm. **Left**: Trap position as a function of time for quadratic (blue solid) and erf-like (red dashed) profiles for a transport between moments of time t_1 and t_2. **Right**: Amplitude of the residual centre-of-mass oscillations for the quadratic (blue solid) and erf-like (red dashed) transport profiles for transport duration $t_2 - t_1$.

The loss in the number of atoms during and after the optical transport is mainly determined by the finite trap's lifetime and the residual center-of-mass oscillations caused by the motion of the trap. In addition to the losses discussed in section 4.3.2, the optical dipole trap has a relatively low depth which allows free evaporation during which the most energetic atoms overcome the potential barrier and escape.

To optimize the number of atoms left in the trap, the transport should be fast enough to reduce the losses associated with the collisions and free evaporation, but the trap should be moving in such a way that the residual sloshing is suppressed, so it does not spill out too many atoms and does not convert to heat. In [58] it was shown that the residual sloshing amplitude S in a harmonic

trap depends on the Fourier component of the trap's velocity profile $v_T(t)$ during the transport, calculated at the trapping frequency ω_T:

$$S = |\int_{-\infty}^{+\infty} v_T(t) e^{-i\omega_T t} dt|. \tag{4.18}$$

Figure 4.9 shows the sloshing amplitude as a function of the transport time for a simple quadratic and a more complicated error-function profile. In both cases, oscillations are strongly damped after a reasonable transport time of 0.8 s. In our experiment, the control of the laser focus position profile is realized in Labview with small discrete steps.

In the experimental sequence used for the planed on-chip experiments, we aim at to achieve temperatures of the gas around 10 μK for loading into the optical dipole trap and transport. If needed, it is better to create a Bose-Einstein condensate near the chip than in the preparation chamber, since its enhanced density would lead to a higher rate of losses associated with three-body collisions during the transport [30], and even a small amount of heating would cause the transition of the cloud back to a thermal state.

Chapter 5

Magnetic-field-mediated coupling and control in atomic-nanomechanical systems

By taking the best aspects from quantum systems of a different nature, hybrid quantum systems perform in ways the individual systems can not and offer many applications for quantum technology [2, 3]. As an example, the long coherence times of trapped ultracold atoms can be combined with conventional read-out techniques available for solid-state devices. In this chapter we discuss a few ways to control the mechanical state of a nanostring using magnetic interactions with an ultracold gas, as was proposed in [1]. We start the discussion with Landau-Zener theory of adiabatic transitions in two-level systems with avoided level crossings (section 5.1). After that, we present a proposal for an on-chip design (section 5.2) for a nanostring that allows two different sources for magnetic coupling to atomic states, and several applications (section 5.4). This chapter is an adapted version of recently published work [1].

5.1 Adiabatic transitions at an avoided level crossing

Evolution of a two-level system with off-diagonal perturbation $|V\rangle$ in the Hamiltonian with a time-independent diagonal elements $\hbar\omega_1$ and $\hbar\omega_2$ was already discussed in 2.1.1. Here we generalize our discussion[1] for the case when the levels $\omega_1(q)$ and $\omega_2(q)$ depend on parameter q and cross at

[1] Discussion in this section mostly follows [32].

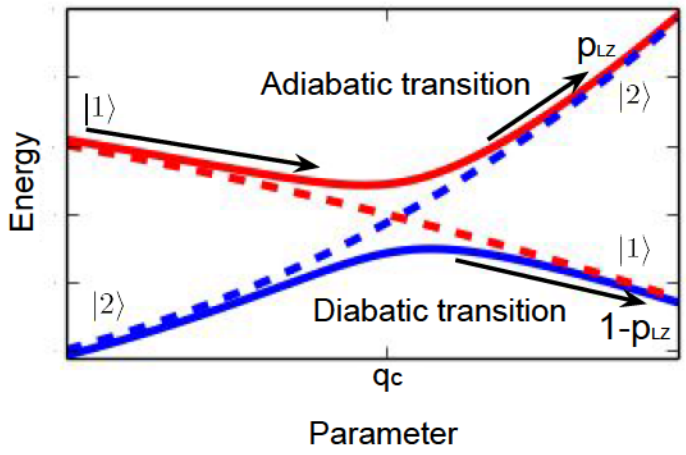

Figure 5.1: Energy of the two levels as a function of the parameter p with (solid) and without the coupling (dashed). Red curves correspond to $\hbar\omega_1$ and E_+. Black arrows indicate adiabatic and diabatic transition in a system starting on red curve.

some parameter value q_c : $\omega_1(q_c) = \omega_2(q_c) = \omega_c$, when the coupling is turned off (as is shown in dashed in Figure 5.1). In particular, we are interested in how the coupling affects the evolution of the system when the parameter q sweeps through the crossing value q_c.

To analyse this, let us consider the following Hamiltonian:

$$\hat{H}(\theta) = \hat{H}_0(q) + \hat{V} = \hbar \begin{pmatrix} \omega_1(q) & \frac{1}{2}\Omega e^{-i\phi t} \\ \frac{1}{2}\Omega e^{i\phi t} & \omega_2(q) \end{pmatrix}, \tag{5.1}$$

with off-diagonal coupling term $\hat{V}_{12} = \frac{1}{2}\Omega e^{-i\phi t}$, where Ω is real. The eigenvalues of this Hamiltonian are

$$E_\pm(p) = \frac{1}{2}\left([\omega_1(q) + \omega_2(q)] \pm \sqrt{[\omega_1(q) - \omega_2(q)]^2 + \Omega^2} \right). \tag{5.2}$$

With the coupling, the level crossing is avoided since $E_+(q) > E_-(q)$ for any q. At the critical point q_c the levels are separated by $E_+(q_c) - E_-(q_c) = \hbar\Omega$.

When the parameter changes in time, the evolution of the two-level system in the basis of the uncoupled eigenstates $|1\rangle$ and $|2\rangle$ can be obtained by modifying equation 2.6:

$$|\psi(t)\rangle = c_1(t) \exp\left[-i \int_0^t \omega_1\left(q(t')\right) dt' \right] |1\rangle + c_2(t) \exp\left[-i \int_0^t \omega_2\left(q(t')\right) dt' \right] |2\rangle . \tag{5.3}$$

If the parameter q sweeps through the level crossing, the system starting at a higher energy state $|1\rangle$ (the red curve in Figure 5.1) will stay at the higher energy state (adiabatic transition) with

probability $p_{LZ} = |\langle 2\,|\psi(t)\rangle\,|^2$. In case of an infinitely long linear sweep, this probability is given by the Landau-Zener formula [59]

$$p_{LZ} = 1 - \exp\left(-\frac{\pi}{2}\frac{\Omega^2}{\Delta\omega_{12}/\Delta t}\right), \tag{5.4}$$

where $\omega_{12}(q(t)) = \omega_1(q(t)) - \omega_2(q(t))$. According to expression 5.4, p_{LZ} goes to zero in the limit of the large sweep rate $\Delta\omega_{12}/\Delta t \gg \Omega^2$ or when the coupling is zero, which corresponds to a diabatic transition between two levels. In contrast, in the case of strong coupling (large separation between the levels) and low sweep rate, the system will more likely undergo an adiabatic transition. The wavefunction that describes the system after the sweep, can be written as

$$|\psi\rangle = \sqrt{1 - p_{LZ}}\,|1\rangle + \sqrt{p_{LZ}}\,|2\rangle\, e^{i\phi_{LZ}}, \tag{5.5}$$

where $\phi_{LZ} = \int \omega_{12}(q(t))dt$ is the relative phase between the two states.

By varying the parameter sweep's conditions, it is possible to engineer a wavefunction for particular experimental applications. For example, setting the conditions to achieve adiabatic transitions with $p_{LZ} \approx 1$ provides a robustness for the state transfer, which is beneficial for the mechanical cooling (section 5.4.1) and thermometry (5.4.2) experiments. On the other hand, setting $p_{LZ} = 1/2$ leads to an equal superposition state, which offers a way for creating a quantum entanglement between mesoscopic mechanical devices, as is discussed in section 5.4.3.

5.2 Chip design

In this section we discuss a practical design to create a coupling between Zeeman sublevels of the ground state of alkali metal atoms (in particular ^{87}Rb) and mechanical motion of a magnetized nanonostring via an oscillating magnetic field, generated by this motion. In this setup, the long lifetime of the Zeeman states offers a coherent manipulation of the nanostring motion provided by interaction between atomic magnetic dipole moments and the magnetic moment of the nanostring.

Using on-chip design allows near-surface trapping of cold atoms using a magnetic trap [26] (see Figure 5.2), as well as an optical-dipole trap created in a beam focused near the chip [60] or using chip-integrated optics [61, 62] as the nanomechanical part of the hybrid system. For our experiment we are considering using high-tensile stress SiN nanostrings [22–25]. Compared to cantilever designs previously used for atom coupling [19–21], this geometry permits a magnetic

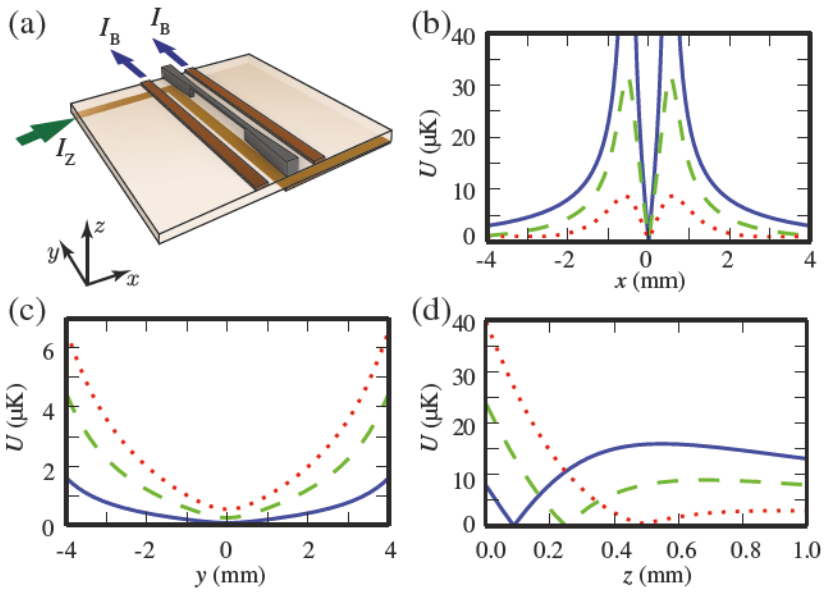

Figure 5.2: (a) Schematic design of the proposed on-chip nanostring. Magnetic field from a Z-shaped wire with current I_Z, combined with a bias field from two parallel wires with equal currents I_B created a magnetic trap similar to Ioffe-Pritchard configuration [27]. (b,c,d) Numerical calculation of the magnetic trapping potential for $|F = 1, m_F = -1\rangle$ state of ^{87}Rb in three direction. The trap's position and depth can be adjusted by varying current through Z-wire at constant $I_B = -5$ A: red dotted curves correspond to $I_Z = 10$ A, green dashed to $I_Z = 6$ A, blue solid to $I_Z = 2$ A. The bias wires are separated by 1 mm. Same or analogous pair of bias wires with lesser separation can be used for cancelling magnetic field offsets as is discussed in section 5.3.3.

coupling with controllable strength by running electric current through the string. In addition, this type of nanomechanial devices shows good quality factors in the frequency range where the string's fundamental mode ω_{m} can be matched to atomic resonance ω_{a} by tuning the Zeeman splitting. For example, a 200 μm long-string, with width of 2.75 μm and thickness of 350 μm has effective mass $m_{\mathrm{eff}} = 8.4 \times 10^{-13}$ kg and it has a room-temperature Q factor of 1.6×10^5 for the fundamental mode $\omega_{\mathrm{m}}/2\pi = 850$ kHz [24]. Having a good quality factor leads to a low decoherence rate of the mechanical oscillator, which is essential for all of the applications proposed in this chapter. Estimating the decoherence rate as $\gamma_{\mathrm{dec}} = k_{\mathrm{B}}T_{\mathrm{s}}/\hbar Q$ (where T_{s} is the temperature of the substrate) [63] gives $\gamma_{\mathrm{dec}}/2\pi = 39$ MHz for the room temperatures, $\gamma_{\mathrm{dec,4K}}/2\pi = 520$ kHz at 4 K and $\gamma_{\mathrm{dec,10mK}}/2\pi = 1.3$ kHz at 10 mK, which is comparable with a system using a carbon nanotube coupled to atoms [64].

5.3 Magnetic coupling

In the systems we consider in this chapter, the interactions between the atoms and the mechanical resonator are mediated through magnetic fields [21, 65, 66]. Even though we are mostly interested in the effect of the coupling on the state of the nanostring, it is easier to estimate the coupling strength by treating the oscillating magnetic field from the nanostring as a perturbation to Zeeman level structure $|F, m_F\rangle$ in a static background magnetic field $\mathbf{B}$, which is described by the Hamiltonian $\hat{H}_Z = g_F \mu_B (\hat{\mathbf{F}} \cdot \mathbf{B})/\hbar$ (see section 2.3). A generalized quantum description of the whole system will be introduced in section 5.3.4. If we assume that the static field points along the z-direction, and oscillating magnetic field $\mathbf{B}_\mathrm{m}(\mathbf{r}, t) = \mathbf{B}_{\mathrm{m},0}(\mathbf{r}) \cos \omega_\mathrm{m} t$ with amplitude $\mathbf{B}_{\mathrm{m},0} = B_{\mathrm{m},0}\{\sin\theta, 0, \cos\theta\}$, resonant with levels $|F, m_F\rangle$ and $|F', m'_F\rangle$, will couple these levels with coupling strength

$$\hbar\Omega = \frac{g_F \mu_B B_{\mathrm{m},0}}{\hbar} \langle F' m'_F | \hat{F}_x \sin\theta + \hat{F}_z \cos\theta | F m_F \rangle . \tag{5.6}$$

The second term here represents the transition between two different hyperfine states with $F' \neq F$ and $m_F = m'_F$. Frequencies of such transitions are much higher than those that are available in our design, so they can be neglected here. The first term is responsible for spin-flipping transitions $m'_F = m_F \pm 1$ within the same hyperfine level. In this case the coupling has only off-diagonal elements, that can be estimated using the same approach as in section 2.1.1. In the rotating-wave approximation, the coupling strength is

$$\frac{\hbar\Omega}{2} = \frac{g_F \mu_\mathrm{B} B_{\mathrm{m},0} \sin\theta}{4} \sqrt{F(F+1) - m_F(m_F \pm 1)}, \tag{5.7}$$

where Ω is the frequency of the Rabi oscillations between two Zeeman sublevels in the resonant case.

5.3.1 Magnetic field from an oscillating point dipole

One method of generating an oscillating magnetic field is by depositing a permanent magnet on the nanostring [67]. A point-like magnetic dipole with moment $\boldsymbol{\mu}_m$ oriented along x-direction placed at the center of a nanostring oscillating in z-direction with an amplitude α (as is shown in

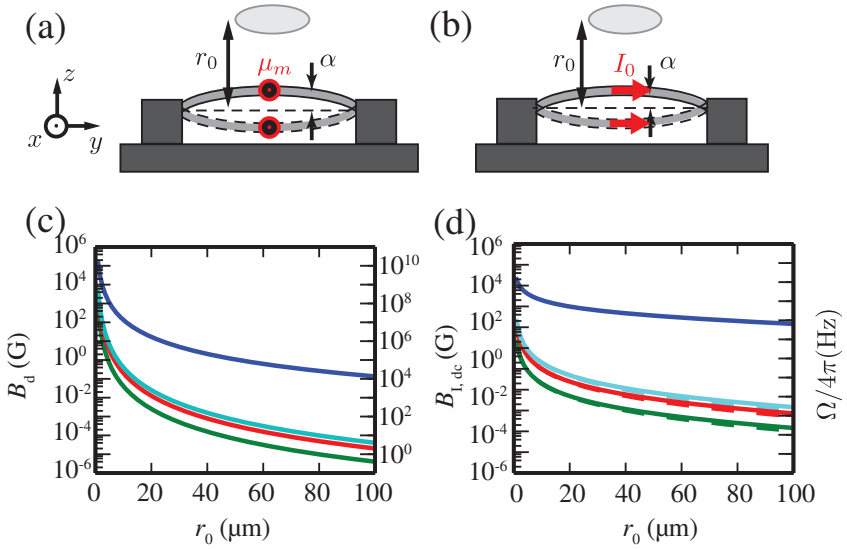

Figure 5.3: **Top**: schematics of the nanostring with a permanent magnet(a) and electric current(b). **Bottom**: Magnetic field (left axis) and coupling parameter for $|F = 1\rangle$ state of ^{87}Rb from a permanent magnet with $\mu_m = 0.067$ nJ/T (c) and 1 A of electric current (d). Blue solid curve represents the static part of the coupling field B_{0x} ($B_{0x,\mathrm{d}}$ or $B_{0x,I}$). The other curves correspond to the oscillatory part $B_{\mathrm{m},0}$ ($b_d\alpha$ or $b_I\alpha$) for the nanostring's amplitudes $\alpha = 10$ nm (upper light blue), $\alpha = 5$ nm (middle red) and $\alpha = 1$ nm (lower green).

Figure 5.3(a)) and frequency ω_{m} creates a magnetic field [66]

$$B_{\mathrm{d}}(t) = \frac{\mu_0\mu_m}{4\pi r_0^4}[r_0 - 3\alpha\cos(\omega_{\mathrm{m}}t)] \equiv B_{0x,\mathrm{d}} + b_{\mathrm{d}}\alpha\cos(\omega_{\mathrm{m}}t), \tag{5.8}$$

where r_0 is the distance from the magnet's equilibrium position, $B_{0x,\mathrm{d}}$ and $b_{\mathrm{d}}\alpha$ are the static and the oscillatory components of the magnetic field respectively. The influence of the static component on the coupling strength is discussed in section 5.3.3. The calculations for components are given in Figure 5.3(c).

5.3.2 Magnetic field from current-carrying wire

A nanostring design also offers the possibility to create oscillating fields by passing an electric current through a conducting layer deposited on the string. In the case of a direct current I_0 running along the y-direction, the nanostring oscillating along the z-direction with amplitude α creates magnetic field

$$B_{\mathrm{I,dc}}(t) = \frac{\mu_0 I_0}{2\pi r_0^2}[r_0 - \alpha\cos(\omega_{\mathrm{m}}t)] \equiv B_{0x,I} + b_{\mathrm{I}}\alpha\cos(\omega_{\mathrm{m}}t), \tag{5.9}$$

where $B_{0x,I}$ and $b_{\mathrm{I}}\alpha$ are the static and oscillatory parts of the magnetic field. This analytical expression is derived from an approximation of a straight infinitely long wire oscillating in z. A numerical simulation that calculates the total magnetic field from many small linear elements forming the string shows similar results (see Figure 5.3(d)).

Similarly, a magnetic field created by an alternating current $I_{\mathrm{ac}} = I_0 \sin(\omega_{\mathrm{ac}} t)$ is given by

$$B_{\mathrm{I,ac}}(t) = \frac{\mu_0 I_0}{2\pi r_0^2}[r_0 \sin\omega_{\mathrm{ac}} t + \frac{\alpha}{2}\sin(\omega_{\mathrm{ac}} + \omega_{\mathrm{m}})t + \frac{\alpha}{2}\sin(\omega_{\mathrm{ac}} - \omega_{\mathrm{m}})t]. \tag{5.10}$$

In this case, adjusting the frequency of the current drives transitions with frequencies that are different from ω_m.

Using electrical current as a source for magnetic coupling makes it possible to change the coupling strength during the experiment, but it heats the nanostring, thus increasing the decoherence rate of the string. Using an alternating current also affects the mechanical motion of a string with a bilayer design [24], which should be avoided in the mechanical cooling and thermometry experiments.

5.3.3 Compensating field

According to expressions 5.8 and 5.9, nanostrings with a permanent magnet and a constant current both create a constant magnetic field B_{0x} ($B_{0x,\mathrm{d}}$ or $B_{0x,I}$), which is perpendicular to the background static field B_{0z}, and is greater than the oscillatory part $B_{\mathrm{m},0}$ ($b_{\mathrm{d}}\alpha$ or $b_{\mathrm{I}}\alpha$) by approximately two orders of magnitude. It shifts the vector of the total static magnetic field ($\mathbf{B}_{0z} + \mathbf{B}_{0,x}$) towards $\mathbf{B}_{\mathrm{m},0}$ as is shown in Figure 5.4 (left), thus decreasing the angle θ between $B_{\mathrm{m},0}$ and the total static magnetic field. According to equations 5.8 and 5.9, the ratio of the oscillatory to static component of the coupling field $\chi = B_{\mathrm{m},0}/B_{0x}$ is equal to $r_0/3\alpha$ for the permanent magnet and r_0/α for the direct current. In terms of $B_{m,0}$, the spin-flipping part of the magnetic field can be written as

$$B_{\mathrm{m},\perp} = B_{\mathrm{m},0}\sin\theta = \frac{B_{\mathrm{m},0}B_{0z}}{\sqrt{B_{0z}^2 + \chi^2 B_{\mathrm{m},0}^2}}. \tag{5.11}$$

In the limit of infinite $B_{\mathrm{m},0}$, the coupling part becomes $B_{\mathrm{m},\perp} \approx B_{0z}/\chi$, which implies that increasing the direct current running through the nanostring or choosing a permanent magnet with higher magnetization has a limited effect on the coupling strength (see inset of Figure 5.4). This limit can be improved by cancelling the constant part of the nanonstring's field with a set of permanent

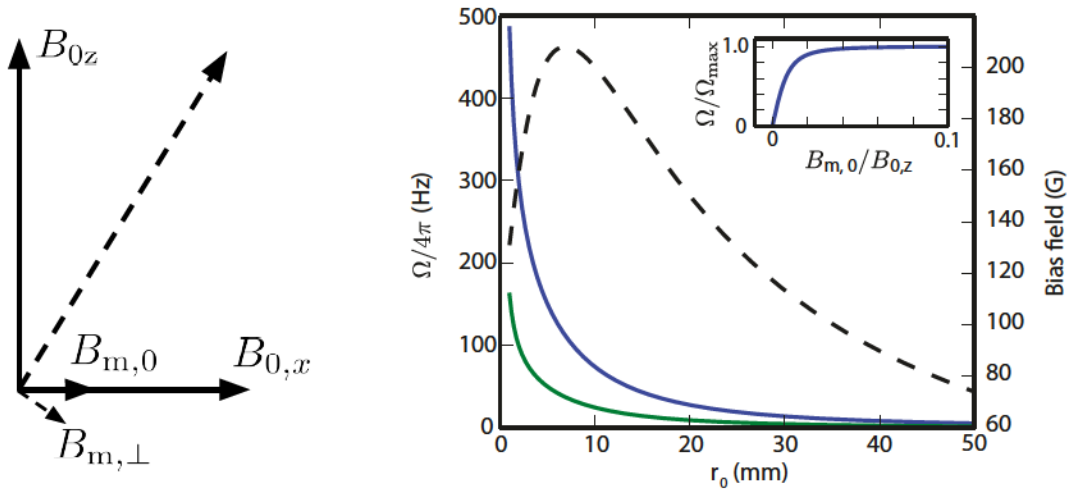

Figure 5.4: **Left**: Shift of the static field (long dashed arrow) due to addition of the static component of the field created by a magnetized nanostring $B_{0,x}$ to the background field B_{0z}. $B_{\mathrm{m},0}$ represents the oscillatory part and $B_{\mathrm{m},\perp}$ the effective oscillatory part with respect to the new quantization axis. **Right**: Dashed curve represents the bias magnetic field created by a pair of parallel on-chip wires separated by 10 μm with length of 10 mm, width of 10 μm, thickness of 4 μm with current of 1 A in the same direction. The field is shown (right axis) as a function of the distance from the nanostring r_0, where the nanostring is located 4 μm above the chip's surface. The coupling parameter in case when $B_{0,x}$ is cancelled by the bias field is shown (left axis) by the solid curves for magnetic-dipole (blue upper) and direct-current (lower green) cases. **Inset**: normalized coupling parameter as a function of oscillating-field-to-bias-field ratio $B_{\mathrm{m},0}/B_{0z}$. At a constant B_{0z} the coupling parameter is limited by $\Omega_{\max} = g_F \mu_B B_{\mathrm{m},0}\sqrt{F(F+1) - m_F(m_F \pm 1)}/2\hbar$.

magnets deposited on the chip [65] or by using a bias field created by pair of wires as is shown in Figure 5.2 (a). When B_{0z} is fully compensated, the coupling parameter can be improved, as seen in Figure 5.4 (right), where the coupling parameter is plotted for both kinds of devices in the presence of a compensating field.

5.3.4 Quantized coupling

Nanoresonators can be put in mechanical states with quantized motion by means of cryogenic and sideband cooling [15, 68–70]. In this case, the displacement of the nanostring from the equilibrium point should be described by operator $\hat{\alpha} = \alpha_0(\hat{a} + \hat{a}^\dagger)$, where $\alpha_0 = \sqrt{\hbar/2m_{\mathrm{eff}}\omega_{\mathrm{m}}}$ is the amplitude of zero-point motion and $\hat{a}$ is annihilation operator of the phonons in the mechanical mode. Considering an atom as a two-level system[1] with states $|\uparrow\rangle$ and $|\downarrow\rangle$, operator $\hat{F}_x$ in equation 5.6 can be written in terms of raising and lowering operators as $\hat{\sigma}_x = \hat{\sigma}^+ + \hat{\sigma}^-$. In this

[1]Two levels can be isolated in a strong magnetic field due to the quadratic Zeeman effect. Also, proposed schemes can be generalized for the case of multiple levels.

notation the interaction part of the Hamiltonian becomes $\frac{\hbar g_0}{2}\left(\sigma^+\hat{a}^\dagger + \sigma^+\hat{a} + \sigma^-\hat{a}^\dagger + \sigma^-\hat{a}\right)$, where $\hbar g_0 = g_F\mu_B b\alpha_0[F(F+1) - m_{F\uparrow}m_{F\downarrow}]^{1/2}/2$ is the single-atom-single-phonon coupling parameter. Neglecting the co-rotating terms $\sigma^+\hat{a}^\dagger$ and $\sigma^-\hat{a}$, in the rotating-wave approximation, the system of a magnetic mechanical resonator interacting with atomic spin is described by the Jaynes-Cummings Hamiltonian [71]

$$\hat{H}_{\rm at} = \hbar\omega_{\rm m}\hat{a}^\dagger\hat{a} + \frac{\hbar\omega_{\rm a}}{2}\hat{\sigma}_z + \frac{\hbar g_0}{2}(\hat{\sigma}^+\hat{a} + \hat{\sigma}^-\hat{a}^\dagger), \tag{5.12}$$

where $\hat{\sigma}_z = \hat{\sigma}^+\hat{\sigma}^- - \hat{\sigma}^-\hat{\sigma}^+$, and the first and second terms represent the energy of the mechanical mode and Zeeman energy of the atom, respectively.

Hamiltonian 5.12 can be generalized for a case of N atoms interacting with the resonator by introducing operators of the total atomic spin $\hat{\tilde{\sigma}}^+ = (1/\sqrt{N})\sum_{i=0}^{N}\hat{\sigma}_i^+$ and $\hat{\tilde{\sigma}}^- = (1/\sqrt{N})\sum_{i=0}^{N}\hat{\sigma}_i^-$, where $\hat{\sigma}_i^\pm$ corresponds to the spin of a single atom. This leads to the Tavis-Cummings Hamiltonian with an enhanced effective coupling $g_{eff} = \sqrt{N}g_0$ [71]. A similar enhancement occurs when there are n excitations in the mechanical mode [72], leading to the effective coupling of $g_{eff} = \sqrt{n}\sqrt{N}g_0$.

5.4 Magnetic coupling between atoms and a nanostring and its applications

To introduce the applications for quantum manipulation of the mechanical state of the oscillator, we consider a system of a single atom in a magnetic field B coupled to n phonons in the mechanical mode. The system is described by the wavefunction $|n, s\rangle$, where $s = (\uparrow, \downarrow)$. In the absence of the coupling, the energy levels of the system as a function of B form a ladder in the dressed state representation with levels $|n, \downarrow\rangle$ and $|n, \uparrow\rangle$ crossing at B_0 (see Figure 5.6(a)). Introducing the coupling leads to the avoided level crossing as was discussed in section 5.1. Sweeping the background field from $B_1 < B_0$ and $B_2 > 0$ will adiabatically flip the atomic spin with the Landau-Zener probability

$$p_{\rm LZ}(n) = 1 - \exp\left[-\frac{\pi\hbar n g_0^2}{2g_F\mu_B(\Delta B/\Delta t)}\right], \tag{5.13}$$

where the magnetic sweep is kept at a constant rate $\Delta B/\Delta t$ for a sufficiently long time Δt. The Landau-Zener probability can be controlled by adjusting the coupling strength and the field sweep duration (see Figure 5.5), and this control is robust provided that B_1 and B_2 are sufficiently far from B_0.

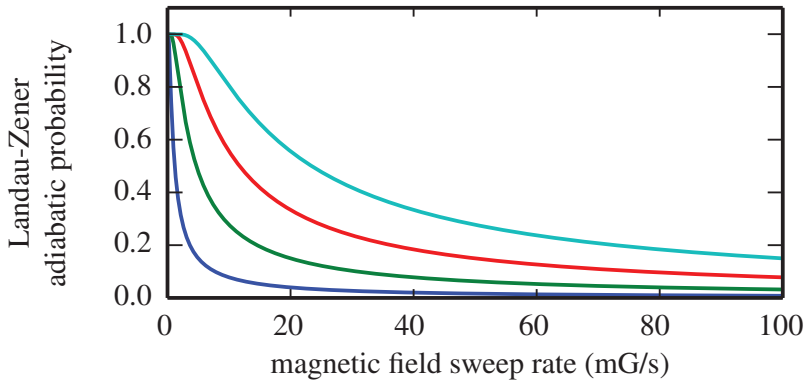

Figure 5.5: Landau-Zener probability as a function of the field sweep rate $\Delta B/\Delta t$ for a ^{87}Rb atom with $F = 1$ coupled to a nanostring with electric current of 1 A separated by 1 μm. Curves from bottom to top correspond to mean phonon number $\bar{n} = 5$, 20, 50, 100. Figure reprinted from [1].

5.4.1 Mechanical cooling

Cooling of the mechanical motion of a membrane in an atomic-nanomechanical hybrid system was already demonstrated by using optical coupling [17, 73]. Here we present a way to cool the mechanical motion of a nanoresonator by transferring the corresponding energy to Zeeman energy of atoms via a magnetic coupling, and then utilizing it by means of optical pumping (see section 4.2). During the first cooling step, for the atom starting in $|\downarrow\rangle$ state, after the field sweep $B_1 \to B_2$ (as is shown by black curve I in Figure 5.6(b)) the system makes a transition

$$|n,\downarrow\rangle \to \sqrt{p_{\mathrm{LZ}}(n)}\,|n-1,\uparrow\rangle + \sqrt{1-p_{\mathrm{LZ}}(n)}\,|n,\downarrow\rangle\,, \tag{5.14}$$

where we neglect the relative phase between the states and assume that $n > 0$. In the case of an adiabatic spin-flipping transition, the mechanical oscillator loses one phonon associated with its motion and the atom ends up in $|\uparrow\rangle$ state. After that, we optically pump the atom back to $|\downarrow\rangle$, dissipating the Zeeman energy of the atom through spontaneous emission (curve II in Figure 5.6(b)). During the second cooling step, we do the inverse field sweep $B_2 \to B_1$. If adiabaticity is achieved, the sweep will flip atomic spin and reduce the number of photons again (curve III in Figure 5.6(b)). The second optical pumping pulse then finishes the cooling cycle (curve IV in Figure 5.6(b)) putting the system into state $|n-2,\uparrow\rangle$, which has two photons less than the initial state.

Repetition of many such cycles leads to a substantial reduction in the mean phonon number as is shown in Figure 5.6(d)[1]. For the system including N atoms coupled to a resonator with

[1]This calculation was made by L.J. LeBlanc. See [1] for the details.

high phonon occupation $\bar{n} \geq N$, one cooling step reduces the mean phonon number proportionally to the number of spin-flip events: $\Delta\bar{n} = p_{LZ}(\overline{n})N$ which is equivalent to reducing the mechanical temperature by $\Delta T = \hbar\omega_{\rm m} N \Delta\bar{n}/k_{\rm B}$. For $\omega_{\rm m}/2\pi = 850$ kHz and $N = 10^5$ one cooling step decreases the temperature by $\Delta T = p_{\rm LZ}(\bar{n}) \times 4.1$ K.

For the cooling to be efficient, its rate should be higher the rate $\gamma_{\rm dec}$ at which thermal energy dissipates from the substrate to the mechanical motion [74]. The nanostring with parameters described in section 5.2 with current of 1 A couples to a ^{87}Rb atom in the $|F = 1\rangle$ state with a coupling strength of $g_0 = 21$ s^{-1}. The magnetic field sweep over 1 mG should be about 1 s in duration for the efficient cooling at low mechanical temperatures (see Figure 5.5). During this time atomic losses due to background or inelastic collisions can be neglected. Calculations of expected $\gamma_{\rm dec}$ are shown in section 5.2.

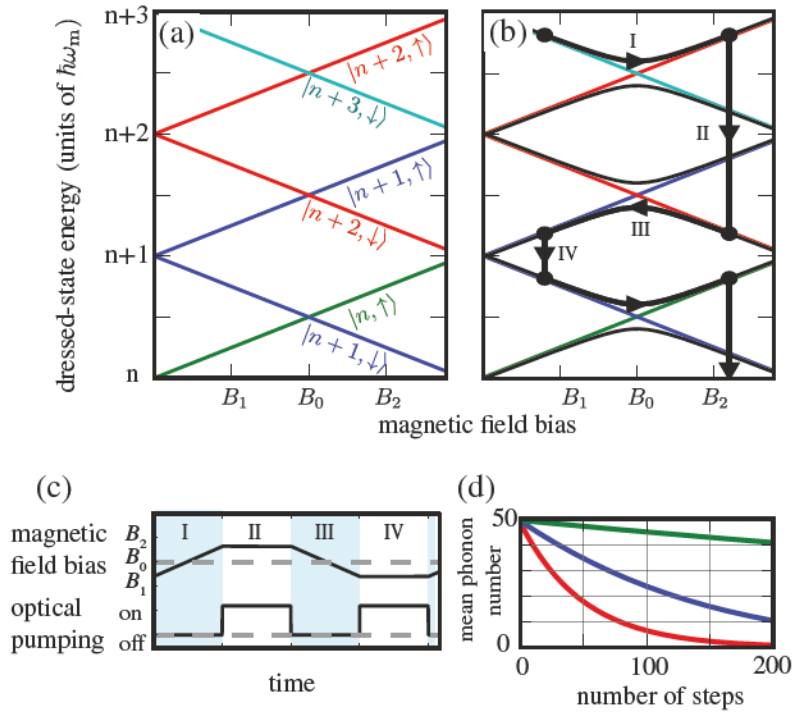

Figure 5.6: Mechanical cooling scheme. (a) Uncoupled Zeeman energy levels of a spin in a magnetic field "dressed" with phonons. (b) Zeeman energy levels of a spin coupled to phonons, with black curves representing a single cooling cycle. (c) Schematics of a single cooling cycle. (d) Mean phonon number $\bar{n}$ during the mechanical cooling starting with $\bar{n} = 50$ for (from bottom to top) $p_{LZ}(1) = 1$ (red curve), $p_{LZ}(1) = 0.5$ (blue curve), and $p_{LZ}(1) = 0.1$ (green curve). One step includes one magnetic field sweep and one optical pumping pulse for a single spin. Figure reprinted from [1] (Credit: L.J. LeBlanc).

5.4.2 Mechanical thermometry

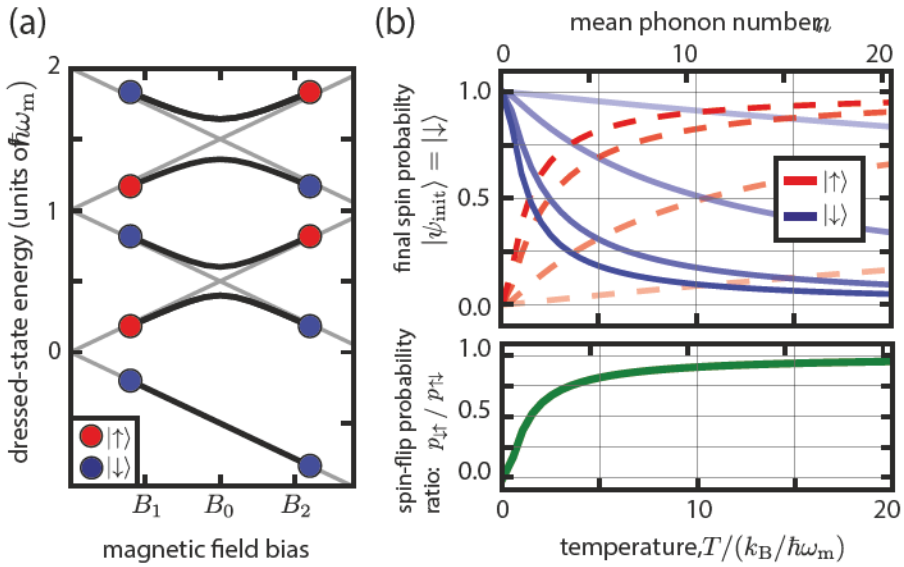

Figure 5.7: Schematics of mechanical thermometry. (a) Zeeman energy levels of a spin coupled to phonons near the mechanical ground state in the dressed-state picture. (b, upper) Probability to find the spin in $|\uparrow\rangle$ (red dashed) and $|\downarrow\rangle$ (blue solid) after one field sweep as a function of the mean phonon number, if is the original state is $|\downarrow\rangle$. Darkest curves correspond to $p_{LZ}(1) = 1.0$ and the respectevly fainter curves represent $p_{LZ}(1) = 0.75$, 0.5 and 0.25. (b,lower) Ratio of spin-flip probability $p_{\downarrow\uparrow}$ to $p_{\uparrow\downarrow}$ as a function of mechanical temperature. Figure reprinted from [1] (Credit: L.J. LeBlanc).

Landau-Zener sweeps at low phonon number $\bar{n}$ can also be used for mechanical thermometry. The energy conservation law forbids the adiabatic spin-flipping transition for the system starting at $|0,\downarrow\rangle$ (see Figure 5.7(a)). As a result, the spin-flip probability for state $|\downarrow\rangle$ is given by

$$p_{\downarrow\uparrow} = p_{LZ}(\bar{n}) \times (1 - p_{\omega_m}(0)) = p_{LZ}(\bar{n}) \times \exp(-\hbar\omega_m/k_B T), \tag{5.15}$$

where $p_{\omega_m}(0) = 1 - \exp(-\hbar\omega_m/k_B T)$ is the probability of having zero phonons in the oscillator's mode ω_m in the Bose-Einstein statistics. Since the spin-flip probability for state $|\uparrow\rangle$ is $p_{\uparrow,\downarrow} = p_{LZ}(\bar{n})$, the ratio of spin-flip probabilities corresponding to different spin states at the same field sweep parameters is determined only by the mechanical temperature:

$$\frac{p_{\downarrow\uparrow}}{p_{\uparrow\downarrow}} = \exp\left(-\frac{\hbar\omega_m}{k_B T}\right). \tag{5.16}$$

The same result can also be obtained by a more rigorous numerical simulation[1] as is shown in Figure 5.7(b).

In the experiment, the spin-flip probability ratio can be determined by repeating measurements for a single atom or by measuring an ensemble of many atoms. Figure 5.7(b) shows that the proposed Landau-Zener thermometry is especially efficient at mean phonon numbers below 10, which makes this technique attractive in a difficult-to-access regime [15, 68–70, 75–77].

At high mechanical temperatures, thermometry can be carried out by using the dependence of the coupling strength on the mean number of phonon excitations. In this case, measuring the spin-flip probability for $|\uparrow\rangle$ gives the Landau-Zener probability, from which the number of phonons can be extracted from expression 5.13.

5.4.3 Quantum entanglement between nanostrings

Here we consider a way to create quantum entanglement between two unconnected oscillators by coupling them to the same spin, which can be transported between the locations of these oscillators. After a Landau-Zener sweep, the system of a spin coupled to the nanomechanical oscillator phonon modes ends up in an entangled state. By moving this spin to a different mechanical oscillator and performing a second Landau-Zener sweep, quantum entanglement between these two oscillators can be created. For example, consider the system of two unconnected oscillators in the phononic Fock states n_1 and n_2 and atomic spin $|\uparrow\rangle$ described by the wavefunction $|\psi_i\rangle = |n_1, n_2, \uparrow\rangle$. After Landau-Zener sweep with probability p_1 for the spin coupled to the first oscillator only, the system goes to state $|\psi_i\rangle \to \sqrt{p_1}\,|n_1+1, n_2, \downarrow\rangle + \sqrt{\bar{p_1}}\,|n_1, n_2, \uparrow\rangle$, where $\bar{p_1} = 1 - p_1$ and the phase difference is neglected. After moving the spin from the first to the second oscillator, the second sweep with probability p_2 results in

$$\begin{aligned} |\psi_f\rangle = &\left[\sqrt{p_1 p_2}\,|n_1+1, n_2-1, \uparrow\rangle + \sqrt{\bar{p}_1\bar{p}_2}\,|n_1, n_2, \uparrow\rangle\right] \\ &+ \left[\sqrt{p_1\bar{p}_2}\,|n_1+1, n_2, \downarrow\rangle + \sqrt{\bar{p}_1 p_2}\,|n_1, n_2+1, \downarrow\rangle\right]. \end{aligned} \tag{5.17}$$

In the simple case where $p_1 = p_2 = 1/2$, a spin measurement will leave the two resonators in an entangled state: either $|\psi_f\rangle = (|n_1+1, n_2\rangle + |n_1, n_2+1\rangle)/\sqrt{2}$ if the measured spin is $|\downarrow\rangle$ or $|\psi_f\rangle = (|n_1, n_2\rangle + |n_1+1, n_2-1\rangle)/\sqrt{2}$ if $|\uparrow\rangle$-state is measured.

The situation is slightly different when both oscillators are in the ground state with $n_1 = n_2 = 0$.

[1] This calculation was made by L.J. LeBlanc. See [1] for the details.

In this case the adiabatic transition $|\downarrow\rangle \rightarrow |\uparrow\rangle$ is forbidden, and the system starting in $|\psi_i\rangle = |0,0,\uparrow\rangle$ after the two sweeps will be found in the state $|\psi_f\rangle = \sqrt{p_1}\,|1,0,\downarrow\rangle + \sqrt{\bar{p}_1 p_2}\,|0,1,\downarrow\rangle + \sqrt{\bar{p}_1\bar{p}_2}\,|0,0,\uparrow\rangle$. If the Landau-Zener probabilities are $p_1 = 1/2$ and $p_2 = 1$ the mechanical resonators will end up in the entangled state $|\psi_{f,m}\rangle = (|1,0\rangle + |0,1\rangle)/\sqrt{2}$ independently of the spin-measurement outcome.

For the successful generation of entanglement, the whole system should maintain coherence during the protocol described above. The decoherence rate for a Fock state $|n\rangle$ is given by [74]

$$\Gamma_{m,\mathrm{Fock}} = (n+1)\bar{n}_s\Gamma_m + n(\bar{n}_s+1)\Gamma_m, \tag{5.18}$$

where $\bar{n}_s$ is the mean phonon number of the substrate and $\Gamma_m = \omega_m/Q$ is the damping rate of the mechanical oscillator. Near the ground state, the Fock state decoherence rate is mainly determined by $\bar{n}_s$ and can be significantly decreased by cooling the substrate to cryogenic temperatures.

Chapter 6

Summary and future directions

In summary, we have built an apparatus for experiments on the hybridization of ultracold gases with other quantum systems, whose design should allow us to rapidly switch different chips while maintaining the complex setup for atomic cooling unchanged. By baking the vacuum system, we have successfully achieved the ultrahigh vacuum conditions with pressure of the order of 10^{-10} Torr.

For cooling atoms to ultralow temperatures, we have set up an optical system to arrange three pairs of circularly polarized counter-propagating beams intersecting at one point, as well as an electronic system to create a quadrupole magnetic field with adjustable position of its zero. We have demonstrated successful magneto-optical trapping of ^{87}Rb atomic clouds with up to 10^8 atoms and cooling below the Doppler cooling limit by means polarization gradient cooling in optical molasses to temperatures near 80 μK. For further reduction in temperature, we implemented RF-induced evaporative cooling in a compressed quadrupole magnetic trap. Even though during the trapping the temperature increases to $200 - 300$ μK, after several steps of the evaporation it should go down to $1 - 10$ μK. So far, the first successful step has shown the temperature decrease from 280 μK to 140 μK with total number of 1.7×10^7 atoms left in the magnetic trap.

In the near future, we expect to cool atoms to the temperatures where they can be captured by an optical dipole trap, whose optics are already assembled. After that, the transport of atoms from the preparation region to the science cell by moving the focus of the trapping laser beam should be tested and optimized. Finally, we want to observe the magnetic coupling between the ultracold gas and an on-chip nanomechanics starting with simpler experiments analogous to the one described in [20] and then moving to the experiments proposed in Chapter 5 as well as possible experiments with optical cavities proposed in [78]. For these experiments with the chips we will

need to design, manufacture and install a chip holder to the science chamber. Meanwhile we are planning to update the current apparatus with an additional load-lock chamber and a magnetic transfer arm to simplify and accelerate the chips loading.

When finished, our apparatus will allow us to integrate ultracold atomic ensembles with various quantum systems using atom-chip technology. This has a potential for advancing current application of quantum physics, including processing and storage of quantum information, quantum communication and cryptography, and high-precision measurements. Besides, it will provide opportunities to study fundamental questions of classical-to-quantum crossover and quantum decoherence.

Bibliography

[1] A. Tretiakov and L. J. LeBlanc, "Magnetic-field-mediated coupling and control in hybrid atomic-nanomechanical systems," *Phys. Rev. A*, vol. 94, p. 043802, Oct 2016.

[2] G. Kurizki, P. Bertet, Y. Kubo, K. Mølmer, D. Petrosyan, P. Rabl, and J. Schmiedmayer, "Quantum technologies with hybrid systems," *Proceedings of the National Academy of Sciences*, vol. 112, no. 13, pp. 3866–3873, 2015.

[3] P. Treutlein, C. Genes, K. Hammerer, M. Poggio, and P. Rabl, "Hybrid Mechanical Systems," in *Cavity Optomechanics* (M. Aspelmeyer, T. J. Kippenberg, and F. Marquardt, eds.), pp. 327–351, Berlin: Springer, July 2014.

[4] M. Wallquist, K. Hammerer, P. Rabl, M. Lukin, and P. Zoller, "Hybrid quantum devices and quantum engineering," *Physica Scripta*, vol. 2009, no. T137, p. 014001, 2009.

[5] J. Raftery, D. Sadri, S. Schmidt, H. E. Türeci, and A. A. Houck, "Observation of a dissipation-induced classical to quantum transition," *Physical Review X*, vol. 4, no. 3, p. 031043, 2014.

[6] I. Katz, A. Retzker, R. Straub, and R. Lifshitz, "Signatures for a classical to quantum transition of a driven nonlinear nanomechanical resonator," *Physical Review Letters*, vol. 99, no. 4, p. 040404, 2007.

[7] R. Z. Vered, Y. Shaked, Y. Ben-Or, M. Rosenbluh, and A. Peer, "Classical-to-quantum transition with broadband four-wave mixing," *Physical Review Letters*, vol. 114, no. 6, p. 063902, 2015.

[8] W. H. Zurek, "Decoherence, einselection, and the quantum origins of the classical," *Reviews of Modern Physics*, vol. 75, no. 3, p. 715, 2003.

[9] Z.-L. Xiang, S. Ashhab, J. You, and F. Nori, "Hybrid quantum circuits: Superconducting circuits interacting with other quantum systems," *Reviews of Modern Physics*, vol. 85, no. 2, p. 623, 2013.

[10] M. H. Devoret and R. J. Schoelkopf, "Superconducting circuits for quantum information: an outlook," *Science*, vol. 339, no. 6124, pp. 1169–1174, 2013.

[11] O. Arcizet, V. Jacques, A. Siria, P. Poncharal, P. Vincent, and S. Seidelin, "A single nitrogen-vacancy defect coupled to a nanomechanical oscillator," *Nature Physics*, vol. 7, no. 11, pp. 879–883, 2011.

[12] H.-R. Wei and G. L. Long, "Hybrid quantum gates between flying photon and diamond nitrogen-vacancy centers assisted by optical microcavities," *Scientific reports*, vol. 5, 2015.

[13] E. Verhagen, S. Deléglise, S. Weis, A. Schliesser, and T. J. Kippenberg, "Quantum-coherent coupling of a mechanical oscillator to an optical cavity mode," *Nature*, vol. 482, no. 7383, pp. 63–67, 2012.

[14] A. D. OConnell, M. Hofheinz, M. Ansmann, R. C. Bialczak, M. Lenander, E. Lucero, M. Neeley, D. Sank, H. Wang, M. Weides, *et al.*, "Quantum ground state and single-phonon control of a mechanical resonator," *Nature*, vol. 464, no. 7289, pp. 697–703, 2010.

[15] J. Teufel, T. Donner, D. Li, J. Harlow, M. Allman, K. Cicak, A. Sirois, J. D. Whittaker, K. Lehnert, and R. W. Simmonds, "Sideband cooling of micromechanical motion to the quantum ground state," *Nature*, vol. 475, no. 7356, pp. 359–363, 2011.

[16] S. Camerer, M. Korppi, A. Jöckel, D. Hunger, T. W. Hänsch, and P. Treutlein, "Realization of an optomechanical interface between ultracold atoms and a membrane," *Physical Review Letters*, vol. 107, no. 22, p. 223001, 2011.

[17] A. Jöckel, A. Faber, T. Kampschulte, M. Korppi, M. T. Rakher, and P. Treutlein, "Sympathetic cooling of a membrane oscillator in a hybrid mechanical–atomic system," *Nature nanotechnology*, vol. 10, no. 1, pp. 55–59, 2015.

[18] B. Vogell, K. Stannigel, P. Zoller, K. Hammerer, M. Rakher, M. Korppi, A. Jöckel, and P. Treutlein, "Cavity-enhanced long-distance coupling of an atomic ensemble to a micromechanical membrane," *Physical Review A*, vol. 87, no. 2, p. 023816, 2013.

[19] Y.-J. Wang, M. Eardley, S. Knappe, J. Moreland, L. Hollberg, and J. Kitching, "Magnetic resonance in an atomic vapor excited by a mechanical resonator," *Physical Review Letters*, vol. 97, no. 22, p. 227602, 2006.

[20] C. Montoya, J. Valencia, A. A. Geraci, M. Eardley, J. Moreland, L. Hollberg, and J. Kitching, "Resonant interaction of trapped cold atoms with a magnetic cantilever tip," *Physical Review A*, vol. 91, no. 6, p. 063835, 2015.

[21] D. Hunger, S. Camerer, T. W. Hänsch, D. König, J. P. Kotthaus, J. Reichel, and P. Treutlein, "Resonant coupling of a bose-einstein condensate to a micromechanical oscillator," *Physical Review Letters*, vol. 104, no. 14, p. 143002, 2010.

[22] S. S. Verbridge, J. M. Parpia, R. B. Reichenbach, L. M. Bellan, and H. Craighead, "High quality factor resonance at room temperature with nanostrings under high tensile stress," *Journal of Applied Physics*, vol. 99, no. 12, p. 124304, 2006.

[23] S. S. Verbridge, H. G. Craighead, and J. M. Parpia, "A megahertz nanomechanical resonator with room temperature quality factor over a million," *Applied Physics Letters*, vol. 92, no. 1, pp. 13112–13112, 2008.

[24] T. S. Biswas, A. Suhel, B. D. Hauer, A. Palomino, K. S. Beach, and J. P. Davis, "High-q gold and silicon nitride bilayer nanostrings," *Applied Physics Letters*, vol. 101, no. 9, p. 093105, 2012.

[25] S. Schmid, K. Jensen, K. Nielsen, and A. Boisen, "Damping mechanisms in high-q micro and nanomechanical string resonators," *Physical Review B*, vol. 84, no. 16, p. 165307, 2011.

[26] R. Folman, P. Krüger, D. Cassettari, B. Hessmo, T. Maier, and J. Schmiedmayer, "Controlling cold atoms using nanofabricated surfaces: atom chips," *Physical Review Letters*, vol. 84, no. 20, p. 4749, 2000.

[27] R. Folman, P. Kruger, J. Schmiedmayer, J. Denschlag, and C. Henkel, "Microscopic atom optics: from wires to an atom chip," *arXiv preprint arXiv:0805.2613*, 2008.

[28] S. Bernon, H. Hattermann, D. Bothner, M. Knufinke, P. Weiss, F. Jessen, D. Cano, M. Kemmler, R. Kleiner, D. Koelle, *et al.*, "Manipulation and coherence of ultra-cold atoms on a superconducting atom chip," *Nature communications*, vol. 4, 2013.

[29] Y. Colombe, T. Steinmetz, G. Dubois, F. Linke, D. Hunger, and J. Reichel, "Strong atom–field coupling for bose–einstein condensates in an optical cavity on a chip," *Nature*, vol. 450, no. 7167, pp. 272–276, 2007.

[30] M. A. Naides, R. W. Turner, R. A. Lai, J. M. DiSciacca, and B. L. Lev, "Trapping ultracold gases near cryogenic materials with rapid reconfigurability," *Applied Physics Letters*, vol. 103, no. 25, p. 251112, 2013.

[31] J. Léonard, M. Lee, A. Morales, T. M. Karg, T. Esslinger, and T. Donner, "Optical transport and manipulation of an ultracold atomic cloud using focus-tunable lenses," *New Journal of Physics*, vol. 16, no. 9, p. 093028, 2014.

[32] J. R. Rubbmark, M. M. Kash, M. G. Littman, and D. Kleppner, "Dynamical effects at avoided level crossings: A study of the landau-zener effect using rydberg atoms," *Physical Review A*, vol. 23, no. 6, p. 3107, 1981.

[33] C. J. Foot, *Atomic physics*, ch. 7. Oxford: Oxford University Press, 2005.

[34] H. J. Metcalf and P. Straten, *Laser cooling and trapping of neutral atoms*, ch. 1. Berlin: Springer, 1999.

[35] D. A. Steck, *Quantum and atom optics*, ch. 11. Oregon: University of Oregon, 2007.

[36] C. J. Foot, *Atomic physics*, ch. 4. Oxford: Oxford University Press, 2005.

[37] C. Cohen-Tannoudji, B. Diu, and F. Laloë, *Quantum Mechanics.*, ch. XII. New York: Wiley-Interscience, 2006.

[38] B. G. Sidharth, "Revisiting zitterbewegung," *International Journal of Theoretical Physics*, vol. 48, no. 2, pp. 497–506, 2009.

[39] C. J. Foot, *Atomic physics*, ch. 6. Oxford: Oxford University Press, 2005.

[40] D. A. Steck, "Rubidium 87 d line data." `http://steck.us/alkalidata/rubidium87numbers.pdf`, 2001.

[41] D. A. Steck, *Quantum and atom optics*, ch. 7. Oregon: University of Oregon, 2007.

[42] C. J. Foot, *Atomic physics*, ch. 5. Oxford: Oxford University Press, 2005.

[43] W. H. Wing, "On neutral particle trapping in quasistatic electromagnetic fields," *Progress in Quantum Electronics*, vol. 8, no. 3-4, pp. 181–199, 1984.

[44] H. J. Metcalf and P. Straten, *Laser cooling and trapping of neutral atoms*, ch. 10. Berlin: Springer, 1999.

[45] C. Klempt, T. Van Zoest, T. Henninger, E. Rasel, W. Ertmer, J. Arlt, *et al.*, "Ultraviolet light-induced atom desorption for large rubidium and potassium magneto-optical traps," *Physical Review A*, vol. 73, no. 1, p. 013410, 2006.

[46] C. J. Foot, *Atomic physics*, ch. 8. Oxford: Oxford University Press, 2005.

[47] D. A. Steck, "Rubidium 85 d line data." `http://steck.us/alkalidata/rubidium85numbers.pdf`, 2008.

[48] L. D. Landau and E. Lifshitz, *Statistical physics, part I*, ch. 38. Oxford: pergamon, Oxford, 1980.

[49] T. M. Brzozowski, M. Maczynska, M. Zawada, J. Zachorowski, and W. Gawlik, "Time-of-flight measurement of the temperature of cold atoms for short trap-probe beam distances," *Journal of Optics B: Quantum and Semiclassical Optics*, vol. 4, no. 1, p. 62, 2002.

[50] H. J. Metcalf and P. Straten, *Laser cooling and trapping of neutral atoms*, ch. 7. Berlin: Springer, 1999.

[51] C. J. Foot, *Atomic physics*, ch. 9. Oxford: Oxford University Press, 2005.

[52] H. J. Metcalf and P. Straten, *Laser cooling and trapping of neutral atoms*, ch. 11. Berlin: Springer, 1999.

[53] J. Dalibard and C. Cohen-Tannoudji, "Laser cooling below the doppler limit by polarization gradients: simple theoretical models," *JOSA B*, vol. 6, no. 11, pp. 2023–2045, 1989.

[54] W. Ketterle and N. Van Druten, "Evaporative cooling of trapped atoms," *Advances in atomic, molecular, and optical physics*, vol. 37, pp. 181–236, 1996.

[55] R. Grimm, M. Weidemüller, and Y. B. Ovchinnikov, "Optical dipole traps for neutral atoms," *Advances in atomic, molecular, and optical physics*, vol. 42, pp. 95–170, 2000.

[56] L. D. Landau and E. Lifshitz, *Statistical physics, part I*, ch. 3. Oxford: pergamon, Oxford, 1980.

[57] M.-X. K. Na, "Optical transport of cold atoms." `https://sites.ualberta.ca/~ljleblan/naphys499_2015.pdf`.

[58] A. Couvert, T. Kawalec, G. Reinaudi, and D. Guéry-Odelin, "Optimal transport of ultracold atoms in the non-adiabatic regime," *EPL (Europhysics Letters)*, vol. 83, no. 1, p. 13001, 2008.

[59] L. D. Landau and E. Lifshitz, *Course of theoretical physics, quantum mechanics non-relativistic theory*. Oxford: Pergamon, 1991.

[60] L. LeBlanc, A. Bardon, J. McKeever, M. Extavour, D. Jervis, J. Thywissen, F. Piazza, and A. Smerzi, "Dynamics of a tunable superfluid junction," *Physical Review Letters*, vol. 106, no. 2, p. 025302, 2011.

[61] C. J. Straatsma, M. K. Ivory, J. Duggan, J. Ramirez-Serrano, D. Z. Anderson, and E. A. Salim, "On-chip optical lattice for cold atom experiments," *Optics letters*, vol. 40, no. 14, pp. 3368–3371, 2015.

[62] J. P. Burke Jr, S.-T. Chu, G. W. Bryant, C. Williams, and P. Julienne, "Designing neutral-atom nanotraps with integrated optical waveguides," *Physical Review A*, vol. 65, no. 4, p. 043411, 2002.

[63] D. Hunger, S. Camerer, M. Korppi, A. Jöckel, T. W. Hänsch, and P. Treutlein, "Coupling ultracold atoms to mechanical oscillators," *Comptes Rendus Physique*, vol. 12, no. 9, pp. 871–887, 2011.

[64] Z. Darázs, Z. Kurucz, O. Kálmán, T. Kiss, J. Fortágh, and P. Domokos, "Parametric amplification of the mechanical vibrations of a suspended nanowire by magnetic coupling to a bose-einstein condensate," *Phys. Rev. Lett.*, vol. 112, p. 133603, Apr 2014.

[65] P. Treutlein, D. Hunger, S. Camerer, T. W. Hänsch, and J. Reichel, "Bose-einstein condensate coupled to a nanomechanical resonator on an atom chip," *Physical Review Letters*, vol. 99, no. 14, p. 140403, 2007.

[66] S. Steinke, S. Singh, M. Tasgin, P. Meystre, K. Schwab, and M. Vengalattore, "Quantum-measurement backaction from a bose-einstein condensate coupled to a mechanical oscillator," *Physical Review A*, vol. 84, no. 2, p. 023841, 2011.

[67] Z. Diao, J. E. Losby, J. A. Burgess, V. T. Sauer, W. K. Hiebert, and M. R. Freeman, "Stiction-free fabrication of lithographic nanostructures on resist-supported nanomechanical resonators," *Journal of Vacuum Science & Technology B*, vol. 31, no. 5, p. 051805, 2013.

[68] S. M. Meenehan, J. D. Cohen, G. S. MacCabe, F. Marsili, M. D. Shaw, and O. Painter, "Pulsed excitation dynamics of an optomechanical crystal resonator near its quantum ground state of motion," *Physical Review X*, vol. 5, no. 4, p. 041002, 2015.

[69] R. Riedinger, S. Hong, R. A. Norte, J. A. Slater, J. Shang, A. G. Krause, V. Anant, M. Aspelmeyer, and S. Gröblacher, "Non-classical correlations between single photons and phonons from a mechanical oscillator," *Nature*, vol. 530, no. 7590, pp. 313–316, 2016.

[70] E. E. Wollman, C. Lei, A. Weinstein, J. Suh, A. Kronwald, F. Marquardt, A. Clerk, and K. Schwab, "Quantum squeezing of motion in a mechanical resonator," *Science*, vol. 349, no. 6251, pp. 952–955, 2015.

[71] B. W. Shore and P. L. Knight, "The jaynes-cummings model," *Journal of Modern Optics*, vol. 40, no. 7, pp. 1195–1238, 1993.

[72] J. Fink, M. Göppl, M. Baur, R. Bianchetti, P. Leek, A. Blais, and A. Wallraff, "Climbing the jaynes–cummings ladder and observing its nonlinearity in a cavity qed system," *Nature*, vol. 454, no. 7202, pp. 315–318, 2008.

[73] K. Hammerer, K. Stannigel, C. Genes, P. Zoller, P. Treutlein, S. Camerer, D. Hunger, and T. Hänsch, "Optical lattices with micromechanical mirrors," *Physical Review A*, vol. 82, no. 2, p. 021803, 2010.

[74] M. Aspelmeyer, T. J. Kippenberg, and F. Marquardt, "Cavity optomechanics," *Reviews of Modern Physics*, vol. 86, no. 4, p. 1391, 2014.

[75] G. Harris, D. McAuslan, E. Sheridan, Y. Sachkou, C. Baker, and W. Bowen, "Laser cooling and control of excitations in superfluid helium," *Nature Physics*, 2016.

[76] E. Gavartin, R. Braive, I. Sagnes, O. Arcizet, A. Beveratos, T. J. Kippenberg, and I. Robert-Philip, "Optomechanical coupling in a two-dimensional photonic crystal defect cavity," *Physical Review Letters*, vol. 106, no. 20, p. 203902, 2011.

[77] A. MacDonald, B. Hauer, X. Rojas, P. Kim, G. Popowich, and J. Davis, "Optomechanics and thermometry of cryogenic silica microresonators," *Physical Review A*, vol. 93, no. 1, p. 013836, 2016.

[78] C. A. Potts, A. Melnyk, H. Ramp, M. H. Bitarafan, D. Vick, L. J. LeBlanc, J. P. Davis, and R. G. DeCorby, "Tunable open-access microcavities for on-chip cavity quantum electrodynamics," *Applied Physics Letters*, vol. 108, no. 4, 2016.

Appendix A

Here we present absorption images after different stages of the experiment. We also give the stages' time t, measured number of atoms N and temperature T. In all figures colorbar represent optical density $n\sigma_s l$ and the pixel size is 3.2 μm.

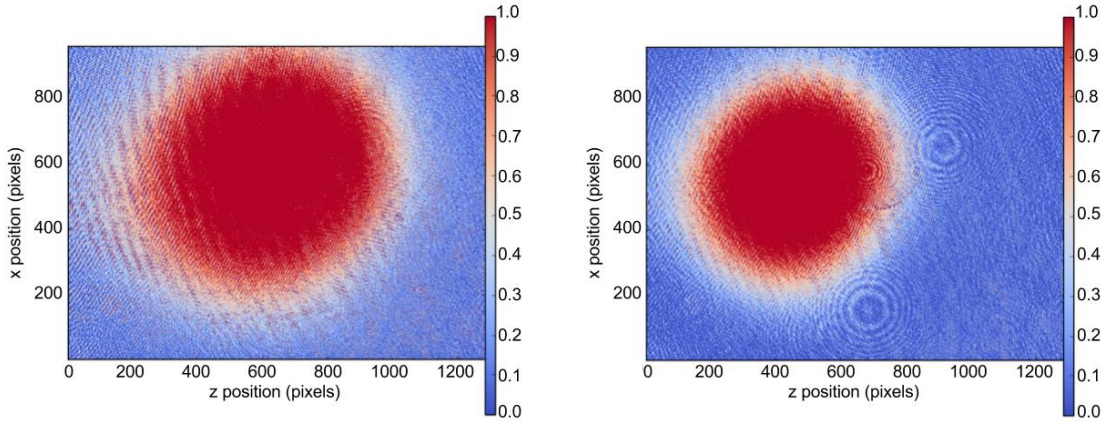

Figure A.1: **Left**: Magneto-optical trap: $t = 15$ s, $N = 3.2 \times 10^7$, $T = 250$ μK. **Right**:Optical molasses: $t = 5$ ms, $N = 3.0 \times 10^7$, $T = 80$ μK.

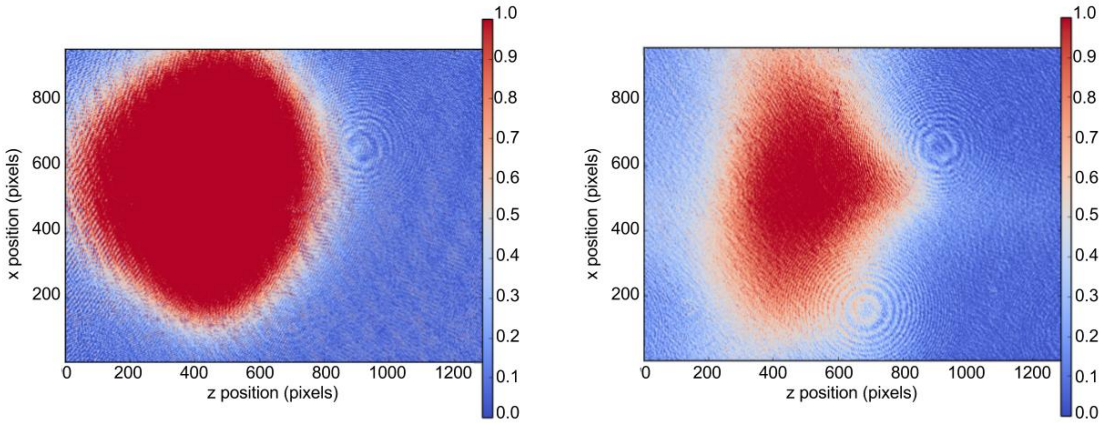

Figure A.2: **Left**: Optical pumping: $t = 3.5$ ms, $N = 3.5 \times 10^7$, $T = 80$ μK. **Right**: Magnetic trap at 65 A: $t = 74$ ms, $N = 3.0 \times 10^7$, $T = 140$ μK.

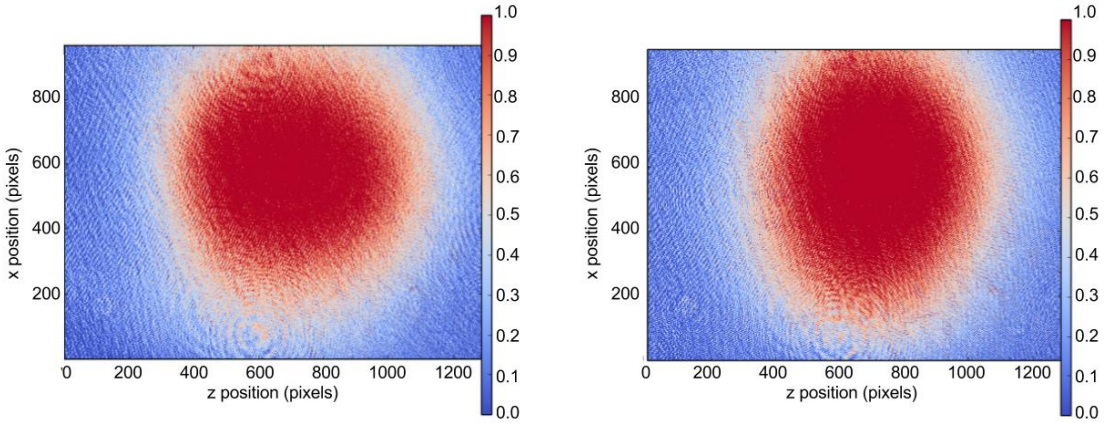

Figure A.3: **Left**: Magnetic trap at 420 A: $t = 0.5$ s, $N = 2.4 \times 10^7$, $T = 300$ μK. **Right**: Magnetic trap at 420 A: $t = 4$ s, $N = 3.7 \times 10^7$, $T = 280$ μK.